



## Boundary dynamics in 3D printed samples

Zhang, Chunlei

*Publication date:*  
2022

*Document Version*  
Publisher's PDF, also known as Version of record

[Link back to DTU Orbit](#)

*Citation (APA):*  
Zhang, C. (2022). *Boundary dynamics in 3D printed samples*. Technical University of Denmark.

---

### General rights

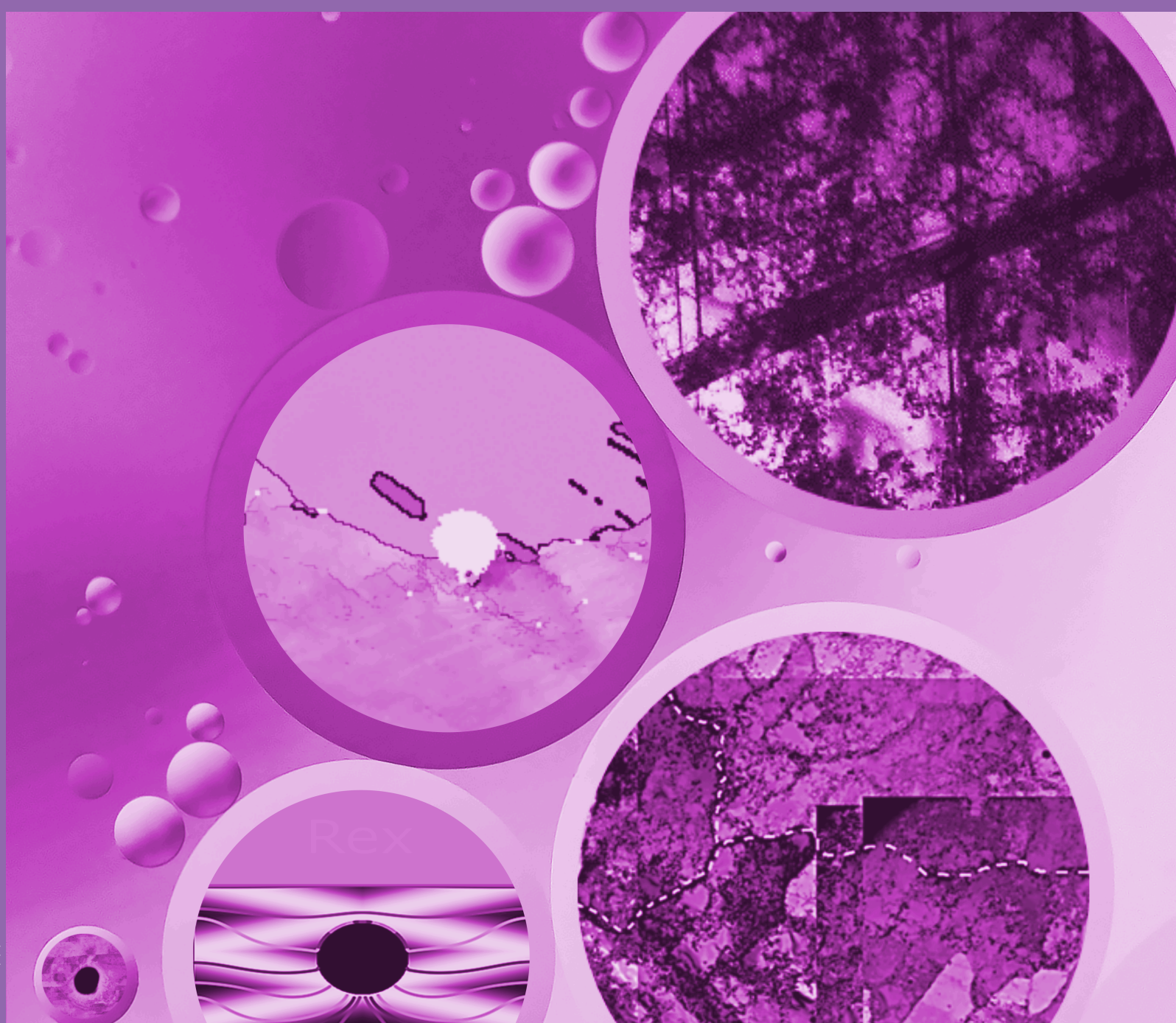
Copyright and moral rights for the publications made accessible in the public portal are retained by the authors and/or other copyright owners and it is a condition of accessing publications that users recognise and abide by the legal requirements associated with these rights.

- Users may download and print one copy of any publication from the public portal for the purpose of private study or research.
- You may not further distribute the material or use it for any profit-making activity or commercial gain
- You may freely distribute the URL identifying the publication in the public portal

If you believe that this document breaches copyright please contact us providing details, and we will remove access to the work immediately and investigate your claim.

# Boundary dynamics in 3D printed samples

Chunlei Zhang



# **Boundary dynamics in 3D printed samples**

By

**Chunlei Zhang**

February 2022



Section of Manufacturing Engineering  
Department of Mechanical Engineering  
Technical University of Denmark



## **Boundary dynamics in 3D printed samples**

### **A doctoral thesis by**

Chunlei Zhang

E-mail: [chzhang@mek.dtu.dk](mailto:chzhang@mek.dtu.dk)

Technical University of Denmark

Section of Manufacturing Engineering

Department of Mechanical Engineering

Building 425, Room 209, DK-2800 Kgs. Lyngby

### **Principal Supervisor:**

Senior scientist Tianbo Yu

E-mail: [tjyu@mek.dtu.dk](mailto:tjyu@mek.dtu.dk)

Technical University of Denmark

Section of Manufacturing Engineering

Department of Mechanical Engineering

Building 425, Room 214, DK-2800 Kgs. Lyngby

### **Co-Supervisor:**

Professor Dorte Juul Jensen

E-mail: [doje@mek.dtu.dk](mailto:doje@mek.dtu.dk)

Technical University of Denmark

Section of Manufacturing Engineering

Department of Mechanical Engineering

Building 425, Room 206, DK-2800 Kgs. Lyngby



# Preface

This thesis is submitted in partial fulfilment of the requirements for the Ph.D. degree at the Technical University of Denmark (DTU). The PhD project is funded by European Research Council (ERC) under the European Union's Horizon 2020 research and innovation programme (ERC Advanced grant M4D led by Professor Dorte Juul Jensen; grant agreement No. 788567) and China Scholarship Council (CSC) (No. 201706120026). The PhD work was carried out at the Section of Manufacturing Engineering, Department of Mechanical Engineering between February 15<sup>th</sup> 2019 and February 14<sup>th</sup> 2022. The project was supervised by Senior Scientist Tianbo Yu and Professor Dorte Juul Jensen from Section of Manufacturing Engineering, Department of Mechanical Engineering.

Chunlei Zhang

Risø, Roskilde, Feb. 10<sup>th</sup> 2022



# Abstract

Additive manufacturing (or 3D printing) of metallic components has recently become very popular as it enables net-shape manufacturing as well as complex designs that are not easily achievable by conventional processing. 3D printed metallic components are likely to be deformed and/or exposed to high temperatures during application and therefore it is necessary to investigate the deformation and annealing behaviours of 3D printed components—the two objectives of this thesis. Stainless steel 316L is chosen as the example in this work because this material is relatively easy to print without introducing too many voids. Laser powder bed fusion (L-PBF) is used to print 316L samples according to industrial standards. Various characterization techniques are used, including electron microscopy: scanning electron microscopy/electron backscatter diffraction (SEM/EBSD) and transmission electron microscopy (TEM), X-ray diffraction (XRD) and X-ray absorption contrast tomography, Vickers hardness measurement and tensile test.

Before analysis of the deformation behaviour of 3D printed 316L samples, conventionally manufactured 316L is deformed by cold rolling and the microstructure and the texture evolution are followed as a function of deformation strain—to serve as a solid basis for the subsequent analysis of the printed samples. It is found that a Taylor lattice structure forms at low strain; deformation twinning and shear banding gradually develop with increasing deformation; martensite transformation occurs mainly in the shear bands at rolling reductions larger than 30%. Deformation twinning transforms the Copper orientation to twin Copper orientation, and texture transition from the Copper to the Brass type occurs at the onset of shear banding, suggesting an important role of shear banding and deformation twinning in this texture transition.

The 3D printed sample is cold rolled to 10% and 30% reduction in thickness. The printing induced cellular/columnar boundaries with dislocations of complex Burgers vectors, on one hand, act as an obstacle to dislocation motion and deformation twinning, but on the other hand, facilitate nucleation of dislocations and deformation twinning. Consequently, multiple sets of deformation twins form and a strong interaction between dislocations and deformation twins are commonly observed in the

3D printed sample, contributing to the higher strength in printed than in conventionally manufactured 316L.

No recrystallization is observed in the as-printed sample during annealing at 850 °C. However, with an additional 30% cold rolling, recrystallization is observed to occur readily and progress faster than in 30% cold rolled conventionally manufactured 316L. Voids appear to be unavoidable in 3D printed samples. Effects of voids on the recrystallization behaviour is thus investigated here by phase field simulations and ex-situ EBSD observations. The voids and the deformed/printed microstructure are found to significantly affect the local recrystallization boundary kinetics.

## Resumé

Additiv fremstilling (eller 3D-printning) af metalliske komponenter er for nylig blevet meget populær, da processen muliggør fremstilling af komponenter uden spild af materiale samt komplekse designs, som ikke er let opnåelige ved konventionel fremstilling. Når 3D-printede metalliske komponenter er i brug, vil de ofte blive deformeret og/eller udsat for høje temperaturer. Det er derfor nødvendigt at undersøge hvordan mikrostrukturen i 3D printede prøver ændrer sig under plastisk deformation og rekrySTALLISATION – dette er de to overordnede mål i denne afhandling. Rustfrit stål 316L er valgt som et eksempel i dette arbejde, fordi dette materiale er relativt nemt at printe uden der introduceres for mange porøsiteter. 'Laser powder bed fusion' (L-PBF) er valgt som fremstillingsmetode og prøverne er printede ifølge den gængse industrielle standard. Forskellige karakteriseringsteknikker, herunder elektronmikroskopi: scanning elektronmikroskopi/elektron tilbagespredningsdiffraktion (SEM/EBSD) og transmissionselektronmikroskopi (TEM), røntgendiffraktion (XRD) og røntgen absorptions kontrast tomografi, Vickers hårdhedsmålinger og trækprøving er blev anvendt.

Som første del af projektet blev konventionelt fremstillede 316L prøver deformeret ved koldvalsning, og mikrostrukturen såvel som teksturudviklingen blev fulgt følges som funktion af deformationsgraden. Formålet med dette studie var at etablere en solid basis for sammenligning med den tilsvarende udvikling i de 3D printede prøver. Ud fra dette indledende arbejde kunne det konkluderes at deformationsstrukturen er en Taylor-lattice struktur ved lave deformationer. Ved højere tøjning udvikles deformationstvillinger og forskydningsbånd. Ved valsning til mere end 30% reduktion sker der en martensittransformation hovedsageligt i forskydningsbåndene. Tvillingdannelsen fører til en teksturændring fra kobber til kobber-tvilling orientering. En teksturovergang fra kobber til messing typen forekommer samtidigt med dannelsen af forskydningsbånd. Det er derfor sandsynligt at netop forskydninger og tvillingdannelse er vigtig for denne teksturovergang.

Den 3D-printede prøve blev koldvalset til 10 % og 30 % reduktion i tykkelse. De printede mikrostrukturer er opbygget af en cellestruktur, med komplekse Burgersvektor dislokationer. Denne struktur virker på den ene side som en hindring for

dislokationsbevægelse og tvillingudbredelse, men på den anden side stimulerer strukturen dannelsen af dislokationer og deformationstvillinger. Som følge heraf dannes flere sæt deformationstvillinger og der er en stærk interaktion mellem dislokationer og deformationstvillinger, hvilket bidrager til den højere styrke i printet end i konventionelt fremstillet 316L.

Den printede prøve rekrytalliserer ikke ved 850 °C. Men hvis den printede prøve vales 30%, sker rekrytallisationen hurtigere end i en tilsvarende konventionelt fremstillet prøve. Porøsiteter er uundgåelige i 3D-printede prøver. Virkninger heraf på rekrytallisation blev undersøgt ved hjælp af 'phase field' simuleringer kombineret med ex-situ EBSD-observationer. Resultaterne viste at porer såvel som den deformerede/printede mikrostruktur påvirker den lokale rekrytallisations kinetik signifikant.

## Acknowledgements

I would like to thank my main supervisor, Senior Scientist Tianbo Yu, for his continuous support throughout the 3 years. His extensive knowledge and impressive patience helped me solve most of the problems I had during experiments, analysis and writing. His elegance as always sets a great example for me to follow in my whole life. I am grateful to my co-supervisor Professor Dorte Juul Jensen, who is full of energy and novel ideas, for her guidance through this PhD project. There wouldn't be this thesis without her reliable support, impressive availability and encouragement as always. Her curiosity in science always inspires me and reminds me of what my original intention is and where I am going. I would also like to thank the late Dr. Niels Hansen, for sharing his insights on research and his wisdom about future and life. It has been a pleasure and a worth-to-remember time, although it unfortunately didn't last long.

I would also like to thank Professor Nele Moelans and Dr. Vishal Yadav, for their acceptance and supervision during my external stay at KU Leuven. Those nice talks and meetings, helped me gain much knowledge and finish my first paper about phase field simulations, although my time at Leuven was short due to the Covid-19 pandemic. I would like to thank Yinglun Zhao and his wife Sijia Bao for their warm welcome and accompany, making my time at Leuven joyful.

I would like to thank Professor Xiaoxu Huang for bringing me printed samples and powders all the way from Sweden to China and to Denmark. Many thanks to Professor Grethe Winther and Flemming B. Grumsen for their help with my X-ray diffraction experiments. Many thanks to colleagues Yubin Zhang, Xiaodan Zhang, Chuanshi Hong, Runguang Li, Lichu Zhou, Daniel Cardenas del Rio and Adam Alexander Lindkvist for their help every time. Special thanks to the skillful technicians, Gitte Christiansen, Lars Lorentzen, and Elias Meskouk Mathiesen.

Also thanks to Shuangyang, Tianbo, Chaoling and Jun for their warm parties and delicious food, which bring much fun for the holidays in Denmark. I would like to thank my friends Xiaoming, Xuan, Faping, Linfei, Guoqiang, Danyang, Xiuchuan,

Tianzhao, Wenxin, Guangni, Yushi, Xiaojuan and Xiaoying, those who have brought valuable entertainment to my life in Denmark.

Finally, I would like to thank my family and my girlfriend for their constant support and understanding during my PhD.

## Publications

- I. **C. Zhang\***, D. Juul Jensen, T. Yu, Microstructure and Texture Evolution During Cold Rolling of 316L Stainless Steel, *Metall. Mater. Trans. A.* (2021) 52 (9), 4100–4111.
- II. **C. Zhang\***, D. Juul Jensen, T. Yu\*, “Effects of Initial 3D Printed Microstructures on Subsequent Microstructural Evolution in 316L Stainless Steel” (**In preparation**)
- III. **C. Zhang\***, V. Yadav, N. Moelans, D. Juul Jensen, T. Yu, “The Effect of Voids on Local Boundary Migration During Recrystallization - A Phase Field Study” *Scr. Mater.* (**Under review**)
- IV. **C. Zhang\***, V. Yadav, N. Moelans, D. Juul Jensen, T. Yu, “Boundary Kinetics in 3D printed 316L- A Comparison between Phase Field Simulation and Experimental Observation (**In preparation**).



# Contents

<b>Preface</b> .....	i
<b>Abstract</b> .....	iii
<b>Resumé</b> .....	v
<b>Acknowledgements</b> .....	vii
<b>Publications</b> .....	ix
<b>Introduction</b> .....	1
<b>Chapter 1: Background</b> .....	3
1.1 Status of 3D Printing .....	3
1.1.1 Printed microstructure .....	4
1.1.2 Voids .....	6
1.1.3 Residual stress.....	7
1.2 Plastic deformation.....	8
1.2.1 Deformation of conventionally manufactured 316L .....	9
1.2.2 Deformation of 3D printed 316L .....	10
1.3 Recrystallization.....	11
1.4 Phase field simulation .....	14
<b>Chapter 2: Methodology and work outline</b> .....	17
2.1 Methodology .....	17
2.1.1 Materials .....	17
2.1.2 Cold rolling .....	18
2.1.3 Annealing.....	19
2.1.4 Microstructure Characterization.....	20
2.1.5 Mechanical property.....	22
2.1.6 Phase Field Simulation .....	23
2.2 Motivation and specific outline of the thesis .....	25
<b>Chapter 3: Deformation behaviour of conventionally manufactured 316L</b> .....	27
3.1 Introduction .....	28
3.2 Experimental.....	29
3.3 Results .....	30
3.3.1 Microstructure.....	30
3.3.2 Discussion.....	40
3.4 Conclusion .....	46
<b>Chapter 4: Deformation behaviour of 3D printed 316L</b> .....	49
4.1 Introduction .....	50
4.2 Experimental.....	52
4.3 Results .....	53
4.3.1 Microstructure of the as-printed sample (P-0) .....	53

4.3.2	Microstructure after 10% reduction (P-10%) .....	56
4.3.3	Microstructure after 30% reduction (P-30%) .....	59
4.3.4	Hardness variation.....	65
4.4	Discussion .....	65
4.4.1	Deformation of 3D printed 316L samples .....	65
4.4.2	Orientation dependence of deformation twinning.....	69
4.5	Conclusion.....	71
<b>Chapter 5: Annealing behaviour of 3D printed 316L .....</b>		<b>73</b>
5.1	Recrystallizing microstructure of 316L.....	73
5.1.1	C-30% .....	73
5.1.2	3D printed 316L; P-0 and P-30% .....	74
5.1.3	Mechanical properties .....	78
5.2	Voids in 3d printed 316L.....	79
5.3	Effect of voids on recrystallization behaviour of 3D printed samples .....	82
<b>Chapter 6: Conclusion and outlook .....</b>		<b>91</b>
<b>Bibliography .....</b>		<b>94</b>
<b>Appendix A .....</b>		<b>111</b>
<b>Appendix B.....</b>		<b>113</b>
<b>Appendix C .....</b>		<b>114</b>

# Introduction

---

During the last few decades, 3D printing or additive manufacturing has been developed to manufacture metallic components. Austenitic stainless steel 316L is a widely used engineering material due to its excellent corrosion and oxidation resistance and good formability. 316L stainless steel samples and components with decent properties have been successfully manufactured by 3D printing. Due to the fast heating and cooling rate as well as the complex thermal cycles, the printed microstructure is quite different from conventionally manufactured microstructures. The printed microstructure is influenced by the printing process and it determines the properties of the printed samples. Understanding the printed microstructure is thus of significance for *both* the development of 3D printing techniques and the practical application of printed components.

Typical printed microstructures consist of irregular domains with large orientation spreads, cellular and columnar sub-grain structures and elemental segregation at dislocation boundaries (all depending on the printing parameters). However, it is unclear how the printed microstructure evolves during annealing and during applications where the printed components may be exposed to plastic deformation. Little work has been reported on these points although it is important for the applications of printed products. Therefore, there is a need for detailed characterization and understanding of the printed microstructures and their development during post-printing annealing and when mechanically loaded, i.e., an understanding of the dynamics of different types of boundaries. This is in particular important because the printed microstructures, as mentioned above, may deviate significantly from those in conventionally manufactured components and thus their boundary dynamics may be different.

One objective of this study is thus to understand the evolution of printed microstructure during deformation by following the microstructural evolution. To

have a solid basis for such an analysis, the microstructural evolution of conventionally manufactured 316L during deformation, was characterized first. The evolution of the printed microstructure during deformation was then analysed by comparing to conventionally manufactured 316L.

The other objective is to investigate the effects of voids during annealing. Voids appear to be unavoidable in 3D printed samples, even when the printing parameters are carefully controlled and optimized. It is not known how the voids affect the microstructural evolution during post-printing heat treatments or during applications in high temperature environments. The topic is of importance *both* for establishing efficient post-printing annealing treatment and for understanding how interior surfaces, surrounding voids, affect recrystallization. Thus, the objective is to investigate the effects of voids on boundary migration during recrystallization by both experimental observations (ex-situ) and phase field simulations.

This thesis is structured as follows: Chapter 1 summarizes background knowledge related to the present work; Chapter 2 describes the applied methodologies and outline of the thesis; Chapter 3 presents results obtained during this work on the microstructural evolution of conventionally manufactured 316L during deformation; Chapter 4 analyses how the printed microstructure develops during plastic deformation including mechanical properties (compared to those observed in conventionally manufactured samples, including mechanical properties); Chapter 5 focusses on the recrystallization behaviour of 3D printed 316L, including phase field simulations of the effect of voids on boundary migration during recrystallization; Chapter 6 gives the conclusion and outlook.

# Chapter 1: **Background**

---

## **1.1 Status of 3D Printing**

3D printing or additive manufacturing (AM) has drawn extensive attention during the last four decades due to its unique advantage in design freedom and ability of net-shape manufacturing components with complex shapes [1–3]. 3D printing has been applied for manufacturing of various materials: polymers, ceramics and metallic materials [4–6]. Among the metallic materials, Ti-6Al-4V and stainless steels, are probably the most widely used, which find applications in aerospace, automotive, nuclear and medical industries [7–12].

Laser powder bed fusion (L-PBF), which is a commonly used method for metal printing, is taken as an example here to illustrate the 3D printing process. In general, L-PBF is a layer-by-layer manufacturing technique using a computer-controlled laser to melt powder and allowing rapid solidification of the melt pool (as illustrated in Figure 1-1). The characteristics of L-PBF are the fast heating and cooling rate ( $10^6\sim 10^8$  K/s) as well as the complex thermal cycles due to the layer-by-layer processing mode. The printed microstructures are thus rather complex and highly dependent on the printing parameters, e.g. the laser input power, scan speed, and scanning strategy [13–19]. Other features such as voids and residual stress also affect the performance of 3D printed components. In the following sections, these features in 3D printed 316L are described in some detail. Different words are used in the literature to describe voids in printed samples, e.g. holes, voids, and pores. In the following, I will preferentially refer to them as voids.

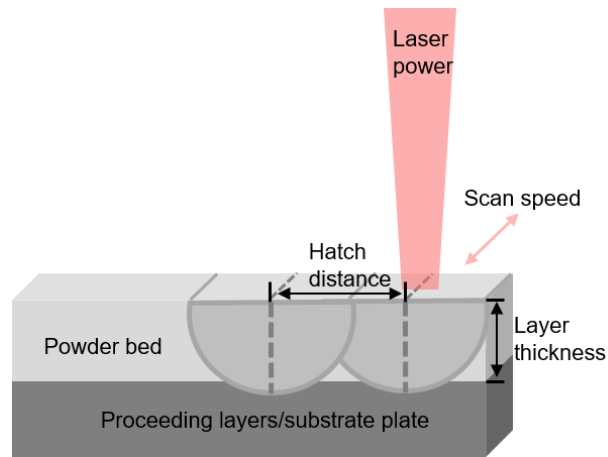


Figure 1-1 Schematic diagram of the L-PBF process, showing the printing parameters (input laser power, scan speed, hatch distance and layer thickness).

### 1.1.1 Printed microstructure

A typical printed microstructure, as shown in Figure 1-2, consists of irregular domains with large orientational spreads, cellular/columnar sub-grain structures, and maybe elemental segregation at dislocation boundaries. The irregular domains can cross several layers due to re-melting of previous layers and the consecutive epitaxial growth. The shape of the domains is thus related to the melt pool shape.

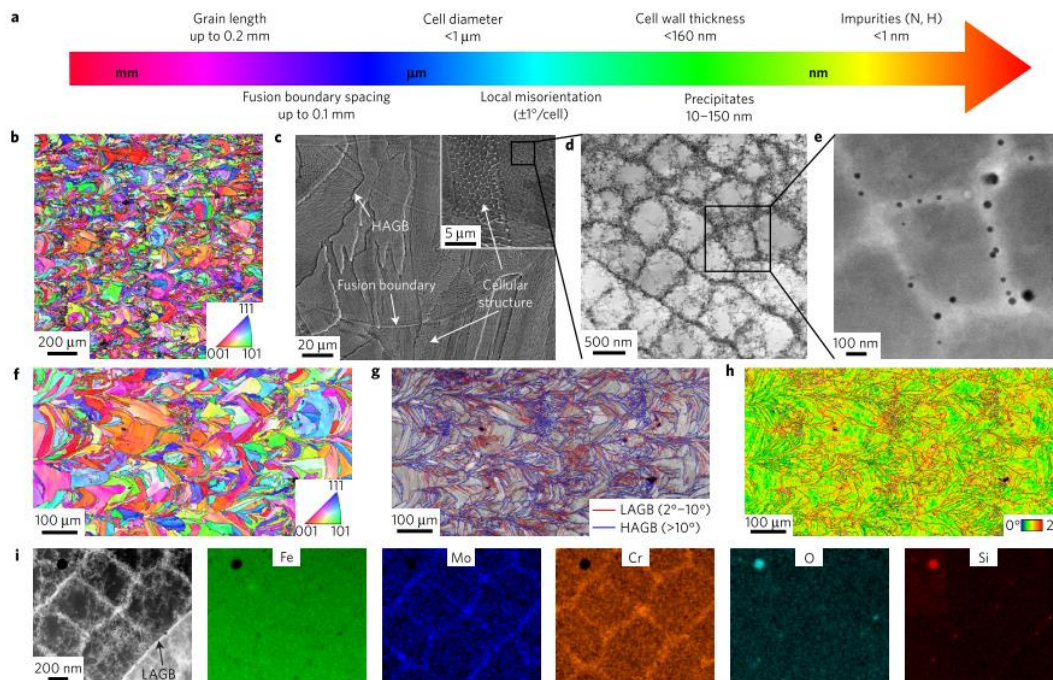


Figure 1-2 Typical microstructures of 3D printed 316L, reproduced from [20]. (a) A schematic illustration of the various microstructural length scales relevant for printed 316L. (b) A cross-sectional view by an electron backscatter diffraction (EBSD) inverse pole figure map. (c) A

cross-sectional scanning electron microscopy (SEM) image. (d) A cellular structure induced by printing. (e) A high-angle annular dark-field (HAADF) scanning TEM (STEM) image of (d), showing the particle segregation at the cellular boundaries. (f-h) EBSD information, showing the distribution of orientations and low angle and high angle boundaries. (i) Elemental segregation.

The origin of the cellular/columnar sub-grain structures is not fully clear yet. Several mechanisms have been proposed. The micro-segregation mechanism suggested that the constitutional stress due to micro-segregation in the inter-dendrite region causes distortion that is accommodated by dislocations [21]. However, the constitutional stress may be insufficient to generate dislocation densities of about  $10^{14} \text{ m}^{-2}$  typical of in 3D printed samples. Other mechanisms suggested that thermal stress, precipitation networks and dendrite misorientation are the driving force for the formation of dislocations [22–24]. However, a recent study [25] suggests that it is the local thermal expansion/shrinkage in a constrained medium (in other words thermal stress) that mainly contributes to the formation of dislocations, rather than other factors mentioned above.

The cellular/columnar structure has been reported to be in a 3D cylindrical shape, like dendrites [26]. The misorientation angle across the cellular/columnar boundaries is typically less than  $1^\circ$  [20] and therefore the cellular/columnar boundary is considered as a weak obstacle to dislocation motion and deformation twinning. Liu et al. [24] have suggested that the cellular/columnar boundary contains dislocations with complex types of Burgers vectors, which promote the nucleation of both dislocations and deformation twins. During deformation, extensive interaction between dislocations, twins, and cellular/columnar boundaries strongly increases the strength of printed samples [27]. It has been reported that the cellular/columnar boundaries may be decorated by elemental segregation, which contributes to the stability of the cellular/columnar structure at temperature as high as  $900^\circ\text{C}$  for 10 min in 3D printed 316L [27]. In addition, the segregation may hinder the motion of dislocations and further increase the ability of dislocation storage, and thus additionally strengthening the printed samples.

For cubic metals, the  $\langle 001 \rangle$  crystallographic direction is the easy growth direction during solidification [28] and the solidifying domains tend to grow by aligning the  $\langle 001 \rangle$  direction to the maximum thermal gradient, i.e. the direction perpendicular to

the melt pool boundary. This means, the orientation of the solidified domains is highly dependent on the melt pool geometry. It is therefore possible to control the texture of printed samples by manipulating the printing parameters. For example, in cubic metals, the  $\langle 011 \rangle$  texture is usually formed when using the unidirectional laser scanning strategy whereas a  $90^\circ$  rotation between adjacent printing layers generally leads to the  $\langle 100 \rangle$  texture [14]. For industrial printing, a  $67^\circ$  rotation between adjacent layers is usually applied to avoid a strong texture and to make the directions in the scanning plane (normal to building direction) equivalent.

### 1.1.2 Voids

Even when printing parameters have been carefully optimized to manufacture 316L stainless steel samples with nearly full density ( $>99.7\%$ ), voids still appear to be unavoidable even in the inner part of the sample. The voids formed during 3D printing can be classified into 3 types [29]: lack of fusion (LOF) voids, keyhole voids and gas entrapped voids. Of these, the LOF void is typically related to insufficient input power density, insufficient overlap of the melt pools (too large a hatch distance), and significant particle spatter leading to particles which are not melted during laser scanning [30]. Therefore printing parameters including laser beam fluctuation, gas flow, and materials characteristics [31] all affect the formation of the LOF voids. Only by careful choice of printing parameters, LOF voids may be avoided.

The keyhole voids are related to vapour depressions and the subsequent fluctuation of the melt pools (as shown in Figure 1-3), during which pinched off voids may be transferred to the melt pool where these gas voids are subject to both Marangoni force [32] and buoyancy force. For 316L, the Marangoni and buoyancy force are acting in opposite directions. If the Marangoni force is larger than the buoyancy force, the gas voids may remain in the melt pool and consequently remain also in the solidified components. If the opposite is the case, the gas voids are driven out of the melt pool. In practice, keyhole voids tend to form when high input power and low scanning speed are applied. Accordingly, Cunningham et al. [33] found that the angle  $\theta$ , defined as  $\tan\theta = \frac{V_w}{V_d}$  ( $V_w$ : laser velocity and  $V_d$ : drill rate depending on power density), determines the formation of keyhole voids. It is thus also possible to reduce or even avoid keyhole voids via carefully control of printing parameters.

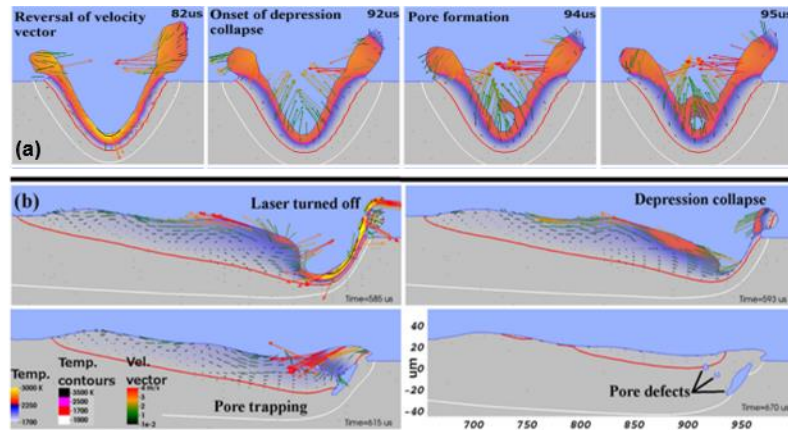


Figure 1-3 The formation and collapse of the depression during laser indentation and movement, showing the temperature distribution and convection velocity in the melt pool. (a) 2D cross section view; (b) 2D longitudinal section view (reproduced from [29]).

The gas entrapped voids may be the hardest to avoid during 3D printing. Even when “perfect” printing parameters are applied, gas entrapped voids still exist in the printed samples [34]. The origin of the gas entrapped voids is either the gas in the printing chamber or the gas entrapped in the powder (particular the powder made by gas atomization), which may remain in the melt pool during printing, as has been experimentally observed in [30].

Voids are reported to be detrimental to the mechanical properties e.g. Young’s modulus, tensile strength, fatigue properties [35] and corrosion properties [36]. To reduce the effects of voids, post-printing treatments like hot isostatic pressing (HIP) are often used [37].

### 1.1.3 Residual stress

Residual stresses are another critical issue for printed components. The stresses are related to the local melt and solidification of the powders and are thus dependent on printing parameters such as scanning strategy and beam diameter [38]. The residual stress can cause dimensional inaccuracy, distortion and even cracks in the printed components. It has been reported that the residual stress can reach values as large as 500 MPa in printed 316L samples, exceeding the yield strength of cast 316L [39]. In addition, residual stress has been reported to affect the fatigue properties and stress corrosion cracking [40,41]. To reduce the effects of residual stress, post-printing annealing is often used [39].

## 1.2 Plastic deformation

Deformation mechanisms have been extensively investigated for metals and alloys both in single crystal and polycrystalline samples, e.g. [42–47]. Stacking fault energy (SFE) is an important parameter when it comes to the understanding of the deformation behaviour. For metals with high SFE like aluminium, the deformation mechanism is generally dislocation slip and therefore the stored energy is mainly in the form of dislocations and dislocation walls. Dislocation motion and interaction together shape the deformed microstructure during deformation. An example of a cell block structure formed in aluminium at low strain is shown in Figure 1-4 [48]. For more details about the formation mechanism of such a deformed microstructure, readers are referred to the earlier work by the Risø group [45,48–50]. For face-centred cubic (fcc) metals with low SFE, dislocations tend to dissociate into partial dislocations (Shockley partials) and cross slip is difficult. In that case, it is observed that planar gliding is energetically favourable at low strains and deformation twinning tends to occur at high strains. For some metals and alloys with very low SFE, martensite transformation also occurs during plastic deformation [51].

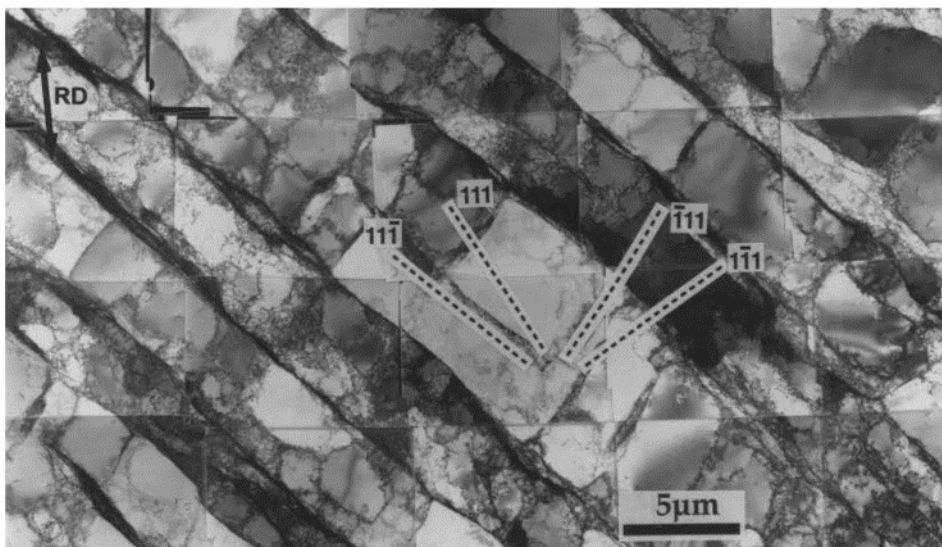


Figure 1-4 A cell block structure in aluminium cold-rolled to 10% reduction in thickness taken from the longitudinal plane view, reproduced from [48].

Texture evolution during plastic deformation is also of interest. The texture transition from the Copper type to the Brass type (from  $\beta$  fibre to  $\alpha$  fibre as shown in Figure 1-5) in fcc metals has been a long-standing issue but reasons for the texture transition is not yet agreed upon. Wasserman and Hirsch et al. [52,53] firstly explained

the texture transition in fcc metals like copper alloys as a result of deformation twinning. However, Leffers and Ray [54] argued that the fraction of deformation twinning is too low to account for this texture transition and claimed that the associated deformation should be the reason for texture transition according to the Sach's model. Subsequent studies, e.g. [55,56], suggested that the texture transition is related to micro-shear banding. As this thesis deals with 316L austenitic stainless steel, the next section describes in detail the formation of the deformed microstructure in this material.

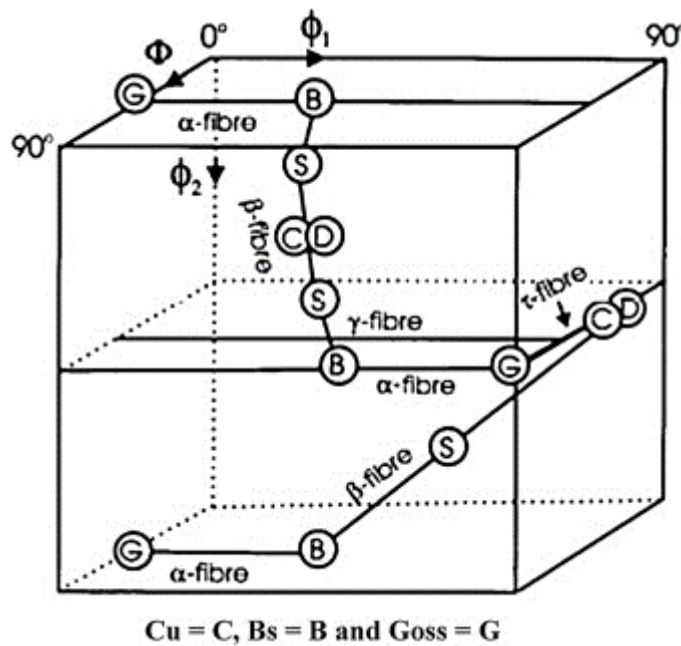


Figure 1-5 Schematic diagram showing the important texture component and groups (i.e. fibres) for rolled fcc metals (reproduced from [57]).

### 1.2.1 Deformation of conventionally manufactured 316L

316L austenite stainless steel possesses good corrosion resistance, good formability and a high work hardening rate. It has thus been widely used as an engineering material in automotive, biomedical, and nuclear industries [9]. However, the yield strength of cast 316L is low. Thermomechanical processing, i.e. deformation and annealing, is therefore usually carried out before the metal is used in practical applications. For example, Yan et al. [58] reported that by dynamic plastic deformation and annealing, a combination of yield strength/elongation-to-failure of 1055 MPa/5.2% was achieved. Later Li et al. [59] reported similar yield strength of 1 GPa but a significantly higher elongation-to-failure of 20% via simple cold rolling to 85% followed by annealing at 750 °C for 10 min. During deformation, deformation twinning typically occurs [60,61]

due to the low SFE. At medium to high strains, twin-matrix lamellae form followed by micro-shear banding, which is observed to erode the twin-matrix lamellae, forming diamond shaped nanotwin bundles [58]. Martensite transformation starts to be observed at around 30% cold rolling and the fraction can increase to about 20% after 80% cold rolling [62,63]. At these strains the twinning-induced plasticity (TWIP) and transformation-induced plasticity (TRIP) effects strongly improve both the strength and ductility [63–67]. While many papers deal with the microstructure and mechanical properties of 316L deformed to high strains, there is little work reporting the details of the microstructural evolution at small deformation strains. In other fcc metallic materials with low SFE, e.g. brass, planar glide of dislocations is favoured while the 3D motion of dislocation, e.g. cross slip, is inhibited, forming a Taylor lattice structure [68]. It is thus of interest to investigate if 316L follows this pattern.

Considering the extensive work focussing on thermomechanical processing of 316L, it is surprising that there is so little published on the correlation between the microstructure and texture evolution. Included in this thesis is a detailed characterization of the microstructure and texture as a function of rolling reduction for conventionally manufactured samples and the results are presented in Chapter 3 (manuscript I). This work provides a solid basis for investigating the deformation behaviour of 3D printed 316L stainless steels.

### **1.2.2 Deformation of 3D printed 316L**

As has been mentioned above, the printed microstructure is far away from equilibrium and this ‘new’ microstructure is not observed after conventional manufacturing. The printed material is thus expected to show a different deformation behaviour as compared to that of the conventionally manufactured material. The high density of cellular/columnar boundaries has been reported to be the main contributor to the high strength and good ductility of 3D printed 316L [21]. Wang et al. [20] reported that the cellular/columnar boundaries together with elemental segregation facilitate dislocation storage and deformation twinning and therefore the tensile strength is increased. In-situ TEM observations revealed that the cellular/columnar boundaries are weak obstacles to both dislocation motion and deformation twinning [24]. Moneghan et al. [69] investigated the deformation mechanism and suggested that the cellular/columnar structure can delocalize strain localization and increase the defect tolerance. However, little work has so far been published, giving a detailed

characterization and quantification of the microstructural evolution during plastic deformation, e.g. by TEM observations. Such work is considered necessary because the cellular/columnar structure is on the sub-micron scale and the quantification of the dislocations and deformation twins thus requires high-resolution characterization techniques. Therefore, in this thesis a detailed TEM observation of 3D printed 316L was carried out for a series of cold rolling reductions to quantify the microstructural evolution and to better understand the mechanical properties, by comparing to the conventionally manufactured 316L. Investigations of deformation of printed samples are of utmost relevance as many printed components are likely to be exposed to mechanical loading while they are in use. Cold rolling was chosen here to deform the samples because it is a well-controlled deformation procedure and the effects of the initial printed microstructures can be extracted by comparing the microstructural evolution to that in conventionally manufactured samples. The results are presented in Chapter 4 (manuscript II).

### **1.3 Recrystallization**

Recrystallization is an important mechanism typically happening during thermomechanical processing, which has been used for centuries to control the microstructure and thereby the properties [70,71]. The driving force for recrystallization is the consumption of the deformation induced stored energy by nucleation and migration of high angle boundaries, which distinguishes recrystallization from the other two phenomena occurring during annealing: recovery and grain growth. Recrystallization is generally divided into two processes: nucleation and growth. During nucleation, almost defect-free crystals form in the deformed microstructure and these crystals grow into the deformed microstructure by boundary migration during growth. The nucleation and growth may take place simultaneously—while already developed nuclei grow, new nuclei develop elsewhere in the deformed microstructure [72].

#### **1.3.1 Nucleation**

The nucleation of recrystallization implies a process generating a region with low dislocation density surrounded (fully or partially) by a high angle boundary with high mobility. Three mechanisms of recrystallization nucleation in single phase materials have been proposed [73–78]:

- i) *nucleation by migration of pre-existing high angle boundary (SIBM – strain induced boundary migration)*
- ii) *sub-grain boundary migration (Cahn-Cottrell model)* suggests that the sub-grain boundary migrates into the deformed matrix and simultaneously the boundary misorientation is increased (usually observed for recrystallization at high temperature)
- iii) *sub-grain coalescence* suggests that a sub-grain boundary disappears due to the rotation of one sub-grain towards a neighboring one and therefore the two sub-grains merge into a large one. The misorientation of sub-grain boundaries is increased with sub-grain coalescence.

Nucleation of recrystallization is important for the microstructural evolution but is not the focus for the present thesis.

### 1.3.2 Growth

During recrystallization, growth by boundary migration is of practical interest since it is critical for the microstructural evolution. The boundary kinetics is generally described by the following equation:

$$v = MP \tag{1}$$

where  $v$  is the velocity,  $P$  is the driving pressure and  $M$  is the boundary mobility. An underlying assumption here is that the boundary mobility is independent of driving pressure, although there are studies showing the opposite [79]. Humphreys and Hatherly [72] concluded that this formula is generally correct if the driving pressure  $P \ll kT$  ( $k$  is the Boltzmann constant,  $T$  is the temperature in Kelvin). The driving pressure  $P$  is generally assumed to be given by the stored energy in the deformed matrix [72]. However, experiments and simulation results [80,81] have shown that the energy related to the recrystallization boundaries also has to be considered, even though it traditionally was assumed to be negligible compared to the magnitude of the stored energy [82]. This is in particular relevant when large boundary curvatures, in the form of retrusions and protrusions (an example is shown in Figure 1-6), provide large local driving/dragging force for the recrystallizing boundaries. In such cases it was suggested [80] that equation (1) should be revised to:

$$v = M(P_{rex} + P_{curve}) \tag{2}$$

Simulations by molecular dynamics and phase field show that not only the local variation in stored energy but also the local arrangement of dislocations and sub-grain boundaries affect the boundary curvature and thereby the boundary kinetics [83–85]. Precipitates/particles drag boundaries slowing down the migration due to the Zener pinning effect [86] and therefore affect the recrystallization microstructure. There has been extensive experimental and theoretical research on the pinning effect of particles on boundary migration during grain growth (occurring after recrystallization) [87–93]. It is worth noting that large particles may facilitate the nucleation of recrystallization, i.e. particles stimulate nucleation [94].

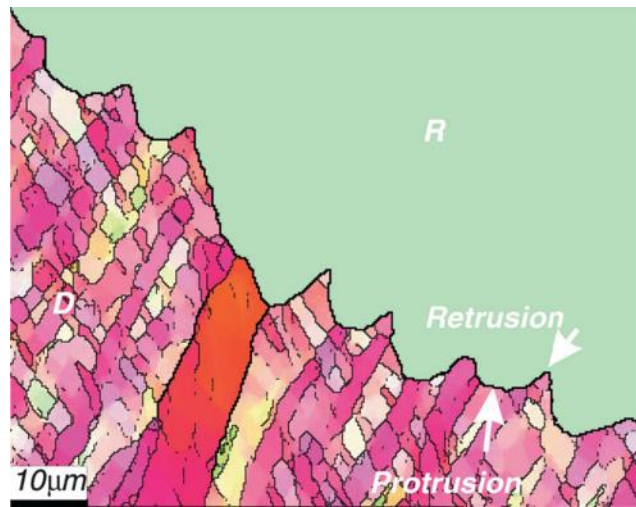


Figure 1-6 Large boundary curvatures in the form of protrusion and retrusion observed during recrystallization in pure aluminium annealed at 250 °C for 10 min (reproduced from [81]). R: recrystallizing grain, D: deformed microstructure.

Boundary mobility is related to the boundary characteristics (misorientation and boundary plane), temperature [79] and impurities [95]. In general, the mobility of a high angle boundary is higher than that of a low angle boundary. For boundaries with very low misorientation angles, the mobility may however decrease with increasing misorientation angle [79]. The boundary plane also affects the boundary migration. For example, the  $\langle 111 \rangle$  high angle boundaries are commonly observed to be the most mobile [96].

The effect of temperature on mobility has been studied for a wide range of materials by both experimental work and atomistic simulations [97–99]. There are experimental data, suggesting an Arrhenius relation between mobility and temperature [99,100]. However, data extracted from atomistic simulations show various temperature

dependencies of the mobility of individual boundaries. For example, Janssens et al. and Homer et al. [99,101] found that the boundary mobility may increase or decrease with increasing temperature, or may be temperature independent or may even have multiple peaks. Recent work by Chen et al. [97,102] reported that the mobility should be a second order tensor considering that the boundary migrates not only along the normal direction of the plane but also along directions in the boundary plane. This interpretation appears to support the disconnection mechanism and provides consent with experimental results.

The grain boundary mobility has been a long-standing issue in recrystallization and grain growth. However, the development of advanced 3D characterization techniques [103] and the increased computing ability provide inspiration to revisit the problem. Recently, there have been simulations of recrystallization using, e.g. phase field, molecular dynamics, and Monte Carlo methods, providing novel insights to the understanding of boundary mobility [85,97]. In the following, the phase field approach shall be summarized, as this is the simulation method applied in the present thesis.

#### **1.4 Phase field simulation**

Phase field (PF) simulation for studies of the microstructural evolution has been developed during the last two decades [104–106]. “The key idea of PF method is the description of the interface using continuous fields” as phrased by Tournet et al. [107] in a recent review. The discontinuities across the interface are thus smeared out and replaced by a continuous and smooth variation of phase fields. This treatment renders the PF method a mesoscale simulation approach. It has been widely utilized to investigate phenomena that occur during thermomechanical processing e.g. solidification, precipitation, phase transformation, dislocation dynamics, deformation twinning and crack initiation and propagation, grain growth and recrystallization [85,85,107,108]. There exist several other methods to simulate the microstructural evolution during recrystallization including Monte Carlo, vertex, level-set, front-tracking, cellular automata [88,91–93,109] and molecular dynamics [110]. Here we choose the PF method because it is easy to implement realistic deformation microstructures and use realistic parameters from the experimental results. Recently, the PF model has been successfully applied to study the microstructural evolution during recrystallization, quantifying effects of stored energy, grain boundaries

characteristics and arrangement of dislocation boundaries in the deformed microstructure on the boundary migration during recrystallization [81,85,111–113].

The PF model for recrystallization was firstly introduced by Moelans et al. [114] based on the initial work by Chen et al. [115]. According to the Ginsburg-Landau equation:

$$\frac{\partial \eta}{\partial t} = -L \frac{\partial F}{\partial \eta} \quad (3)$$

where  $\eta$  is the order parameter for recrystallized grains or deformed microstructure, i.e.  $\eta_{rex}$  and  $\eta_{def}$ . The model parameter  $L$  is a kinetic coefficient related to the grain boundary mobility  $\mu_{gb}$  and the diffuse interface width  $\iota_{gb}$  [114]. The free energy function for the system  $F$  is:

$$F = \int_{\Omega} [F_{gb} + F_s] d\Omega \quad (4)$$

where  $\Omega$  is the simulation domain;  $F_{gb}$  is the contribution from grain boundary;  $F_s$  is the stored energy, which can be artificially defined or defined based on input from experimental data. In this thesis, the PF model is further developed to include a void in the recrystallization system to analyse its effect on recrystallization boundary migration.



# Chapter 2: Methodology and work outline

---

## 2.1 Methodology

### 2.1.1 Materials

The 3D printed 316L (P-0) samples were manufactured by laser powder bed fusion (L-PBF) according to the industrial standards. The laser power and scanning speed were set to 370 W and 1.35 m/s, respectively. A 67° rotation between adjacent layers was used to make the X and Y scanning directions equivalent. To improve the surface finish of the samples, a final contour scanning with input power of 120 W and scanning speed of 0.22 m/s was applied. The size of the samples was  $14 \times 3 \times 6 \text{ mm}^3$  in building direction (BD), X, and Y direction, respectively (see Figure 2-1). Larger samples with dimension of  $130 \times 100 \times 2.5 \text{ mm}^3$  were printed using the same printing parameters as P-0 (see Figure 2-1). These samples were finally cut into dog-shaped specimens for tensile test (detailed information about how these samples were treated can be found in Section 2.1.5.2)

The conventionally manufactured 316L used in this work was delivered in a hot rolled condition. It was first solution treated at 1080 °C for 1 h, after which the material was fully recrystallized with a grain size of 26  $\mu\text{m}$  (determined by the line intercept method). This condition is denoted as C-0 in the following. The chemical composition of P-0 is measured by glow discharge optical emission spectroscopy (GDOES) and is listed in

Table 2-1, together with the nominal chemical composition of C-0.

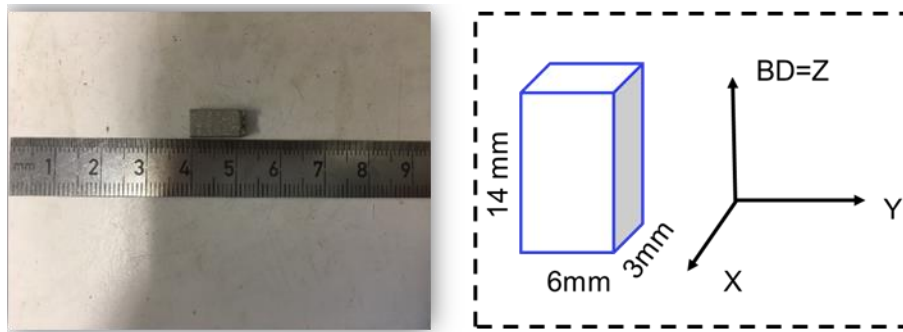


Figure 2-1 A photo and a sketch of a 3D printed sample.

Table 2-1 Chemical composition of P-0 (by GDOES) and the nominal chemical composition of C-0.

%	C	Ni	Fe	Cr	S	Si	P	Mn	Mo
P-0	0.02	13.33	68.75	17.57	0.01	0.75	0.01	0.70	2.41
		±0.07	±0.16	±0.05		±0.02		±0.02	±0.02
C-0	<0.03	10-14	Bal.	16-18	<0.03	<0.75	<0.03	<2	2-3

### 2.1.2 Cold rolling

Cold rolling was chosen as the mode to deform the 3D printed as well as the conventionally manufactured 316L samples. To systematically investigate the microstructural evolution, C-0 was cold rolled to 10%, 30%, 50% and 80% reduction in thickness, denoted as C-10%, C-30%, C-50% and C-80% respectively, for simplicity. The 3D printed samples were cold rolled to 10% and 30% reduction in thickness, denoted as P-10% and P-30%, respectively. During cold rolling, the samples were lubricated by mineral oil and turned upside down between each pass. Inter-pass cooling in water was done to reduce the effects of the temperature increase during rolling. The roll diameter was 340 mm and the ratio of the contact length to the mean height  $L/h$  was kept within the range 2–5 to ensure maximal through-thickness strain homogeneity (see Appendix A for the rolling steps used). The rolling machine used here and an example of a cold rolled sample are shown in Figure 2-2.

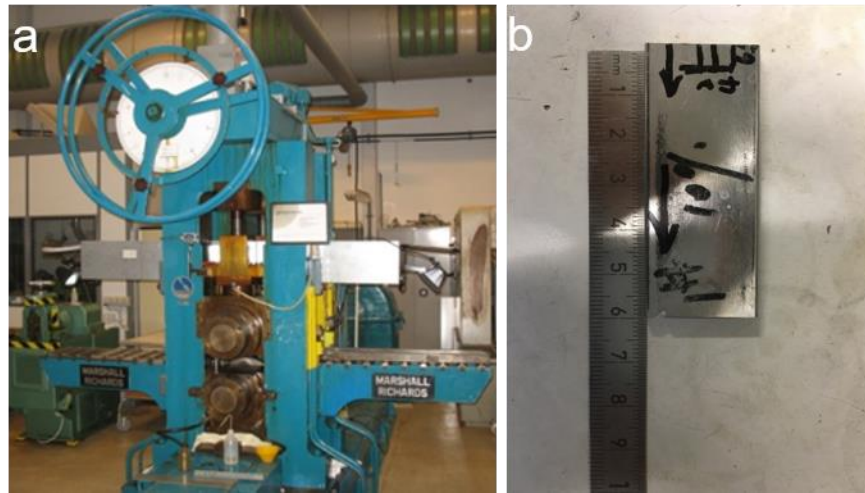


Figure 2-2 Cold rolling. (a) Rolling machine at Risø with the roll diameter 340 mm. (b) A picture of the 10% cold rolled sample (C-10%).

### 2.1.3 Annealing

To analyse the recrystallization kinetics, isochronal annealing of 1 h at temperatures within the range 500~950 °C was first done for the C-30% samples to determine the recrystallization temperature. The samples were annealed in a vacuum furnace at a pressure of 0.02 Pa (to prevent oxidation) and then cooled to room temperature in the vacuum chamber at cooling rates shown in Figure 2-3 a. Based on the hardness shown in Figure 2-3 b, isothermal annealing at 850 °C for 15 min, 30 min, 1 h, 5 h was done for C-30% and printed 316L (both P-0 and P-30% samples) to analyse the recrystallization kinetics. One further annealing step at 900 °C for 5 h was performed to analyse the fully recrystallized microstructure. In addition, one more annealing at 850 °C for 2 h was done for C-30% to better quantify its recrystallization kinetics.

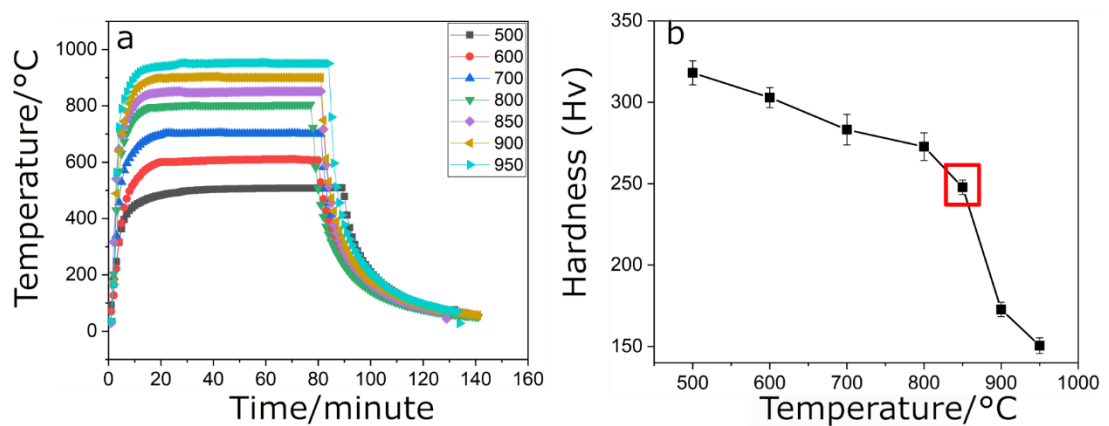


Figure 2-3 Isochronal annealing carried out for C-30% (a) and the corresponding hardness reduction (b).

To analyse the interaction between grain boundaries and voids, ex-situ incremental annealing was done for P-30% (see Table 2-2 Table 2-2 Incremental annealing at 850 °C for P-30% used for an ex-situ experimental investigation of the interaction between moving recrystallization boundaries and voids. Note: A5 was done at 870 °C to bypass effects of thermal grooving.). The sample was firstly annealed at 850 °C for 7 min. Three further annealing steps were done at the same temperature with a holding time of 1 min for each step. To overcome effects of thermal grooving, the final annealing was done with the same holding time but at a higher temperature 870 °C.

Table 2-2 Incremental annealing at 850 °C for P-30% used for an ex-situ experimental investigation of the interaction between moving recrystallization boundaries and voids. Note: A5 was done at 870 °C to bypass effects of thermal grooving.

Annealing Steps	A1	A2	A3	A4	A5
Annealing time	7min	A1+1min	A2+1min	A3+1min	A4+1min at 870 °C (850 °C)

## 2.1.4 Microstructure Characterization

### 2.1.4.1 Microscopy

Samples for light optical microscopy (LOM) were prepared by grinding using SiC papers followed by mechanical polishing using diamond particle suspension (down to 1 µm). The samples were then etched using Kalling etchant for 50 s. Samples for scanning electron microscopy (SEM) were prepared by grinding using SiC papers followed by mechanical polishing. A colloidal silica suspension (0.04 µm) was used for the final polishing step. Both electron channeling contrast (ECC) images (working distance: 9 mm, voltage: 15 kV) and electron backscatter diffraction (EBSD) maps (working distance: 13 mm, voltage: 20 kV) were taken in a Zeiss Supra-35 scanning electron microscope equipped with a field emission gun and an EBSD system from Oxford Instrument. The principles of EBSD technique are illustrated in Figure 2-5. When a focused electron beam hits the polished surface of a tilted sample, a backscatter pattern (Kikuchi pattern) [116] is generated and detected by the detector (CCD camera). This Kikuchi pattern is used for the determination of crystallographic orientation [117,118]. HKL Channel 5 software and the MTEX toolbox [119] (in some cases) were used for the EBSD data processing. In this thesis, all orientation maps are

coloured according to the crystallographic direction of the transverse direction (TD) of the cold rolled samples or the Y direction of as-printed (P-0) samples, unless otherwise stated.

Samples for transmission electron microscopy (TEM) were prepared using a modified window technique in a perchloric acid based electrolyte [120]. TEM observation was done using a JEOL JEM-2100 microscope at an acceleration voltage of 200 kV.



Figure 2-4 Pictures of the electron microscope (Zeiss Supra 35 coupled with Oxford EBSD detector and JEOL JEM-2100) and X-ray microscope (Zeiss Xradia 520 Versa) used in this thesis.

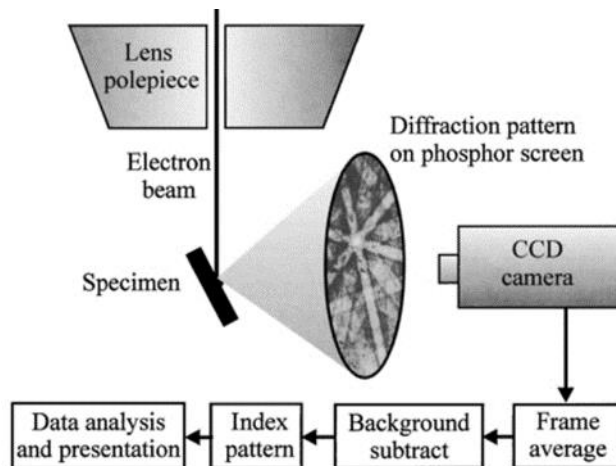


Figure 2-5 Sketch of a typical EBSD installation, reproduced from [121].

#### 2.1.4.2 X-ray measurements

##### Texture measurements

Macro-texture measurements were done for the cold rolled C-0 samples using a Bruker AXSD8 Discover System. Cr was chosen as the X-ray source to reduce the

fluorescence effect. The measurements were done on the rolling plane. The Psi angle (rotating angle around the transverse direction, TD) was set in the range of 0-75° with a step size of 5° and the phi angle (around ND) was set in the range of 0-360° with a step size of 10°. Orientation distribution functions (ODFs) were calculated from three pole figures {111}, {200}, and {220} using the series expansion method with  $l_{max} = 22$  [122]. The pole figure data were processed using the MTEX toolbox [119].

### Phase analysis

The fraction of  $\alpha'$ -martensite in the cold rolled C-0 samples was determined by X-ray diffraction (XRD). To reduce the effect of the rolling texture on the  $\alpha'$ -martensite determination, unlock-coupled scans were carried out with different start angles for theta from 6.5° to 46.5° with an interval of 10°, giving rise to the offset angle Psi between -24.5° and 25°. The penetration depth of the X-rays was calculated by the software developed by Bruker, and found to be in the range of 1.1–5.5  $\mu\text{m}$ . The XRD patterns were obtained by the summation of the intensities over 5 scans. The volume fraction of  $\alpha'$ -martensite was calculated using the standard ASTM E975 method, and the standard error was also obtained based on the 5 scans for each sample condition.

### Porosity analysis

X-ray tomography (using a Zeiss Xradia 520 Versa) was used to characterize the voids inside the printed samples based on absorption contrast. Small cylindrical shaped specimens with cross section size of  $0.5 \times 0.5 \text{ mm}^2$  were prepared by machining and grinding from the as-printed sample (P-0). The voxel size was set to  $0.3 \mu\text{m}^3$ . The data were processed using Avizo software packages and some Matlab codes.

## **2.1.5 Mechanical property**

### *2.1.5.1 Hardness measurement*

Hardness measurement was done using a Struers DuraScan V hardness machine. For the C-0 and cold rolled C-0 samples, the hardness was measured on the RD-ND plane while for the 3D printed samples (P-0 and P-30%), the hardness on both the building plane and the plane containing the building direction were measured. A load of 300 g was used and at least 12 indentations were made for each condition to ensure statistical precision.

### *2.1.5.2 Tensile test*



represents the deformed microstructure, and a region with  $\eta_{rex} = 0, \eta_{def} = 0$  and  $\Phi = 1$  represents the void. The contribution from boundary energy and stored energy are given as:

$$F_{gb} = m[0.25(\sum_{i=1}^p \eta_{rex,i}^4 + \eta_{def}^4) - 0.5(\sum_{i=1}^p \eta_{rex,i}^2 + \eta_{def}^2) + 1.5 \sum_{i=1}^p \sum_{i \neq j} \eta_{rex,i}^2 \eta_{rex,j}^2 + 1.5 \eta_{def}^2 \sum_{i=1}^p \eta_{rex,i}^2 + 0.25] + \epsilon \Phi^2 (\sum_{i=1}^p \eta_{rex,i}^2 + \eta_{def}^2) + \frac{\kappa}{2} (\sum_{i=1}^p |\nabla \eta_{rex,i}|^2 + |\nabla \eta_{def}|^2) \quad (5)$$

$$F_s = f_{def}(x, y) \cdot \phi_{def} = f_{def}(x, y) \cdot \frac{\eta_{def}^2}{\sum_{i=1}^p \eta_{rex,i}^2 + \eta_{def}^2 + \Phi^2} \quad (6)$$

Based on the equations (3-6), the numerical equation is thus:

$$\frac{\partial \eta_{rex,i}}{\partial t} = -L \left[ m \left( \eta_{rex,i}^3 - \eta_{rex,i} + 3\eta_{rex,i} (\sum_{i \neq j}^p \eta_{rex,j}^2 + \eta_{def}^2) \right) - \kappa \nabla^2 \eta_{rex,i} + 2\epsilon \eta_{rex,i} \Phi^2 - \frac{2\eta_{rex,i} \eta_{def}^2}{(\sum_{i=1}^p \eta_{rex,i}^2 + \eta_{def}^2 + \Phi^2)^2} f_{def}(x, y) \right], \quad (7)$$

$$\frac{\partial \eta_{def}}{\partial t} = -L \left[ m \left( \eta_{def}^3 - \eta_{def} + 3\eta_{def} \sum_{i=1}^p \eta_{rex,i}^2 \right) - \kappa \nabla^2 \eta_{def} + 2\epsilon \eta_{def} \Phi^2 + \frac{2\eta_{def} (\sum_{i=1}^p \eta_{rex,i}^2 + \Phi^2)}{(\sum_{i=1}^p \eta_{rex,i}^2 + \eta_{def}^2 + \Phi^2)^2} f_{def}(x, y) \right] \quad (8)$$

where the model parameters  $\kappa$  and  $m$  are related to the grain boundary energy  $\sigma_{gb}$  and the diffuse interface width  $\iota_{gb}$ ,  $\kappa = 3/4 \cdot \sigma_{gb} \cdot \iota_{gb}$  and  $m = 6 \cdot \sigma_{gb} / \iota_{gb}$ . The parameter  $p$  refers to the number of recrystallizing grains.

A standard finite-difference discretization with a central five-point scheme for the spatial Laplacian and explicit time stepping were applied in Eqs. (6) and (7). von Neumann boundary condition was applied in the X and Y directions. Parameters typical for pure Al were chosen here to ease comparison with previous PF simulations of recrystallization in similar microstructures but without voids. The mobility of the recrystallizing grain boundary:  $\mu_{gb} = 6 \times 10^{-14} \text{ m}^4/(\text{J}\cdot\text{s})$ ; the grain boundary energy:  $\sigma_{gb} = 0.32 \text{ J/m}^2$ ; the time step:  $dt = 0.0023\text{s}$ ; order parameters:  $m=22.7 \text{ MJ/m}^3$ ,  $L = 9.46 \times 10^{-7} \text{ m}^3/(\text{J}\cdot\text{s})$ , and  $\kappa=2.03 \times 10^{-8} \text{ J/m}$ ;  $\epsilon=22.7 \text{ MJ/m}^3$ . If parameters typical for 316L had been used instead, the conceptual results for the effect of the void(s) would have been the same.

## 2.2 Motivation and specific outline of the thesis

To have a solid basis to compare the 3D printed samples to, the microstructure and texture evolution in conventionally manufactured 316L is investigated as a function of cold rolling from 10% to 80% in thickness reduction. The microstructures are characterized by electron microscopy, namely SEM/EBSD and TEM. The macro-textures are characterized by X-ray diffraction and are correlated to the microstructure evolution. A systematic characterization of microstructural evolution during cold rolling and the correlation to the texture evolution have not been reported for 316L previously and the results are presented in Chapter 3 (published paper: manuscript I)

To understand the effect of the initial printed microstructure on subsequent deformation, the printed samples are cold rolled to 10% and 30% reduction in thickness reduction. The microstructures are characterized by TEM and SEM/EBSD and compared to that of conventionally manufactured 316L. This type of work is considered essential to understand how printed microstructures and thus properties may evolve when a printed part is in use exposed to external loads. The results are presented in Chapter 4 (manuscript II).

The recrystallization behaviour of printed samples (both P-0 and P-30%) as well as C-30% are studied by annealing for up to 5 h at 850 °C. By comparing the results, effects of the initial printed microstructure are analysed. The results are reported in Chapter 5, but not yet published or prepared in a manuscript format.

Finally, the voids in 3D printed samples are characterized by both SEM (2D) and X-ray tomography (3D). The results are shortly reported in Chapter 5. The aim is to report the types of voids, not to perform an in-depth analysis nor to correlate the 2D and 3D data. The effect of voids on the boundary kinetics during recrystallization is however analysed in detail by both ex-situ SEM/EBSD characterization and phase field simulation. This type of work is highly original and is of genuine importance irrespective of the specific material and printing conditions. The results are presented as part of Chapter 5 (submitted for publication; manuscript III)



# Chapter 3: Deformation behaviour of conventionally manufactured 316L

---

This chapter presents the deformation behaviour of conventionally manufactured 316L. This work is carried out to serve as a basis for the analysis of the thermomechanical behaviour of the 3D printed samples. The results have been published in *Metallurgical and Materials Transactions A* and the manuscript is shown in the following:

## **Microstructure and texture evolution during cold rolling of 316L stainless steel (Manuscript I)**

Chunlei Zhang\*, Dorte Juul Jensen, and Tianbo Yu

Department of Mechanical Engineering, Technical University of Denmark, Kgs. Lyngby DK-2800, Denmark

\*Corresponding author, Email: chzhang@mek.dtu.dk

### **Abstract:**

The evolution of the deformation microstructure and the local crystallographic orientations are investigated for 10%, 30%, 50% and 80% cold rolled 316L austenitic stainless steel strips and the results are related to the overall macro-texture evolution. The microstructures are characterized by scanning electron microscopy (SEM), including electron backscatter diffraction (EBSD), and transmission electron microscopy (TEM). The macro-textures are characterized by X-ray diffraction (XRD) measurements. It is found that the deformation leads to both slip and twinning followed by martensite transformation and shear banding. The deformation twinning occurs on planes with the highest twinning Schmid factors and shows a strong orientation dependence, in the sense deformation twinning occurs preferentially in grains with near Copper orientation rather than Brass orientation. It is furthermore found that the

formation of both deformation twins and shear bands have a significant effect on the texture evolution. The correlations between microstructure, local crystallographic orientations and macro-textures are discussed.

### 3.1 Introduction

The 316L austenitic stainless steel (ASS) is widely used as an engineering material due to its good corrosion resistance and formability plus a high work hardening rate [123]. Deformation and annealing are commonly used to tailor the microstructure and therefore the mechanical properties of 316L [124,125]. For example, recently Yan et al. [58] reported an excellent combination of strength and ductility in 316L ASSs deformed by dynamic plastic deformation (DPD) followed by annealing, and Li et al. [59] reported higher strength and similar elongation in 316L by conventional cold rolling and annealing. The microstructure and texture evolution during deformation are essential to understand the underlying causes for the improvement of mechanical properties. For many face-centred cubic (fcc) metals of medium to high stacking fault energy (SFE), like copper and aluminium, the microstructure and the related texture evolution have been well documented [126–132]. For austenitic steels with low SFE, deformation twinning and/or martensite transformation tend to occur during deformation, which improve both the strength and ductility of the materials, e.g. in twinning-induced plasticity (TWIP) and transformation-induced plasticity (TRIP) steels [63–67]. The microstructure and related texture evolution in TWIP/TRIP steels have been investigated extensively [133–135]. In particular, deformation twinning was found to change the Copper orientation to the twin Copper orientation  $\{552\} \langle 115 \rangle$ . The latter thereafter rotates to the Goss/Brass orientation [53,136], both of which are stable texture components for metals with low SFE after cold rolling. However, similar information on the texture evolution and the related microstructural evolution of cold rolled 316L ASSs is far less frequently reported, although some research has been published in recent years. For example, Chowdhury et al. [137] investigated the texture in cold rolled 316L ASSs, and the microstructure of rolled 316L was reported by Odnobokova et al. [138]. But the correlation between texture and microstructure evolution during cold rolling, to the best of authors' knowledge, is not investigated.

The aim of the present study is thus to characterize *both* the microstructure and texture evolution in 316L ASSs as a function of deformation by cold rolling. The microstructural features, including dislocation boundaries, twins, shear bands, and  $\alpha'$ -

martensite are related to the local crystallographic orientations with the goal of understanding how these local phenomena affect the overall texture and microstructure evolution. Strain accommodation by slip and twinning is discussed based on Schmid factor and modified Taylor criterion analysis.

### 3.2 Experimental

The as received 316L strips (5×25×100 mm<sup>3</sup> in size with the nominal chemical composition 16-18 Cr, 10-14 Ni, ≤2 Mn, 2-3 Mo, ≤0.75 Si, ≤0.045 P, ≤0.03 C, ≤0.30 S, bal. Fe) were first solution annealed at 1080 °C for 1 h and subsequently water quenched to room temperature. The average grain size in this initial condition is 26 μm, which was obtained through the line intercept method. The initial microstructure is fairly homogeneous (see supplementary materials in Appendix B). These strips were cold rolled unidirectionally by a two high rolling mill with a roll radius of 170 mm at room temperature to thickness reductions of 10%, 30%, 50%, and 80%, i.e. von Mises equivalent strains ( $\epsilon_{vm}$ ) of 0.12, 0.41, 0.80, and 1.86 respectively. The contact length to the mean height ratio  $l/h$  were kept between 2.0 and 3.5 to ensure through-thickness homogeneity. The samples were turned upside down and cooled in water between each rolling pass.

A Zeiss Supra 35 field emission gun scanning electron microscope (FEG-SEM), equipped with an HKL electron backscatter diffraction (EBSD) system, was used to characterize the microstructure. EBSD samples were prepared by grinding using SiC papers followed by mechanical polishing. A colloidal silica suspension (0.04 μm) was used for the final polishing step. Transmission electron microscopy (TEM) investigations on the longitudinal sample section, containing the rolling direction (RD) and the normal direction (ND), at the thickness centre of all samples were performed using a JEOL JEM-2100 microscope at an acceleration voltage of 200 kV. Foils for the TEM investigations were prepared by a modified window technique in a perchloric acid based electrolyte [120].

Macro-textures were measured by X-ray diffraction (XRD) using a Bruker AXSD8 Discover XRD System. Cr was used as X-ray source to avoid fluorescence effects. The measurements were done on the rolling plane covering a sample area of 30×10 mm<sup>2</sup>. The Psi angle (rotating angle around the transverse direction, TD) was set in the range of 0-75° with a step size of 5° and the phi (angle around ND) was set in the range of

0-360° with a step size of 10°. Orientation distribution functions (ODFs) were calculated from three pole figures {111}, {200}, and {220} using the series expansion method with  $l_{max} = 22$  [122]. The pole figure data along with the EBSD data were processed by the MTEX tool box [119]. The  $\alpha'$ -martensite fraction was also determined by XRD measurements. To reduce the effect of texture on these measurements, unlock-coupled scans were performed with different start angles for theta from 6.5° to 46.5° with interval of 10°, giving rise to the offset angle Psi between -24.5° and 25°. The information depth calculated by the software developed by Bruker, as a reference, is in a range of 1.1–5.5  $\mu\text{m}$ . The XRD patterns were obtained by the summation of the intensities of these 5 scans. The volume fraction of  $\alpha'$ -martensite was calculated using the standard ASTM E975, and the standard error was also obtained based on 5 scans for each condition. The micro-hardnesses of all the samples were measured using a Struers DuraScan micro-hardness tester. The hardness measurement was done on the RD-ND plane with a load of 300 g and at least 20 indentations for each sample.

### 3.3 Results

#### 3.3.1 Microstructure

In the 10% cold rolled sample, only few deformation induced low angle boundaries can be observed by EBSD (Figure 3-1(a)). Thick annealing twins with straight twin boundaries are observed by EBSD as marked by the red lines in Figure 3-1(a), while no deformation twins are observed in the EBSD images. Detailed TEM observations show a Taylor lattice (TL) dislocation structure with dislocations rather uniformly organized on the {111} slip planes as marked by the dashed lines in Figure 3-2(a). In addition, long straight domain boundaries (DBs) are observed and one example can be seen in Figure 3-2 (a) as marked by a dashed line, roughly parallel to a {111} slip plane. Domain boundaries contain a high density of dislocations and they are typically diffuse at this low strain. Stacking faults are also observed as shown in Figure 3-2 (a).

Both the density of deformation twins and the in-grain misorientation angles increase with increasing strain (see Figure 3-1 (b)). Deformation twins cover an area fraction of around 3% in the 30% deformed sample. As shown in Figure 3-1 (c-h), deformation twinning tends to occur in grains having a near Copper orientation and forms the twin Copper orientation {552}  $\langle 115 \rangle$ , while no deformation twins are

observed in grains with Brass orientation in the EBSD maps. The deformation twinning shown in Figure 3-1 (b) is quantified and the grains with a twinning fraction larger than 10% are denoted as matrix grains with most twins (MTG), while grains with no deformation twins (according to the EBSD result, i.e. Figure 3-1 (b)) are denoted as NTG. Also, microbands with thicknesses of 50-150 nm are observed by TEM (see Figure 3-2 (b)). In contrast to domain boundaries consisting of single dislocation walls, a microband is seen as a platelike region bounded by two parallel dislocation walls approximately along a  $\{111\}$  slip plane. Microbands form by a different combination of slip systems or different partitioning of the same slip systems on either side, and thus the orientations on the two sides of a microband are different (see the different contrast in Figure 3-2 (b)).

After 50% rolling reduction, the density of deformation twins is observed to increase considerably, forming a dense twin-matrix (T-M) lamellar structure, covering 43% of the area (see Figure 3-2 (c)). A high density of dislocations both in the matrix and the twins are observed. Shear bands are also visible in the 50% deformed sample, covering around 20% of the microstructure. After 80% rolling reduction, the T-M lamellar structure is frequently cut by shear bands, leaving some residual T-M lamellar structures seen as “diamond shaped” twin bundle areas (see Figure 3-2 (d)). These areas have an average diagonal length of around 5  $\mu\text{m}$  and align nearly parallel to the RD with a deviation angle of 0-20°, covering an area fraction of around 30%. As illustrated by the inset of Figure 3-2 (d), there is a large orientation variation within each shear band.

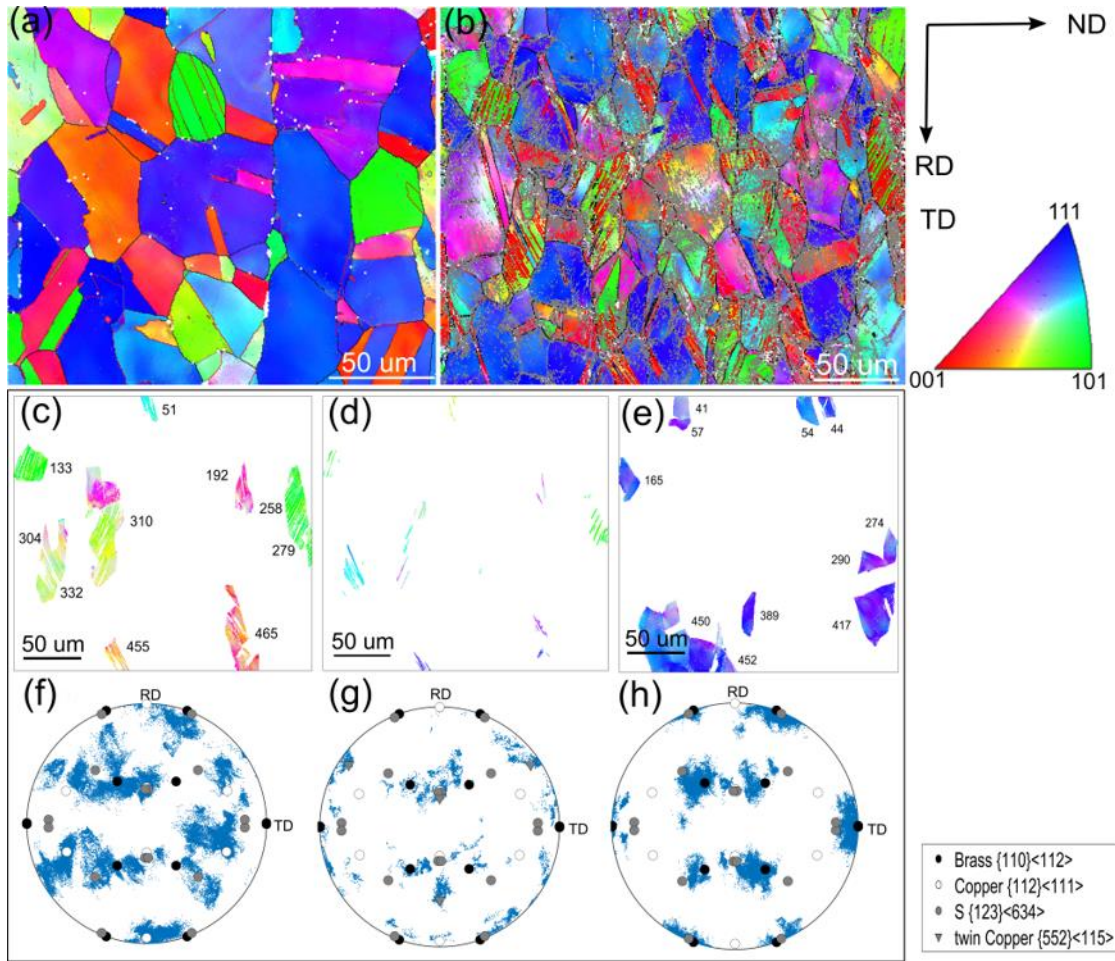


Figure 3-1 Orientation maps (inverse pole figure colouring of TD) obtained by EBSD showing microstructures in the longitudinal section of cold rolled 316L samples. (a) 10% deformed ( $\epsilon_{vm} = 0.12$ ), with an average distance between high angle boundaries of  $17 \mu\text{m}$  as determined by the line interception method (including annealing twin boundaries). (b) 30% deformed ( $\epsilon_{vm} = 0.41$ ). The red thick lines mark  $60^\circ/\langle 111 \rangle$  twin boundaries ( $\Sigma 3$  boundaries); grey lines inside the grains mark misorientation angles between  $2^\circ$  and  $15^\circ$ . (c), (d), and (e) Grains with most twins (MTG), the deformation twins, and grains without deformation twins (NTG), respectively, extracted from (b). (f), (g), and (h)  $\{111\}$  pole figures corresponding to (c), (d), and (e), respectively, showing near Copper, twin Copper  $\{552\} \langle 115 \rangle$ , and Brass orientations.

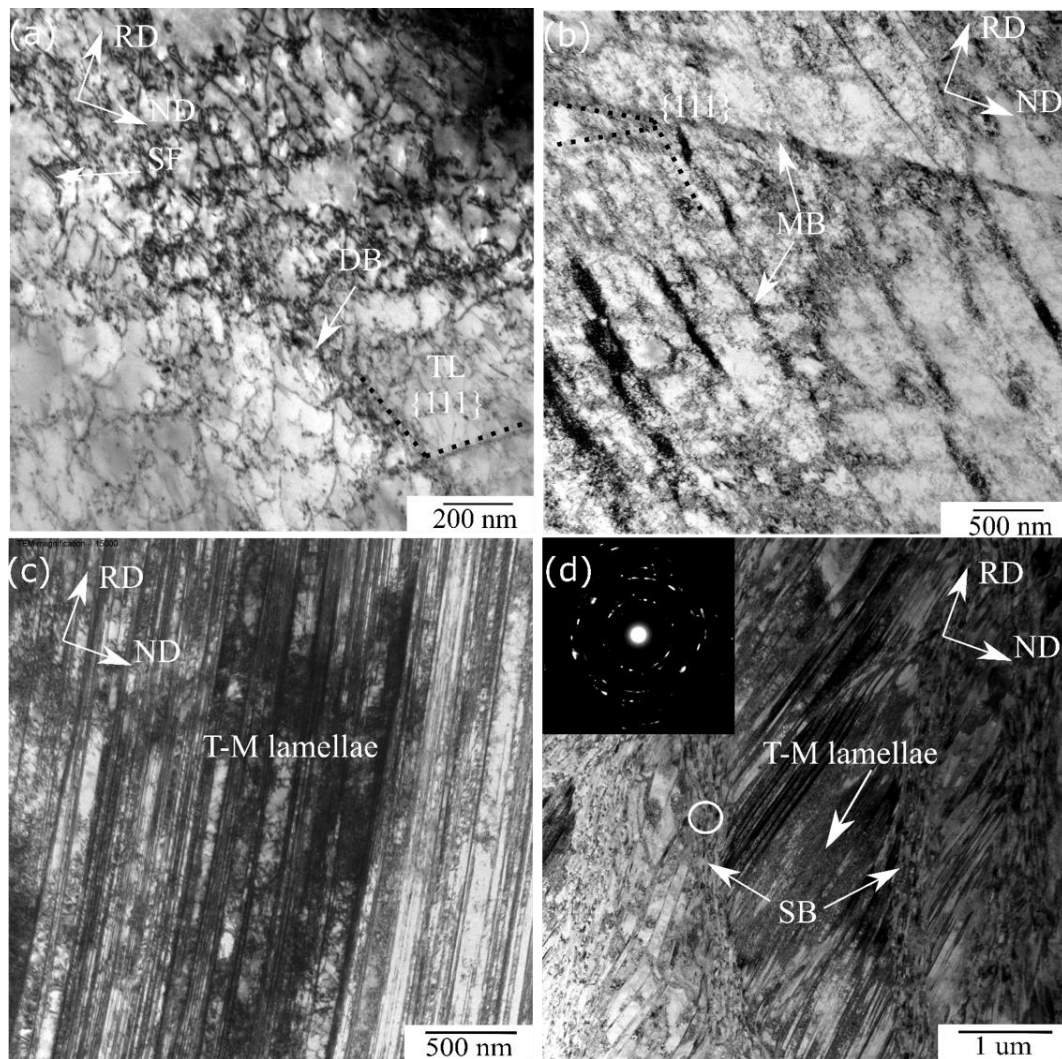


Figure 3-2 Microstructures in the longitudinal section of the cold rolled samples at different strains. (a) 10% deformed, showing the Taylor lattice (TL) dislocation structure with rather uniformly distributed dislocations and rather diffuse domain boundaries (DBs); a stacking fault (SF) is marked. (b) 30% deformed, showing microbands (MBs) and domain boundaries (DBs) subdividing the Taylor lattice (TL) dislocation structure. (c) 50% deformed, showing a twin-matrix (T-M) lamellar structure. (d) 80% deformed, showing shear bands (SBs) and residual twin-matrix (T-M) lamellar structure, seen as “diamond shaped” areas with twin bundles; the inset is the diffraction pattern taken from the area marked by the white circle.

In samples deformed to 30%–80%, interaction between microbands and deformation twins is frequently observed. The thick microbands shown in Figure 3-3(a) are sheared by subsequent deformation twinning into multiple sections and the local shear offset is related to the magnitude of twinning shear, whereas the total shear depends on both the magnitude of twinning shear and the twinning fraction in this region. In contrast, Figure 3-3 (b) shows T-M lamellae which are slightly sheared by

microbands, forming a parallelogrammatic morphology. In some grains, for example the one shown in Figure 3-3 (b), the microbands are curved in the region close to the grain boundary and the dislocation density in this region is much higher than that in the grain interior, indicating concentrated slip activities after formation of the microbands near the grain boundary.

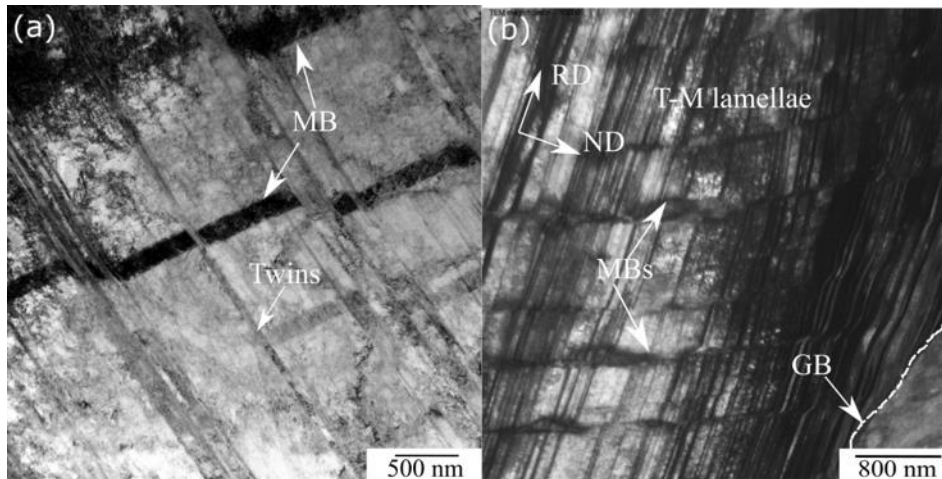


Figure 3-3 Interaction between microbands (MBs) and deformation twins observed in the longitudinal section. (a) 30% deformed, showing microbands (MBs) sheared by deformation twinning; (b) 50% deformed, showing T-M lamellae sheared by microbands (MBs). The microbands in the region near the grain boundary (GB) are curved.

Figure 3-4 shows selected details of the microstructures. At 10% rolling reduction, the twins are rather thin ( $\leq 50$  nm), see Figure 3-4 (a), less than the EBSD step size, making them “invisible” by EBSD characterization with the selected step size. Some stacking faults are observed to form in the matrix bounded by two Shockley partials, while others are observed with one side bounding to a twin boundary (examples are marked by the black arrows in Figure 3-4 (a)). An example of a shear band cutting the T-M lamellae in a direction around  $30^\circ$  away from the RD is shown in Figure 3-4 (b). Moreover, a second set of twins each with a twin thickness of a few nanometers can be also seen in the T-M lamellae in this example. Figure 3-4 (c) shows in more detail the microstructure within a shear band, which exhibits an elongated nano-grained structure aligned roughly parallel to the RD—similar to the deformation microstructure found in metals of higher SFEs at large strains, e.g. in Ni. [139]

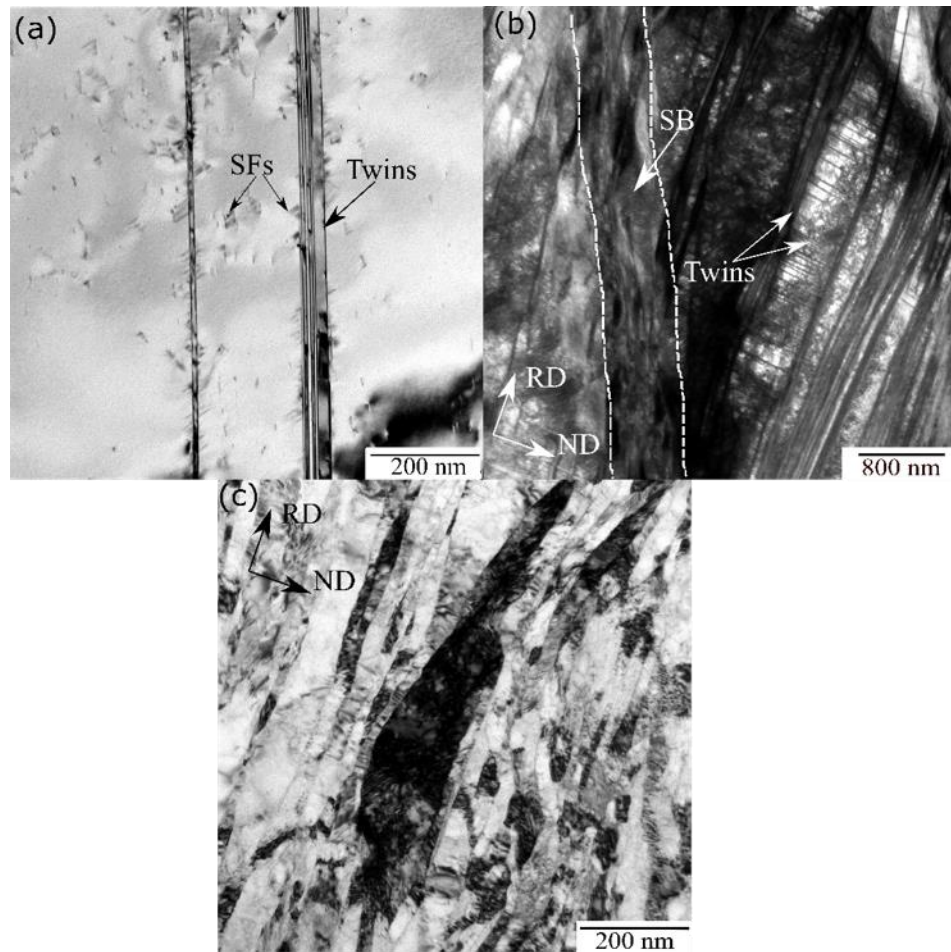


Figure 3-4 Bright field images showing typical details of the microstructures of the cold rolled samples (longitudinal sample section). (a) 10% deformed, showing thin deformation twins and stacking faults (SFs). (b) 50% deformed, showing the twin-matrix (T-M) lamellar structure aligned almost parallel to the RD, a second set of twins within the T-M lamellae, and a shear band (SB) cutting the T-M lamellae in a direction about 30° to the RD. (c) 80% deformed, showing the elongated nano-grained structure inside a shear band (SB).

#### A. *Martensite transformation*

The martensite transformation occurs at medium to high strains and an example observed in the 80% cold rolled sample is shown in Figure 3-5(a). The orientation relationship between the austenitic matrix and the  $\alpha'$ -martensite matches the classic Kurdjumov-Sachs (K-S) relation [140]:  $\langle 111 \rangle_{\alpha} // \langle 110 \rangle_{\gamma}$  and  $\{110\}_{\alpha} // \{111\}_{\gamma}$  (see Figure 3-5 (b)). The  $\alpha'$ -martensite is also observed in the XRD patterns (see Figure 3-6). The volume fraction of martensite is found to increase with deformation strain, reaching 18% after 80% rolling reduction. The results are summarized in Table 3-1. As the table shows, the uncertainties are large relative to the detected volume fractions

for rolling reductions below 80%, indicating the almost undetectable low fractions of martensite in these samples as the detection limit of XRD is considered to be 1–5%.

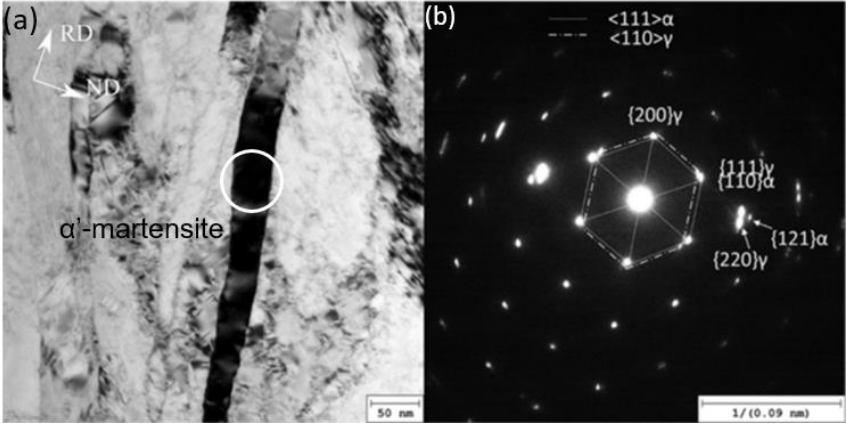


Figure 3-5 An example of  $\alpha'$ -martensite transformation observed in the 80% deformed sample. (a) Bright field image. (b) Diffraction pattern taken from the area inside the white circle in (a), showing the classic Kurdjumov-Sachs (K-S) relationship.

Table 3-1 Summary of microstructure quantification based on EBSD, TEM and XRD investigation.

sample	Taylor lattice fraction (%)	T-M lamella fraction (%)	Shear band fraction (%)	/	Martensite fraction by XRD (%)
10% (EBSD)	100	0	0	/	0
30% (EBSD)	77	23	0	/	0.6±0.2
50% (EBSD)	37	43	20	/	3.5±0.6
80% (TEM)	28	32	40	/	18.6±3

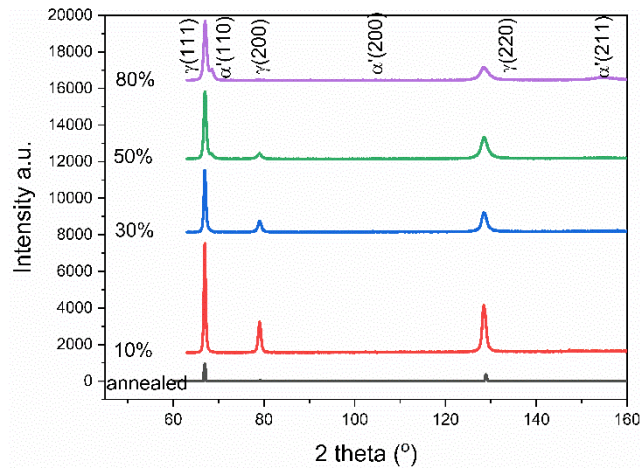


Figure 3-6 X-ray diffraction patterns for the initial (annealed) and cold rolled samples.

### B. Texture

ODFs of the cold rolled samples calculated based on the X-ray diffraction measurement are shown in Figure 3-7. At 10% thickness reduction, the sample has a very weak texture (see Figure 3-7 (a) and Figure 3-8(a)); the maximum intensity is only 1.8. The 30% rolled sample exhibits a stronger Brass component and also the Copper component has a higher intensity as compared to the 10% deformed sample. After 50% rolling reduction, the maximum intensity is at the exact Brass orientation as shown in Figure 3-7 (c) and Figure 3-8 (c)), and the Copper component is largely unchanged. At 80% thickness reduction, the Copper component has disappeared and the  $\{554\} \langle 225 \rangle$  orientation with a spread along the  $\{111\}$  fibre is observed. The  $\{111\}$  fibre is suggested to have developed by the rotation of  $\{111\}$  planes to the rolling plane under the compression stress [53].

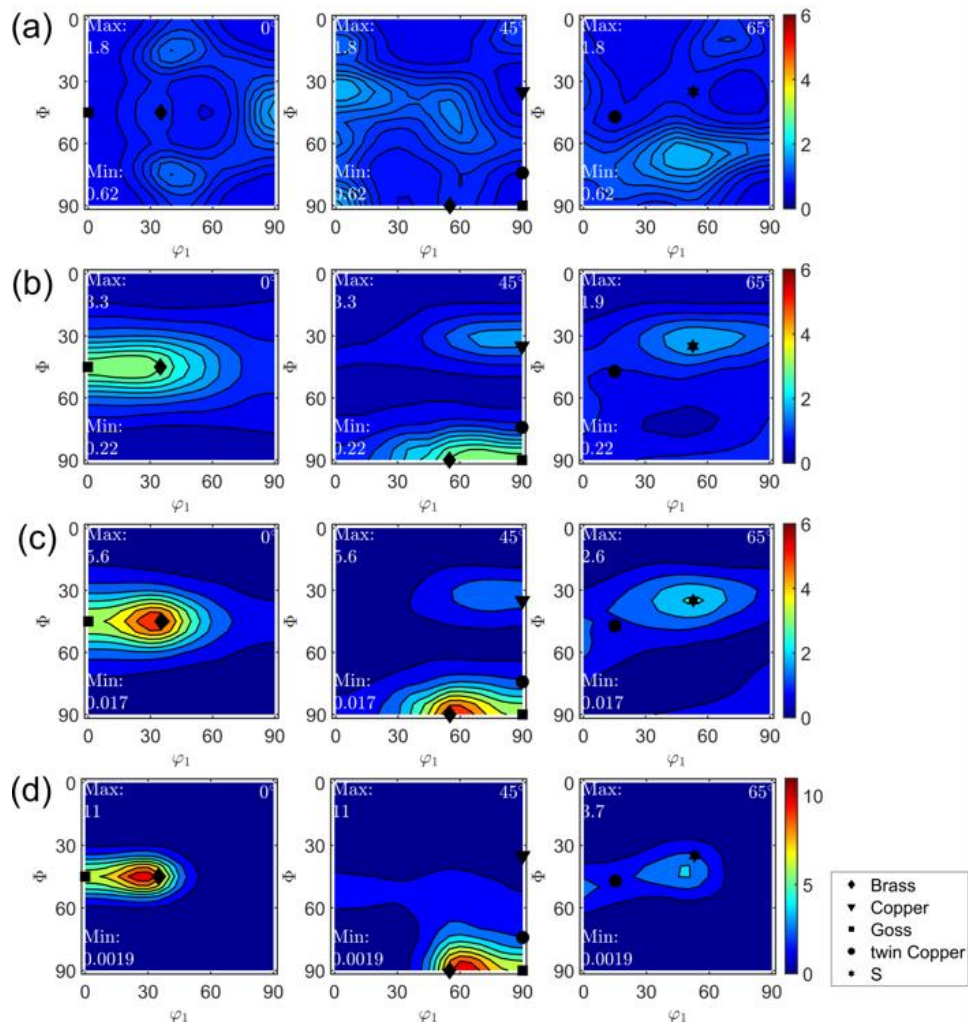


Figure 3-7 ODF sections ( $\phi_2$  at  $0^\circ$ ,  $45^\circ$ , and  $65^\circ$ ) showing the macro-textures of the cold rolled samples. (a), (b), (c), and (d) correspond to 10%, 30%, 50%, and 80% rolling reductions, respectively.

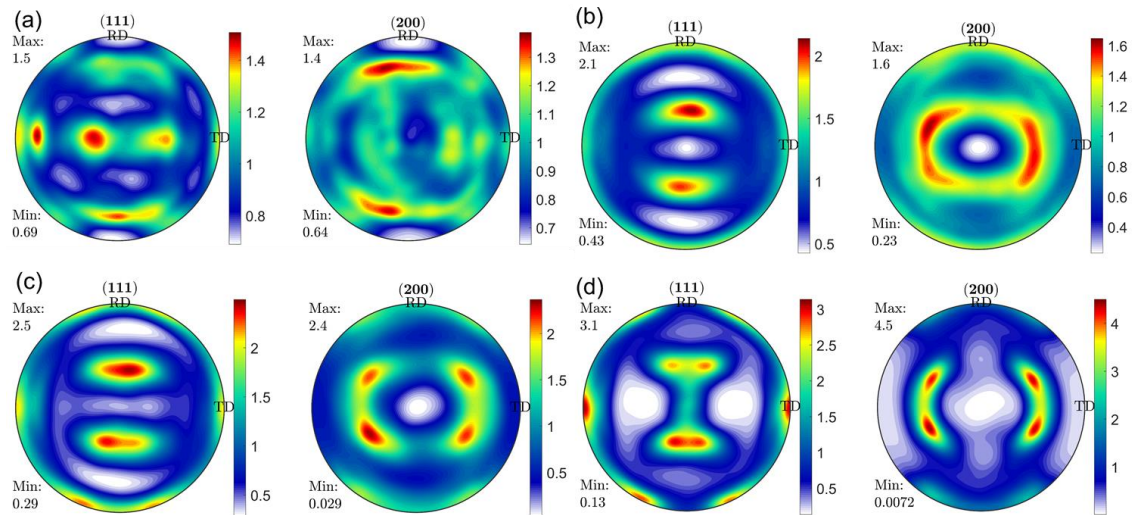


Figure 3-8 {111} and {200} pole figures (calculated from the ODFs) of the cold rolled samples. (a), (b), (c), and (d) correspond to 10%, 30%, 50%, and 80% rolling reductions, respectively.

### C. Micro-hardness

Figure 3-9 shows the hardness increases as a function of strain. This hardness curve gives an indication of the work hardening rate at different strains—it is high at low strains and decreases gradually with increasing strain. Higher fidelity mechanical tests, e.g. tensile tests, will be required to confirm the effect of cold reduction on the work hardening rate. After 80% thickness reduction, the hardness is 434 Hv, nearly 3 times that of the initial annealed sample.

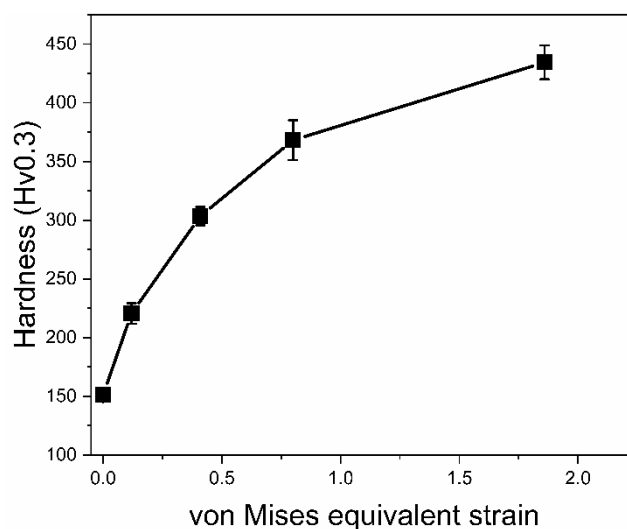


Figure 3-9 Micro-hardness as a function of the von Mises equivalent strain.

### 3.3.2 Discussion

#### *A. Correlation between Microstructure and Texture*

To clarify the microstructural evolution, idealised sketches of microstructures at different strains are shown in Figure 3-10. At low strain (see Figure 3-10(a)), dislocation slip is the dominant deformation mechanism and twinning is not very frequent because the critical resolved shear stress (CRSS) for slip is lower than that for twinning in 316L [141,142]. However, already at 10% rolling reduction, the equivalent flow stress (which may be estimated to be around 3 times the hardness [143] ( $3 \times 220 \text{ Hv}$ )) is comparable to the reported critical stress for twinning [142], rationalizing the deformation twins observed in the 10% cold rolled sample. The Taylor lattice dislocation structure with the dislocations aligned along  $\{111\}$  slip planes are similar to those reported by Kuhlmann-Wilsdorf [68] and Hughes [144]. This microstructure is typical in alloys of low SFEs and is formed due to the planar glide of dislocations. This microstructure contrasts the dislocation cell-block structure formed in materials of high SFEs like Al [45], where dislocations have a high three-dimensional mobility and can cross slip easily [68]. Domain boundaries and microbands are also observed at low strain, subdividing the Taylor lattice dislocation structure. Both domain boundaries and microbands are geometrically necessary boundaries, which are formed to accommodate the orientation difference between neighbouring domains [68], since the number of activated slip systems in each domain may be less than five, which is required by the Taylor model for homologous deformation [145].

At medium strain, the dislocation density becomes higher, the dislocation boundary spacing becomes finer, and the twin fraction becomes higher compared to low strain, as shown in Figure 3-10(b). Consequently, the interaction of these boundaries becomes more frequent as exemplified in Figure 3-3, and the T-M lamellae become a key part of the microstructure.

At high strain, the twinning planes of the T-M lamellae are rotated close to the rolling plane. The deformation becomes less uniform with localized concentrated slip, forming shear bands inclined about  $30^\circ$  to the RD, cutting the original Taylor lattice and T-M lamellar structures. These shear bands carry most of the plastic strain and also facilitate the nucleation of martensite. It should be noted that shear bands differ significantly from microbands in scale, alignment and local strain.

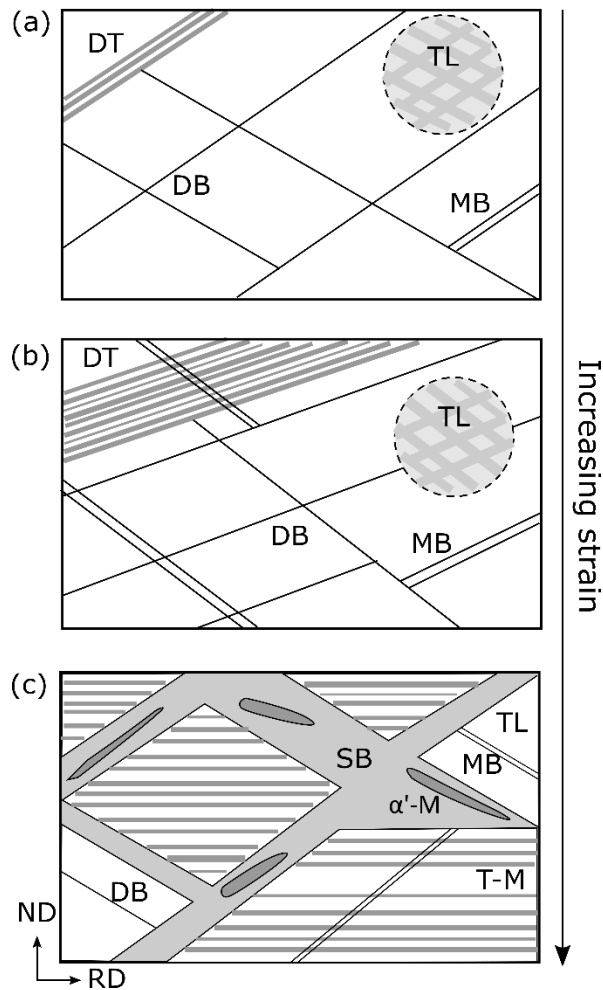


Figure 3-10 Idealized sketches illustrating the microstructural evolution as a function of strain. (a) At low strain, the Taylor lattice (TL) structure is subdivided by domain boundaries (DBs), microbands (MBs) and a few thin deformation twins (DT), all of which are aligned roughly parallel to the  $\{111\}$  planes; (b) at medium strain, with a higher dislocation density, more microbands (MBs) and deformation twins (DT) are formed and interact with each other, further refining the microstructure; (c) at large strain, shear bands (SBs) and martensite ( $\alpha'$ -M) are formed, and the twinning planes of retained twin-matrix (T-M) lamellae are rotated to be parallel to the rolling plane.

The texture evolution is found to be closely correlated to the microstructural evolution. To demonstrate this correlation, the volume fractions of selected texture components are calculated within a tolerance angle of  $15^\circ$  (without taking component overlap into account). The result is shown in Figure 3-11. The increasing volume fraction of Brass and Copper components with increasing rolling reduction (from 10% to 30% reduction) is mainly attributed to dislocation slip, in agreement with previous experiment and simulation in high Mn TWIP steels [134] and in materials with medium to high SFEs [53]. At higher strains, the Copper component is observed to be

partially transformed to the twin Copper orientation due to the significant deformation twinning observed in grains with this orientation (see Figure 3-1). Consequently, the volume fraction of the Copper component remains nearly constant with the rolling reduction (from 30% to 50% reduction) as shown in Figure 3-11, due to the balance between generation of Copper component by dislocation slip and consumption by deformation twinning.

It is found that the Copper type texture (i.e. the  $\beta$ -fibre including Copper, S, and Brass orientations) transforms to Brass type texture (i.e. the  $\alpha$  fibre including Goss and Brass orientations) after 50% rolling reduction, as the fraction of Copper component decreases and the fraction of S component  $\{123\} \langle 634 \rangle$  remains constant while the Brass and twin Copper  $\{552\} \langle 115 \rangle$  component increases after 50% rolling reduction (see Figure 3-11). Such a texture transition has been extensively investigated and debated heavily with considerable disagreement. Wassermann reported that deformation twinning was responsible for this texture transition by transforming Copper orientation to twin Copper orientation as mentioned above [52]. However, Leffers [54] and Duggan [146] suggested that the texture transition cannot be explained by twinning alone because the volume fraction of deformation twins (2% in 37% cold rolled 85/15 brass and less than 25% in 76% cold rolled 70/30 brass) is insufficient to account for this texture transition. This is also the case in the present 316L, where the volume fraction of deformation twins is 3% in the 30% cold rolled sample (according to EBSD data) and less than 25% in the 50% cold rolled sample (according to TEM results, assuming twins covering 50% of T-M lamellae). On the other hand, the onset of this texture transition coincides with the onset of shear banding (40% rolling reduction in brass [55] and 316L [56] as reported in the literature and in the range 30–50% in the present study), but it is far beyond the onset of deformation twinning. Therefore, we dare suggesting that the texture transition from the Copper type to the Brass type in the present samples is likely attributed more to the concurrent shear banding.

Phase transformation may also affect texture evolution. In TRIP steels [147],  $\epsilon$ -martensite transformation preferentially occurs in Copper and S components and therefore the decrease of the volume fraction of these two components starts from 20% rolling reduction, much earlier than the texture transition in the present 316L. In the present case, the volume fraction of  $\alpha'$ -martensite increases dramatically after 50%

thickness reduction and as a hard phase in the soft austenite matrix, the  $\alpha'$ -martensite may affect the deformation behaviour of the surrounding austenite. In fact, it was previously reported that the  $\alpha'$ -martensite tends to slow down the texture transition [148].

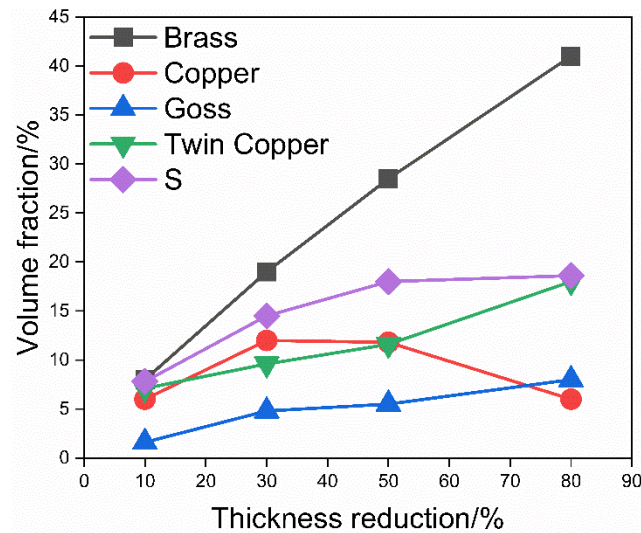


Figure 3-11 Volume fractions of texture components calculated within a tolerance angle of  $15^\circ$  (not taking overlap between the components into account) as a function of thickness reduction.

The mechanical properties are as expected also closely correlated to the microstructural evolution. The high work hardening rate at low strain is attributed to the following two factors: 1) cross slip is limited due to the low SFE and thereby mutual annihilation of dislocations of opposite Burgers vectors from different slip planes is suppressed; 2) deformation twinning significantly decreases the high angle boundary spacing, strengthening the material by acting as obstacles to dislocation slip according to the Hall-Petch relationship. Although the work hardening rate decreases after 30% rolling reduction partly due to the shear banding (a localized softening behaviour), the strength increases continuously. All the three deformation mechanisms, i.e. slip, twinning and strain-induced martensitic transformation, contribute to the increasing strength by increasing the density of dislocations, the area per unit volume of twin boundaries, and the volume fraction of martensite, respectively.

### B. Orientation Dependence of Twinning

Deformation twinning occurs preferentially in grains near Copper orientation while no twins are observed in grains near Brass orientation by EBSD in the 30% deformed sample (Figure 3-1). This is a commonly observed phenomenon in cold rolled fcc

metals [149] but not fully understood. To advance the understanding of the orientation dependence of deformation twinning, a detailed Schmid factor analysis is carried out here. The Schmid factor for rolling is defined [150] as  $(\cos \varphi_{RD} \cos \gamma_{RD} - \cos \varphi_{ND} \cos \gamma_{ND})/2$ , where  $\varphi_{RD}$  and  $\varphi_{ND}$  are the angles between the slip plane normal and RD and ND, respectively;  $\gamma_{RD}$  and  $\gamma_{ND}$  are the angles between the slip direction and RD and ND, respectively. This definition results in the Schmid factor below 0.5, similar to the traditional definition of the Schmid factor under unidirectional tensile stress.

When calculating the Schmid factors for the grains with many twins (MTG), it is found that the trace of twinning plane with the highest Schmid factor (as marked by the lines in Figure 3-12), agrees with the experimentally observed twinning plane trace in each grain, indicating that deformation twinning occurs preferentially on planes with higher twinning Schmid factors. Here the Schmid factors are calculated by averaging all pixel orientations for each grain in the 30% deformed condition. One may argue that this is not fully correct as the orientation of the matrix may change during deformation after twinning due to the slip in the matrix. However, given the good consistency between the twinning plane and the highest Schmid factor, this may be of little effect.

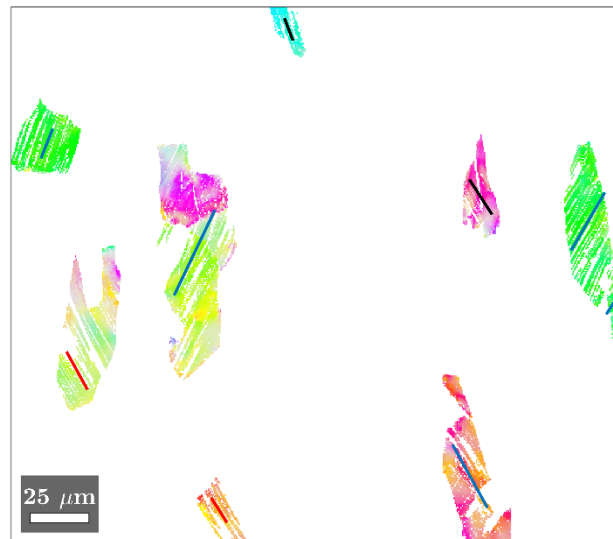


Figure 3-12 Grains with most twins (MTG) in the 30% deformed sample, where the traces of the twinning plane are marked in each grain for the twinning system of the highest Schmid factor. Dark blue line:  $(\bar{1}\bar{1}1)$ ; black line:  $(\bar{1}11)$ ; red line:  $(111)$ .

The calculation also shows that both the Schmid factors for twinning and slip (the shear direction is taken as  $\langle 112 \rangle$  for twinning and  $\langle 110 \rangle$  for slip) are higher for NTG

(near Brass orientation) than those for MTG (near Copper orientation). This finding is consistent with the result reported by Sinha et al. [151], who found that deformation twinning occurred in grains with low twinning Schmid factors during tensile deformation of 316L. However, this is contrary to the documented [152] twinning mechanism (although not fully proved experimentally) that deformation twinning requires a high resolved shear stress and thus a high twinning Schmid factor. To address this contradiction, some researchers [153] have employed the ratio of  $m_t/m_s$  as the criterion for deformation twinning, where  $m_t$  and  $m_s$  are the twinning and slip Schmid factors respectively, and claimed that a high ratio of  $m_t/m_s$  leads to a high tendency for deformation twinning. According to such a calculation, the average ratio for MTG (grains with near Copper orientation) is 1.05, while the average ratio for NTG (grains with near Brass orientation) is 0.98, suggesting that the twinning should be easier in MTG than in NTG. However, it may be not persuasive as the difference in this ratio is rather small whereas the difference in twinning frequency between MTG and NTG is rather dramatic.

In the analysis of accommodation of constrained deformation in fcc metal, Chin et al. modified the Taylor criterion by considering both slip and twinning, and thus the incremental work  $W$  performed by the applied stress  $\sigma_x$  is (resulting in an incremental strain  $\epsilon_{xx}$  in the x direction)

$$W = \sigma_x \epsilon_{xx} = \tau_s \sum_i s_i + \tau_t \sum_i t_i \quad (9)$$

where  $\tau_s$  and  $\tau_t$  are the critical resolved shear stress for slip and twinning, respectively;  $s_i$  and  $t_i$  are the amount of shear due to slip and twinning on the  $i$ th operative slip/twinning system, respectively. Following Taylor's least work hypothesis, to find the combination of operative slip and twinning systems, is equivalent to minimize

$$M = \frac{\sigma_x}{\tau_s} = \frac{1}{\epsilon_{xx}} (\sum_i s_i + \alpha \sum_i t_i) \quad (10)$$

with  $\alpha = \frac{\tau_t}{\tau_s}$  as the ratio of critical resolved shear stress for twinning versus slip. Based on their calculation, deformation twinning is activated in Copper orientation if  $\alpha$  is less than 1.15 and dislocation slip dominates in Brass orientation if  $\alpha$  is larger than 0.577. Following this modified Taylor criterion, it is suggested that  $\alpha$  in the present study is in the range of  $0.577 < \alpha < 1.15$ .

The modified Taylor criterion seems to be rather satisfactory. However, in reality the deformation twinning may be affected by many other factors, e.g. heterogeneous distribution of local stresses and dislocations. Also, the stable width of stacking faults under stress is found to be orientation dependent [154], and the stacking faults are considered to facilitate deformation twinning [155]. Such an effect may be considered in future studies to advance the understanding of strain accommodation by slip and twinning.

### 3.4 Conclusion

In this study, the microstructural evolution of 316L stainless steel cold rolled to reductions from 10% to 80% is characterized by both SEM and TEM. This evolution is interpreted in relation to the local crystallographic orientations, and thereby also the macro-texture evolution may be understood. The following conclusions may be derived:

- (1) Due to the low SFE of 316L, dislocation planar slip dominates initially, forming a Taylor lattice structure at low strain. The density of deformation twins increases with increasing strain, forming twin-matrix (T-M) lamellar structures. Shear banding and martensitic transformation within shear bands occur at high strain, subdividing the Taylor lattice and T-M lamellar structures.
- (2) Deformation twinning is found to occur preferentially in grains having the near Copper orientation rather than the Brass orientation, and on planes with the highest twinning Schmid factors. According to the modified Taylor criterion, extensive twinning in the near Copper orientation suggests  $\alpha > 0.577$  ( $\alpha$  is ratio of critical resolved shear stress for twinning versus slip), while the absence of twinning in the Brass orientation suggests  $\alpha < 1.15$ .
- (3) A texture transition from the Copper type to the Brass type is observed after 50% rolling reduction. This transition is observed to coincide with the onset of shear banding, suggesting an important role of shear banding—in addition to deformation twinning—in this texture transition.
- (4) The observed work hardening rate is high, especially at low strain. This high work hardening rate is related to the low SFE, which limits mutual annihilation of dislocations by suppressing cross slip and reduces the high angle boundary spacing by promoting twinning. At high strain, the martensitic transformation

also contributes to the work hardening, counterbalancing the possible softening effect from shear banding.

### **Acknowledgement**

The authors gratefully acknowledge support from the European Research Council (ERC) under the European Union's Horizon 2020 research and innovation programme (grant agreement No.788567) for the M4D Advanced Grant within which this work is performed. CZ further acknowledges the financial support of the China Scholarship Council (CSC) (N0. 201706120026). The authors also thank Flemming Bjerg Grumsen for his kind help on the XRD measurements.



# Chapter 4: Deformation behaviour of 3D printed 316L

---

This chapter presents the microstructural evolution of 3D printed 316L during deformation. Based on the knowledge of microstructural evolution of conventional manufactured 316L shown in Chapter 3, the effect of the printed microstructure on the deformation behaviour is analysed and the results are reported and discussed in the following manuscript.

## **Effects of initial 3D printed microstructures on subsequent microstructural evolution in 316L stainless steel (Manuscript II)**

Chunlei Zhang\*, Dorte Juul Jensen, and Tianbo Yu\*

Department of Mechanical Engineering, Technical University of Denmark, Kgs. Lyngby DK-2800, Denmark

\*Corresponding author, Email: [chzhang@mek.dtu.dk](mailto:chzhang@mek.dtu.dk); [tiyu@mek.dtu.dk](mailto:tiyu@mek.dtu.dk)

Abstract:

Plastic deformation of 3D printed components may occur when they are in use. Here we analyse the effects of the initial 3D printed microstructure of 316L stainless steel on the subsequent deformation behaviour, where we apply 10% and 30% thickness reductions by cold rolling. The microstructures are characterized by scanning electron microscopy (SEM), including electron backscatter diffraction (EBSD), and transmission electron microscopy (TEM). It is suggested that the pre-existing dislocation structure in the 3D printed 316L significantly affects the microstructural evolution during cold rolling. Deformation twinning, facilitated by the pre-existing dislocations in 3D printed samples, occurs earlier and the twins are thinner compared to conventionally manufactured 316L. Double sets of deformation twins are commonly observed in 3D printed samples, which is not the case for conventionally manufactured samples, and is related to the complex local stress state again stemming

from pre-existing dislocations of various Burger vectors. Strong interaction between dislocations and twin boundaries is observed, and the pre-existing dislocation structure significantly increases the strength of the material.

#### **4.1 Introduction**

3D printing, a popular additive manufacturing (AM) process, has drawn enormous attention during the last few decades because it enables near net-shape manufacturing of components with complex shapes [1–3]. L-PBF is in particular popular. It is based on a powder bed fusion technology, and builds parts using a laser selectively melting metallic powder in a layer-by-layer mode. This technology has been used to manufacture components of many alloys, e.g. Ti-6Al-4V, TiAl-based alloys, IN718, Al-Si-10Mg, and stainless steels [156–158].

Austenitic stainless steel 316L (SS316L) is one of the most frequently used stainless steels, due to its good corrosion resistance and formability. Many of the SS316L components have complex geometries, for example pipeline systems used in the nuclear industry [9], various tailor-made implants [10,11], and structural components used in the automotive and aerospace industries [12], making conventional manufacturing processes difficult and costly. Thus, there is huge potential in producing 316L components via AM techniques and a need for understanding the relationship between AM parameters, microstructure, and mechanical properties.

Extensive recent research has shown that the printing parameters, for example the scan strategy, laser power, and scan speed, significantly affect the microstructure, voids distribution, and mechanical properties of the printed samples, e.g. [16,17,159]. With careful optimization of these printing parameters, almost fully dense printed samples with finely controlled microstructures are obtained [20,160]. Additionally, a promising result is that the L-PBF printed 316L samples may have even better mechanical properties (higher strength and comparable ductility) than the as cast and even wrought counterparts [161]. This improvement in mechanical properties is attributed to the fine-scale microstructures resulting from the printing process. It is well known that the microstructure of 3D printed parts is very different from that of conventionally manufactured parts due to the fast heating and cooling rates in the printing process. Wang et al. [20] reported a complex heterogeneous cellular microstructure in printed 316L samples and suggested this as an explanation for the

improved properties. A recent study [25] suggests that it is the local thermal expansion/shrinkage in a constrained medium that contribute to the origin of dislocations in the cellular structure, rather than other factors, e.g. dendritic micro-segregation and the resultant constitutional stress, and misorientations between dendrites. When the melt pool is cooling down, the crystallographic direction  $\langle 001 \rangle$  (in metals of cubic crystal system) is favored for growth along the maximum temperature gradient, which is normally perpendicular to the melt pool surface. Therefore the columnar boundaries are parallel to the building direction when a shallow melt pool is solidified whereas for the cases within deep melt pools, cellular structures may form during solidification [162]. Elemental segregation to the cellular dislocation boundaries of printed 316L is another feature that is reported in some studies [20,24]. Segregation could reduce the energy and mobility of dislocation boundaries and thus stabilize dislocation boundaries.

Irrespective of how the pre-existing cellular structure is formed, it is expected to affect the dislocation behaviour, and therefore plays a vital role, in any subsequent deformation behaviour. This is of importance as 3D printed components are exposed to external loads when they are in service. So far, this topic has not been thoroughly investigated. Liu et al. [24] suggested that the cellular structure in printed samples may significantly impede dislocation motion but not fully block it. However, there is a lack of experimental characterization underpinning the understanding of how the 3D printed microstructures evolve during subsequent deformation.

The aim of the present study is thus to investigate the microstructural evolution of L-PBF printed 316L when exposed to a subsequent external strain. We have here chosen cold rolling as the deformation mode because the microstructural evolution of fully recrystallized 316L during cold rolling is well known [163]. We realize that a printed component is not very likely to be rolled after printing, but this deformation process will clearly highlight the effects of the printing microstructures on the following deformation behaviour—for example the balance between deformation twinning and dislocation slip—and its effects on the evolution of mechanical properties.

## 4.2 Experimental

Stainless steel 316L samples, with sizes of 3 mm × 4 mm × 14 mm in the scanning directions X, Y and the building direction (BD), were produced by L-PBF. The laser power and scanning speed were set to 370 W and 1.35 m/s, respectively. A 67° rotation of the scanning direction between neighboring layers was applied, making the X and Y scanning directions equivalent. To improve the surface finish of the sample, a final contour scanning, with input power of 120 W and scanning speed of 0.22 m/s, was applied. As sketched in Figure 4-1, the 3D printed samples were unidirectionally rolled along BD at room temperature to thickness reductions of 10% and 30% (von Mises equivalent strains  $\varepsilon_{VM}$  of 0.12 and 0.41, respectively). During cold rolling, the samples were lubricated by mineral oil and turned upside down between each pass. The ratio of the contact length to the mean height  $l/h$  was kept between 2 and 5 to ensure maximal through-thickness strain homogeneity. For convenience, the as-printed sample, and the printed samples after 10% and 30% rolling reductions are denoted as P-0, P-10%, and P-30%, respectively.

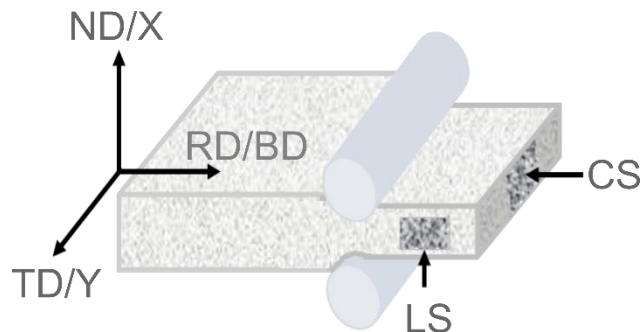


Figure 4-1 Sketch of the rolling geometry of the as-printed sample (P-0). The rolling direction (RD) is parallel to the building direction (BD); the normal direction (ND) is parallel to the X direction; the transverse direction (TD) is parallel to the Y direction. The small micrographs in the longitudinal section (LS) and the cross section (CS) indicate the sections used for microstructural characterization.

A Zeiss Supra 35 field emission gun scanning electron microscope (FEG-SEM), equipped with an HKL electron backscatter diffraction (EBSD) system, was used to characterize the microstructure. EBSD samples were prepared by grinding using SiC papers followed by mechanical polishing. A colloidal silica suspension (0.04  $\mu\text{m}$ ) was used for the final polishing step. Transmission electron microscopy (TEM) investigations were performed using a JEOL JEM-2100 microscope at an acceleration voltage of 200 kV. Foils for the TEM investigations were prepared by a modified

window technique in a perchloric acid based electrolyte [120]. EBSD and TEM characterizations were carried out at the thickness centre for both the cross section and the longitudinal section (see Figure 4-1). EBSD maps were obtained using a step size of 500 nm. Simple noise reduction, e.g. removing wild spikes and filling them with neighbor orientations, was applied using Channel 5 software. MTEX was used for analyzing the EBSD data [119,164], e.g. the Schmid factor analysis. We define boundaries in EBSD maps according to their misorientation angles into low angle boundaries (LABs, 2–15°) and high angle boundaries (HABs, >15°). Twin boundaries (TBs) are defined as boundaries which deviate less than 2° from the misorientation angle/axis of 60°/⟨111⟩. The Vickers microhardness was measured using a Struers DuraScan hardness tester with a load of 300 g. For all samples, the hardness was measured in the longitudinal section, and each value was averaged over at least 12 measurements.

### 4.3 Results

#### 4.3.1 Microstructure of the as-printed sample (P-0)

For the P-0 sample, EBSD results from the longitudinal section reveal the melt pool shapes, as shown in Figure 4-2(a). Here domains delineated by HABs are denoted as grains for simplicity although they are different from grains in conventionally manufactured materials. The microstructure near the lateral surface of the sample grows perpendicular to the BD (but still in the direction of maximum temperature gradient) as marked by the vertical white arrows in Figure 4-2 (a). The average spacing of HABs measured by the line intercept method are 33 μm and 17 μm along the BD and X direction, respectively. There are some large grains, e.g. the blue region in the lower part of Figure 4-2 (a) marked by the white horizontal arrow, indicating local epitaxial growth along the BD during 3D printing. The misorientation angle profile along the horizontal white arrow in Figure 4-2 (a) is shown in Figure 4-2 (c), revealing the significant orientation spread inside this big grain. On the cross section (X/Y plane), the microstructure shows a checkerboard-like pattern due to the 67° rotation of the scanning direction between neighboring layers (Figure 4-2 (b)). The checkerboard-like structure shows similar HAB spacing along the X and Y directions, on average approximately 17 μm. As marked by the white arrow in the up-right corner of Figure 4-2 (b), there are dense parallel LABs inside the grain. By measuring the orientation

along the white arrow, a large orientation spread is found (see Figure 4-2 (d)). Due to the partial re-melting of each layer (except the top layer), the melt pools show a “U” shape in the longitudinal section (see Figure 4-2 (a)) and alternating strings of small and large grains in the cross section as shown in Figure 4-2 (b).

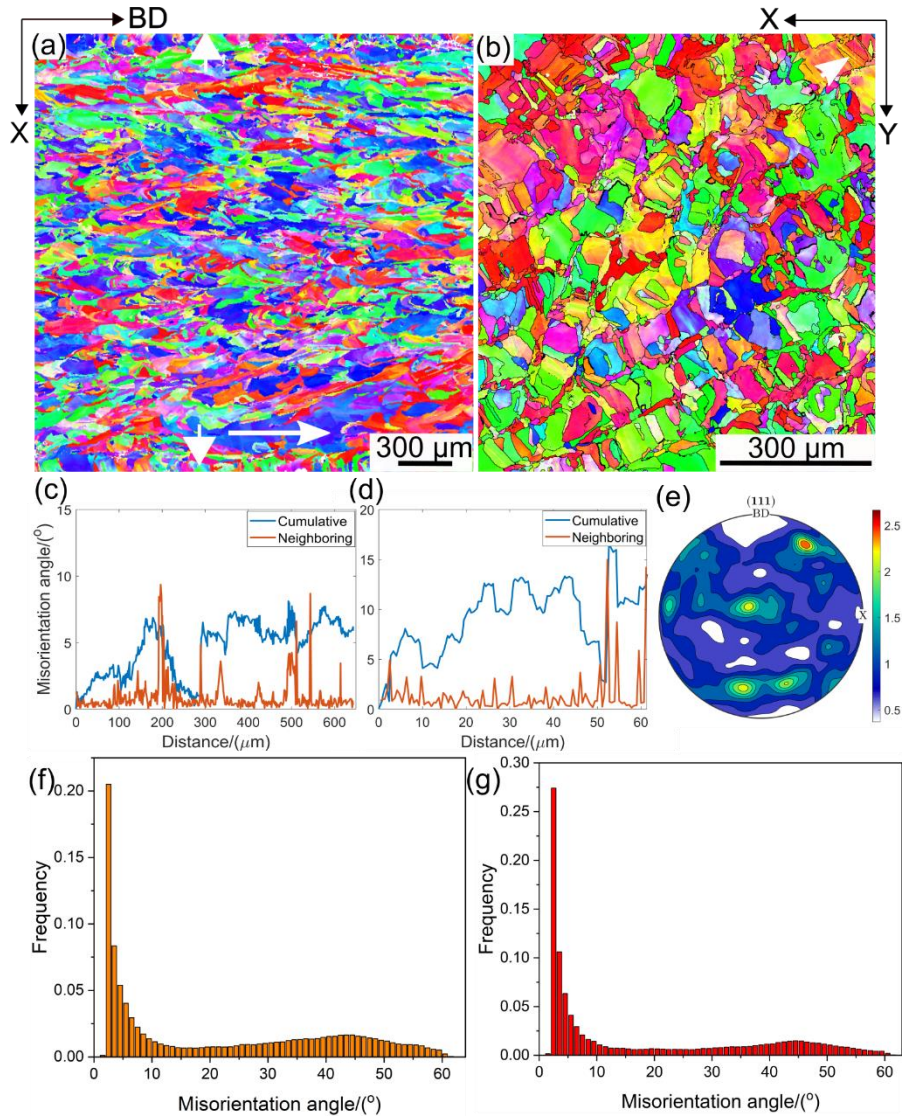


Figure 4-2 P-0; EBSD results. Orientation maps from the longitudinal section (a) and cross section (b). (c, d) Misorientation angle profiles along the horizontal white arrow in (a) and the up-right-corner white arrow in (b), respectively, showing large orientation spread in 3D printed grains. (e)  $\{111\}$  pole figure of (a), showing a weak texture of the present 3D printed 316L. (f, g) Misorientation angle distributions from the longitudinal section (a) and cross section (b), respectively.

The fraction of LABs is between 50%–60%, as shown in Figure 4-2 (f) and (g). Figure 4-2 (e) shows the texture, visualized as the  $\{111\}$  pole figure, of the region shown in Figure 4-2 (a) ( $2.4 \text{ mm} \times 2.4 \text{ mm}$ ). A weak texture is observed. This is

typical of printed samples manufactured with a rotation of the scanning direction between adjacent layers.

To investigate the fine scale dislocation microstructure, TEM was utilized and representative micrographs are shown in Figure 4-3. There are two types of dislocation structures: cellular structure and columnar structure. The dislocation boundaries in the cellular structures (CeDBs) are observed to be loose, with an average width of about 50 nm. The average spacing of CeDBs is about 500 nm (see Figure 4-3 (a)) and their misorientation angles are mostly less than  $1^\circ$ . The dislocation boundaries in the columnar structures (CoDBs) have similar spacings and misorientation angles to those of CeDBs. Stacking faults are visible in high magnification micrographs. Figure 4-3 (b) shows a set of parallel stacking faults inside a cellular structure and Figure 4-3 (c) shows a stacking fault (approximately 800 nm) reaching all the way to the two CeDBs. In our TEM samples, no elemental segregation is observed by energy dispersive X-ray spectroscopy.

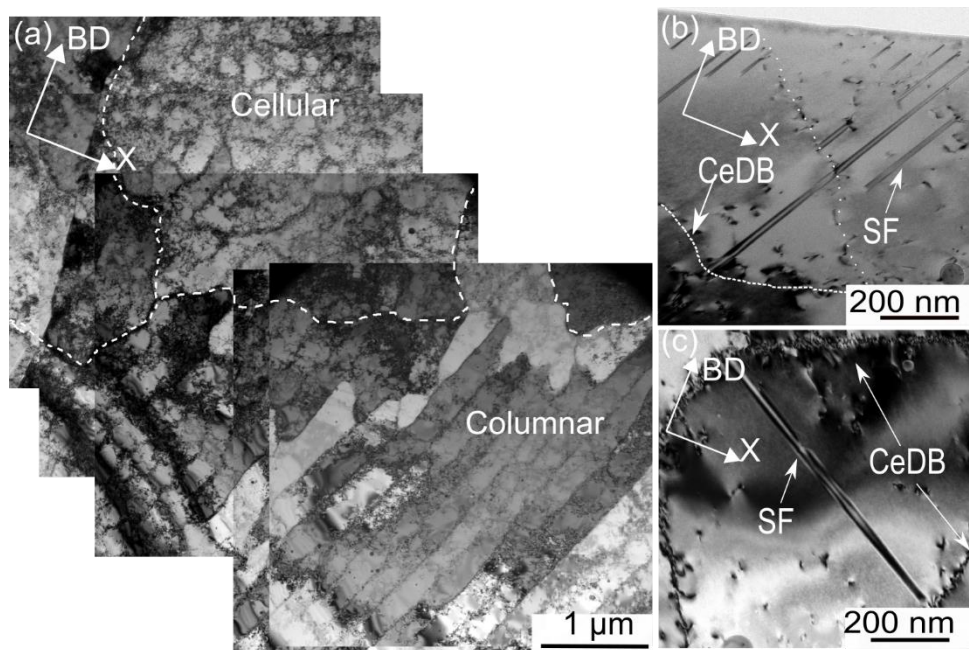


Figure 4-3 Bright field TEM images of the as-printed sample (P-0). (a) Low magnification micrograph showing both the cellular structure and columnar structure. The spacings of CeDBs and CoDBs are similar, on average 500 nm. (b, c) High magnification micrographs showing stacking faults (SFs) within the cellular structure.

### 4.3.2 Microstructure after 10% reduction (P-10%)

After 10% rolling reduction, deformation twins are observed in EBSD orientation maps as shown in Figure 4-4(a,b). There is no obvious change in the shape of grains due to deformation compared to P-0 (see Figure 4-2). 14% of the grains (area fraction) are observed to have deformation twins at this strain. Most of the grains hosting twins exhibit a single set of deformation twins, only two grains are observed exhibiting double sets of deformation twins (marked by the white arrows in Figure 4-4 (b)). The fraction of twin boundaries is 5%, while LABs amount to 67%, of the total boundary length (Figure 4-4 (c,d)).

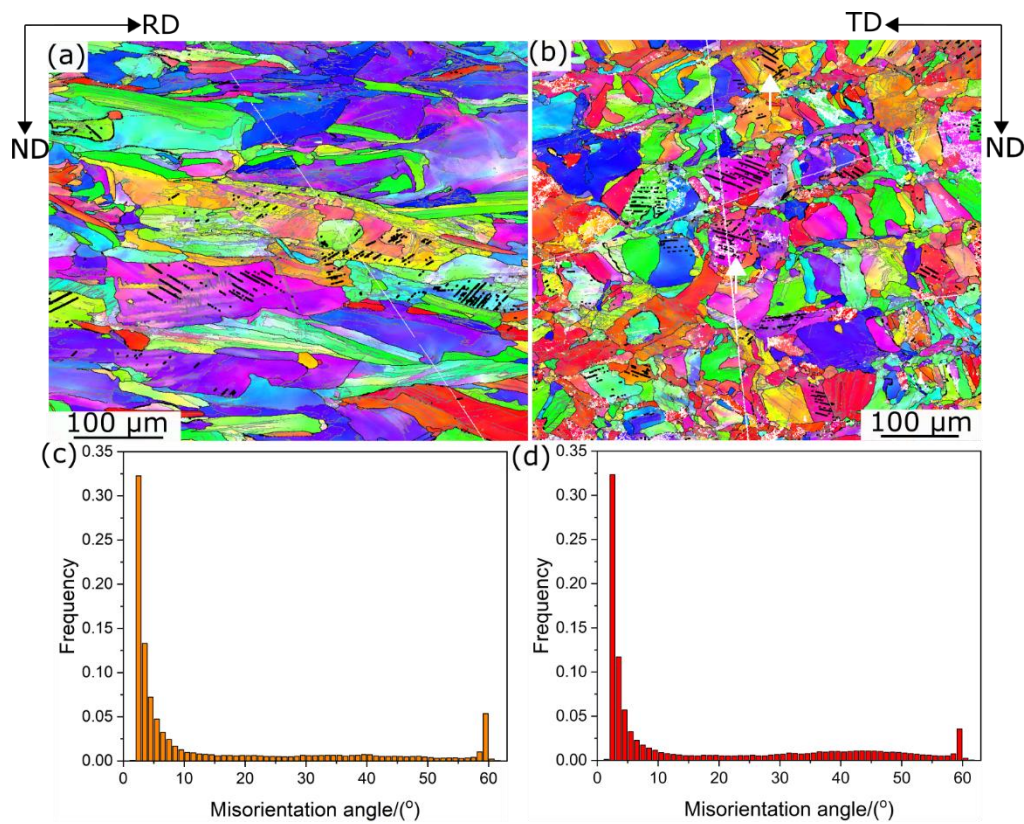


Figure 4-4 P-10%; EBSD results. Orientation maps from the longitudinal section (a) and cross section (b). The thick black lines mark twin boundaries; gray lines and thin black lines mark LABs and other HABs, respectively. Boundary misorientation angle distributions (c) and (d) from (a) and (b), respectively. Deformation twins are detected in some grains and the fraction of LABs is increased due to deformation.

A TEM image of the typical microstructure in P-10% with one set of deformation twins is shown in Figure 4-5(a). It is a common observation that deformation twins penetrate and shear the CoDBs. The observed local shear offset is related to the twin thickness and the angle between the CoDB normal and the twinning direction. In the

region delineated by CoDBs, the dislocation density increases due to plastic deformation.

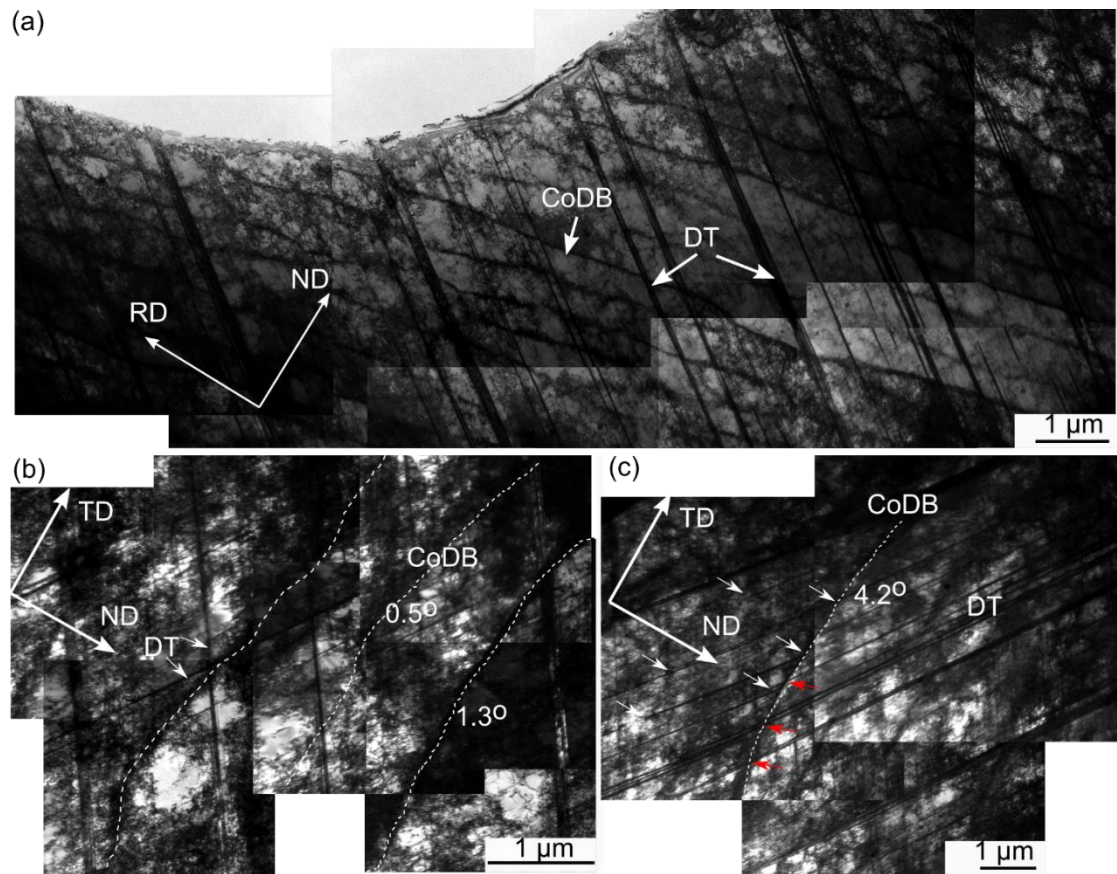


Figure 4-5 Montages of TEM images showing the deformation microstructure of P-10%. (a) Longitudinal section view, showing deformation twins (DTs) penetrating dislocation boundaries in the columnar structure (CoDBs); (b) cross section view, showing the interactions between double sets of deformation twins, dislocation boundaries, and loose dislocations; (c) cross section view, showing the interaction between deformation twins and CoDBs. The white arrows mark twins that are stopped by the CoDB while the red arrows mark twins penetrating the CoDB.

In a few grains where two sets of deformation twins are observed, the grains are subdivided into many parallelogrammatic regions (see Figure 4-5 (b)). A high density of dislocations are also observed in these parallelogrammatic regions, further subdividing the microstructure by forming new dislocation boundaries. For some CoDBs, e.g. the CoDB marked by the white dashed line in Figure 4-5 (c), some deformation twins are stopped by the boundaries (see white arrows in Figure 4-5 (c)) although others penetrate the boundaries (see red arrows in Figure 4-5 (c)), indicating that the CoDBs affect deformation twinning. Twins are also seen in the CeDBs

structure. A magnified image, exhibiting double sets of deformation twins formed on two  $\{111\}$  planes, is shown in Figure 4-6. The vertical set develops first and is thus sheared by the subsequent deformation twinning set. The latter is a twin bundle containing multiple thin deformation twins. High dislocations densities inside the twin bundle are observed.

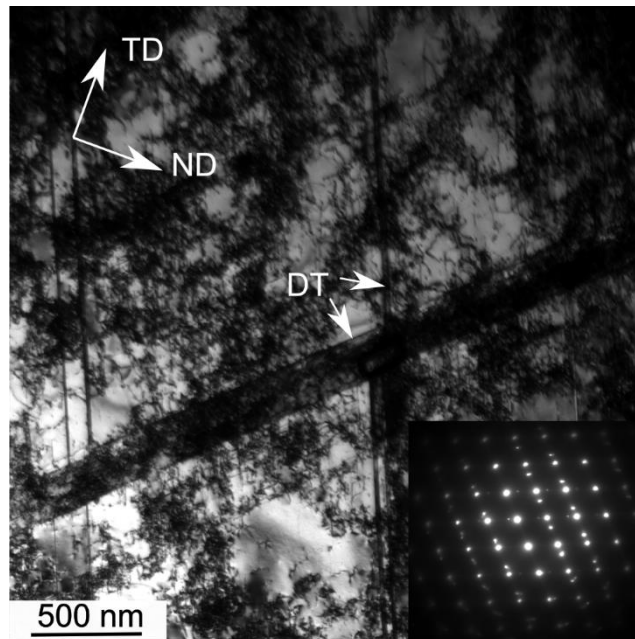


Figure 4-6 TEM bright field image in a CeDBs structure showing double sets of deformation twins (DTs) in P-10% (inset is the diffraction pattern taken from the intersection area of two sets of twins). One set of twins is sharp while the other set is twin bundles containing many thin twins.

Typical dislocation structures observed in the areas without deformation twins are shown in Figure 4-7. Some dislocations align on one of the  $\{111\}$  planes as marked by the white dashed lines in Figure 4-7 (b). However, a common observation is that rolling induced dislocations entangle and organize to form new dislocation boundaries between the original CeDBs/CoDBs.

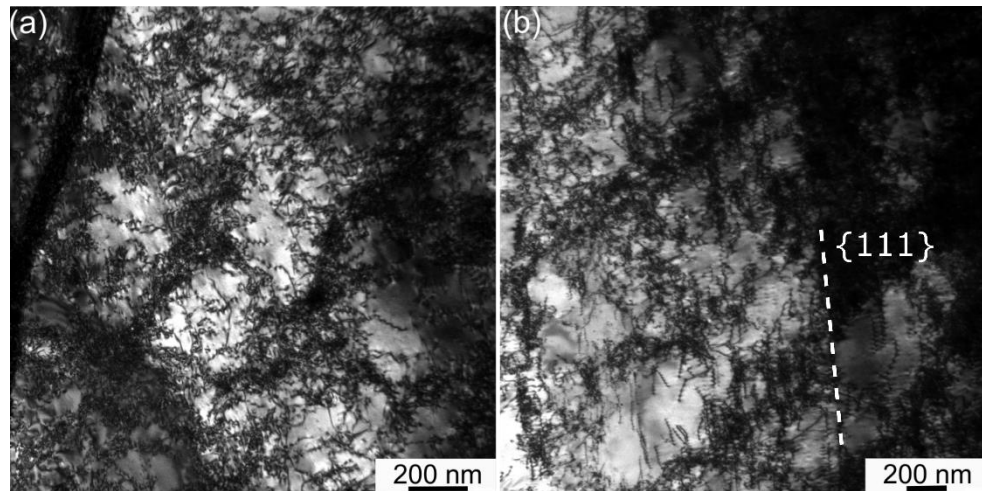


Figure 4-7 Bright field TEM graphs revealing typical microstructures in grains without deformation twins in P-10%. (a) Dislocation configuration in a cellular structure; (b) development of new dislocation boundaries in a columnar structure. The dashed line shows one of the  $\{111\}$  slip plane family.

#### 4.3.3 Microstructure after 30% reduction (P-30%)

After 30% rolling reduction, an elongated microstructural morphology is observed (compressed along ND) as shown in Figure 4-8. The aspect ratio, i.e. the spacing of HABs along RD or TD to that along ND, increases to 3 in the longitudinal section and to 1.5 in the cross section (Figure 4-8 (a, b)). More grains (31% in area fraction) are observed to deform by twinning, compared to P-10% (14%). The fraction of twin boundaries is about 15% of the total boundary length. Twin boundaries are at a tilt of  $\pm 45^\circ$  to RD in the longitudinal section (Figure 4-8 (a)) and parallel to TD in the cross section (Figure 4-8 (b)). These twin planes, approximately  $\pm 45^\circ$  rotated about TD from the rolling plane, have the largest shear stress. Although single sets of deformation twins are still the most common, double sets are frequent in some regions, as marked by the white arrows in Figure 4-8 (a).

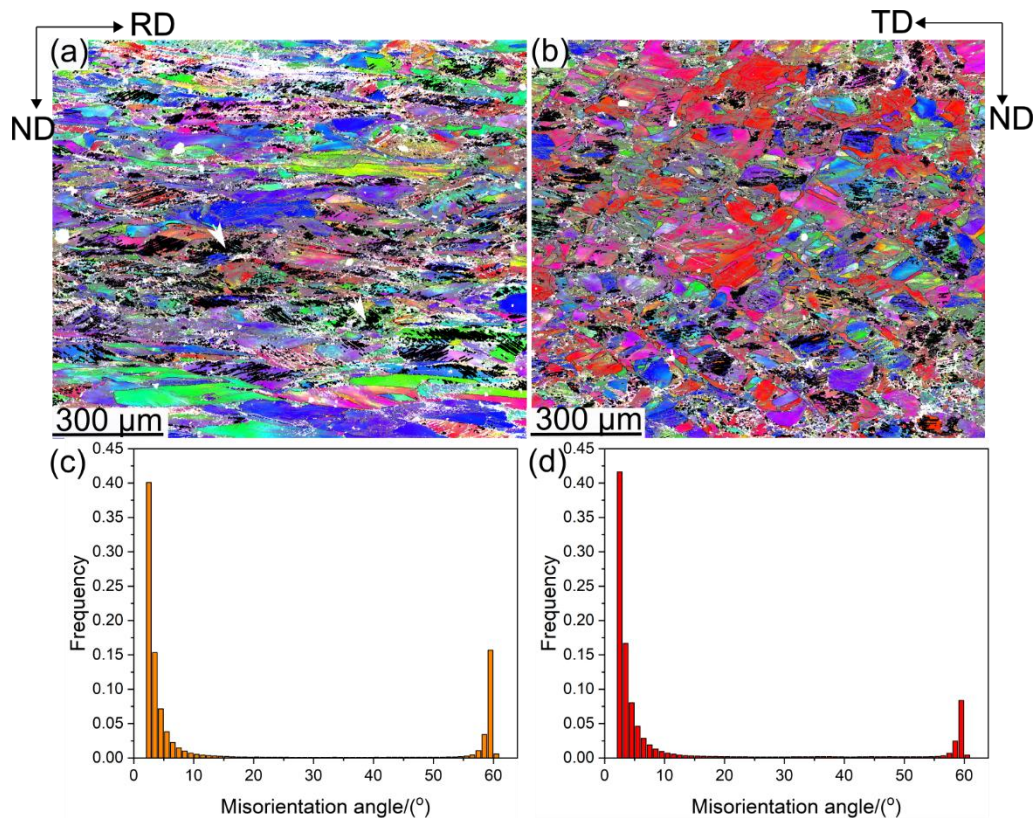


Figure 4-8 P-30%; EBSD results. Orientation maps from the longitudinal section (a) and cross section (b). Thick black lines mark twin boundaries; gray lines and thin black lines mark LABs and other HABs, respectively. The white arrows mark double sets of twins. Boundary misorientation angle distributions (c) and (d) from (a) and (b), respectively. The grains are elongated along RD. More deformation twins are detected compared to samples deformed to a lower strain.

An example of a TEM observation of a grain with double sets of deformation twins is shown in Figure 4-9(a). The first set of twins are denser compared to the second set having another twin variant, indicating that the first set of twins are favorable under the current stress state. Magnified images, (see Figure 4-9 (b) and (c)), show very thin deformation twins with thicknesses down to a few nanometers.

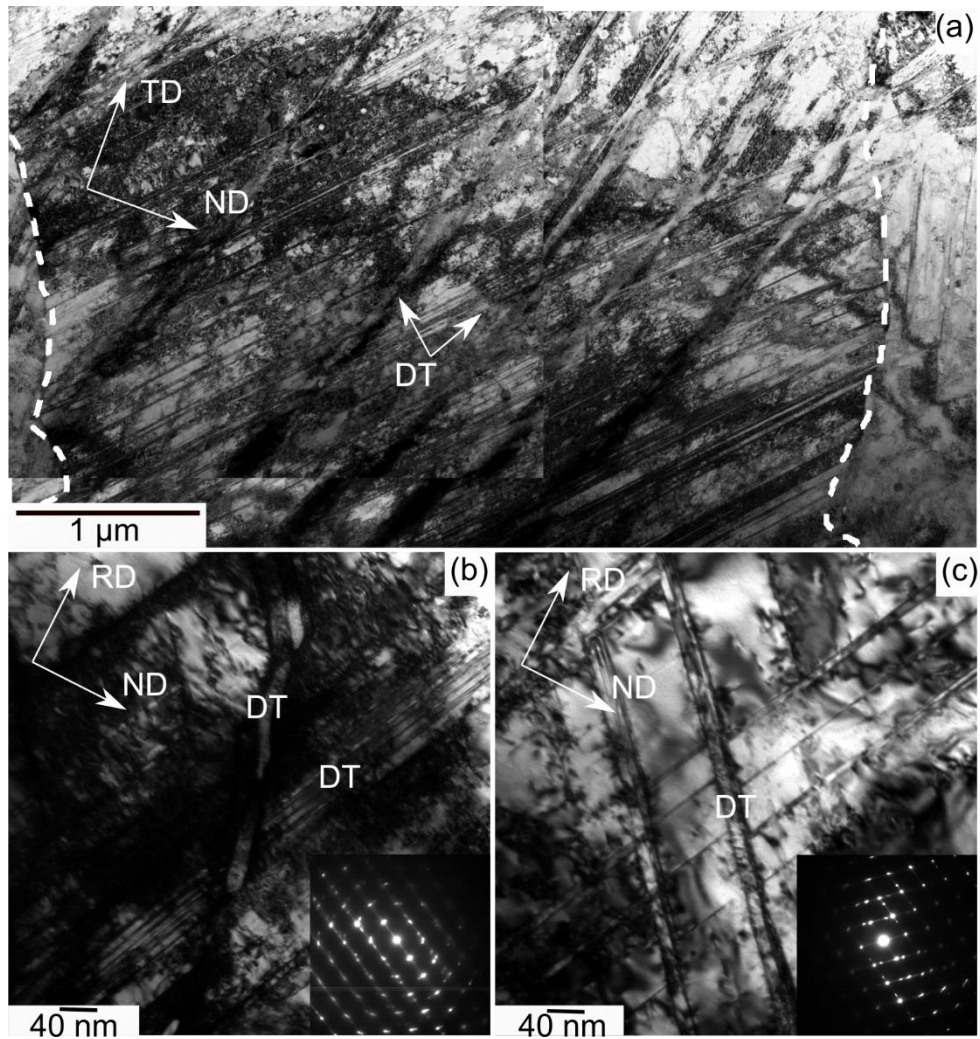


Figure 4-9 Bright field TEM images showing morphology of deformation twins in P-30%. Overview of the microstructure with deformation twins (DTs) taken from the cross section (a). Magnified images of deformation twins (b, c). The insets in (b, c) are the diffraction patterns from deformation twins.

An example of the interaction between deformation twins and CeDBs in P-30% is shown in Figure 4-10. A deformation twin is observed to penetrate through the pre-existing CeDBs (see Figure 4-10 (a)). The misorientation of the twin boundary is found to differ from the perfect  $60^\circ/\langle 111 \rangle$  due to subsequent deformation (the misorientation angle is observed to go to as low as  $48^\circ$ ). Although it appears to be rather ‘clean’ inside the twin in the current view, dislocation boundaries are observed when the sample is tilted to a proper position. A few stacking faults, aligned parallel to the deformation twin, are also observed (see Figure 4-10 (a)). Another example (Figure 4-10 (b)) exhibits double sets of twins intersecting with each other inside the cellular structure, e.g. at the CeDBs marked by the white dashed line. Figure 4-10 (c) shows an example

of extensively developed deformation twins inside the cellular structure, which is marked by the white dashed lines. Most deformation twins are observed to penetrate the CeDBs while some are stopped by CeDBs as marked by the arrows in Figure 4-10 (c). For the deformation twins seen on the right side, the perfect  $60^\circ/\langle 111 \rangle$  misorientation relationship of twin boundaries is destroyed by dislocations, which are marked by the white arrows. It should be also noted that the almost equiaxed cellular structure in P-0 (see Figure 4-3) are now compressed along the ND (see Figure 4-10 (a) and (b)) due to cold rolling.

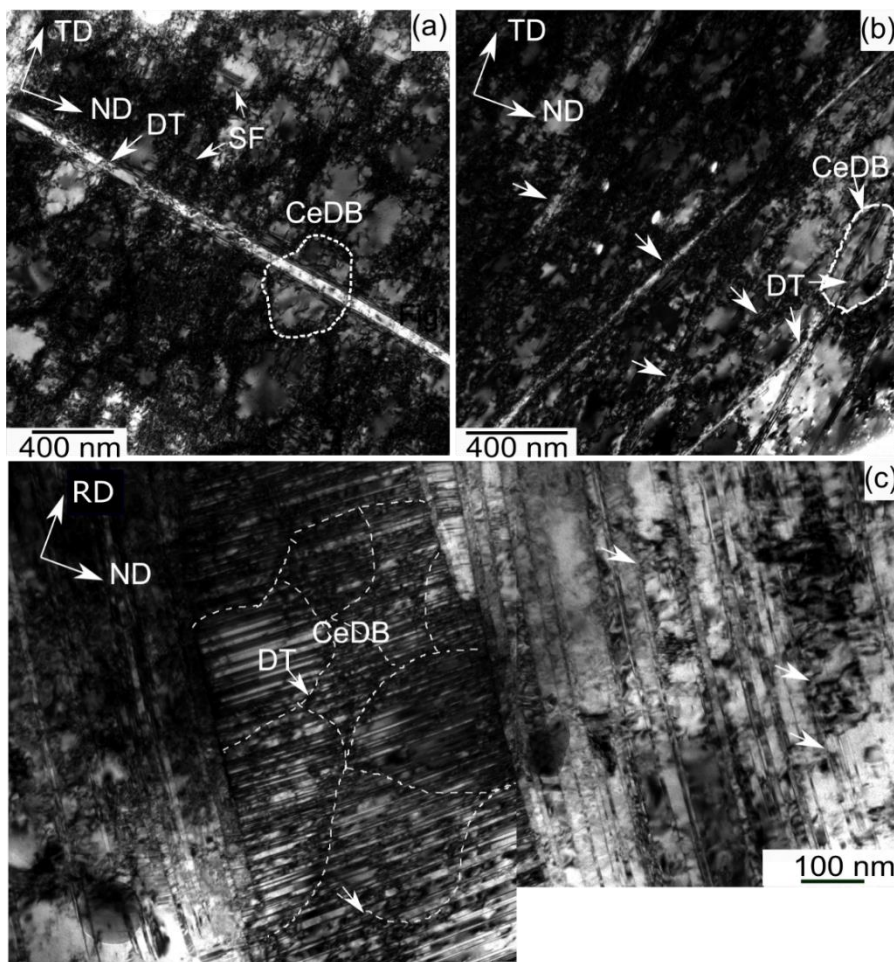


Figure 4-10 Bright field TEM images showing the interaction between CeDBs and deformation twins in P-30%. (a) Cross section view, showing one deformation twin (DT) develops in a cellular structure. Some stacking faults (SF) parallel to the deformation twin are also observed. (b) Cross section view, showing double sets of twins intersect with each other at the CeDBs, e.g. marked by the white dashed line. (c) Longitudinal section view, showing extensively developed deformation twins in one cellular structure. The white dashed lines mark the CeDBs.

Microbands (MBs) are commonly observed after 30% reduction, and an example is shown in Figure 4-11. Microbands form by different combinations of slip systems or different partitioning of slip on the same slip systems in neighboring parts of the microstructure, and thus the orientations on the two sides are different. In the present sample, the misorientation angles across the microbands are low, typically less than  $5^\circ$ , and microbands are observed to strongly interact with deformation twins. As a result, twins are commonly observed to be sheared by microbands especially in the longitudinal section as shown in Figure 4-11(b, c).

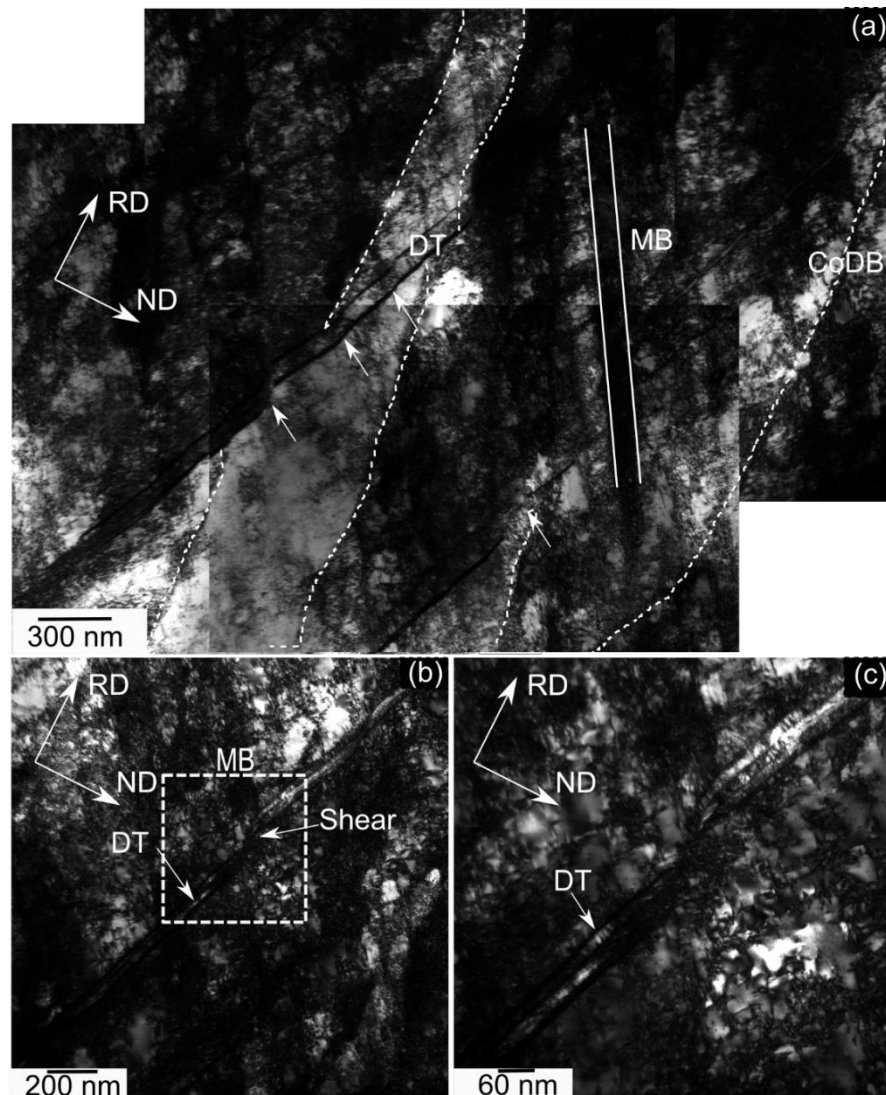


Figure 4-11 TEM images taken from the longitudinal section of P-30% showing the interaction between deformation twins (DT) and microbands (MB). (a) In a columnar structure; (b) In a cellular structure; (c) magnified view of the region marked by the white dashed box in (b). The deformation twins are observed to be sheared by the MBs.

Figure 4-12 shows an example of the typical dislocation structure in areas without deformation twins. There is a high density of dislocations between the pre-existing CoDBs/CeDBs. As shown in Figure 4-12 (a), these dislocations start to organize into new cells of smaller size than that of the pre-existing dislocation structure. Figure 4-12 (b) shows interaction between CeDBs and dislocations activated during cold rolling, increasing the width of CeDBs as well as the overall dislocation density.

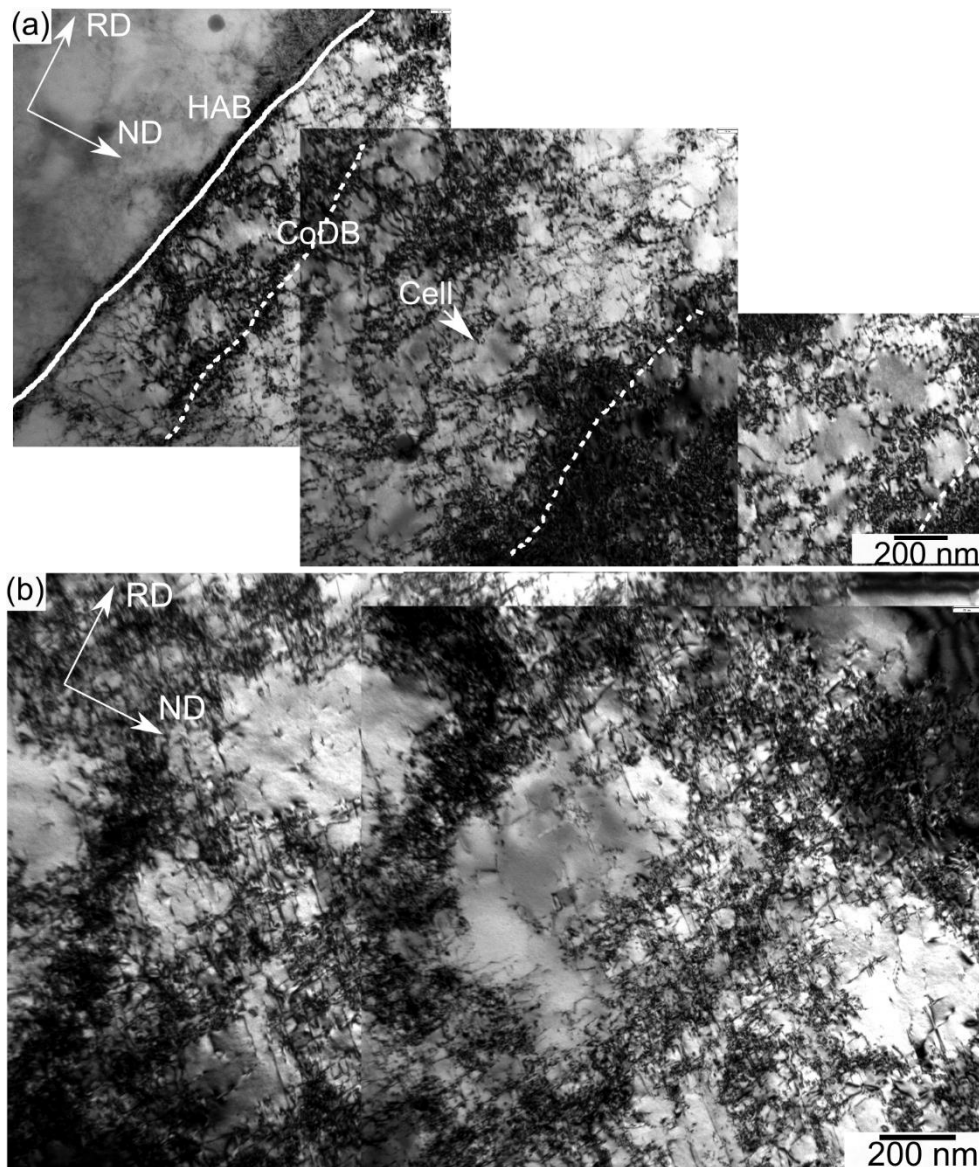


Figure 4-12 Microstructure of areas without deformation twins in P-30%. (a) Formation of new dislocation cells in the columnar structure. (b) Loose dislocations seen inside the cellular structure.

#### 4.3.4 Hardness variation

The hardness measured on the longitudinal section is shown in Figure 4-13, revealing a significant increase by cold rolling. Also shown is the hardness variation of conventionally manufactured 316L samples during cold rolling (denoted as C-0, C-10%, C-30%) from a previous study [163] for comparison. The hardness of P-0 is considerably higher than that of C-0, indicating high strength of 3D printed samples. The hardness of P-0 is comparable to that of C-10%, suggesting that the strengthening effect of the 3D printing process is similar to that of 10% cold rolling although the two microstructures are significantly different. The hardness of P-30% is more than 350 Hv, which is comparable to that of C-50%.

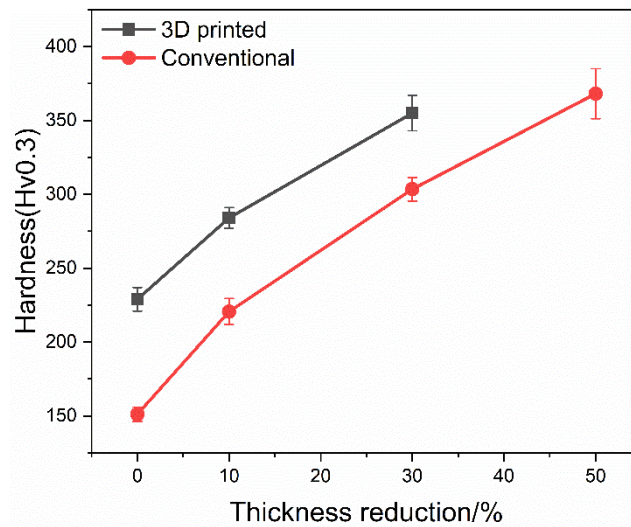


Figure 4-13 Microhardness measured in the longitudinal section (RD/ND plane) of printed and conventionally manufactured samples as a function of deformation strain.

## 4.4 Discussion

### 4.4.1 Deformation of 3D printed 316L samples

After printing of 316L samples, the microstructure consists of domains with rather irregular grain shapes (micrometer scale) each subdivided by cellular/columnar dislocation structures (sub-micron scale). This microstructure is significantly different from that in the initial state of conventionally manufactured 316L and is expected to affect the subsequent deformation behaviour. It is therefore of relevance to analyse the deformation behaviour by comparing the microstructural evolution during deformation in printed samples to that in conventionally manufactured samples. In the present work, the focus is on deformation by cold rolling. The microstructural

evolution during cold rolling (cr) of conventionally manufactured samples has been systematically characterized previously [163], and can be summarized in brief as: At small strain (10-30% cr), a Taylor lattice structure forms due to planar slip of dislocations. Microbands start to form after 30% cr, accommodating a high density of dislocations. Only few deformation twins form at low strain (10% cr), while the volume fraction of twins increases with increasing strain up to 50% cr, forming twin-matrix lamellae. As deformation twinning occurs later than microband formation, it is observed that twins are sheared by the microbands after 30% cr. It was furthermore found that deformation twinning occurs preferentially in grains with Copper orientation rather than Brass orientation and that twinning largely is on planes with the highest Schmid factor for twinning. These results from conventionally manufactured samples serve as a basis for the analysis of the results obtained in the present study.

#### ***A Dislocation activity***

In contrast to the conventional samples, Taylor lattice structures are not observed to form during cold rolling in the 3D printed samples. In 316L, planar slip of dislocations prevails during cold rolling [163,165] due to its low stacking fault energy. Therefore, at low strains, dislocations are activated and glide on one or two favorable {111} slip planes, forming the Taylor lattice structure in conventionally manufactured 316L. However, in 3D printed 316L, the pre-existing dislocation structure acts as an obstacle [20] to the dislocation motion (see Figure 4-5 and Figure 4-6). Therefore, it is difficult for the dislocations to glide continuously to form the Taylor lattice structure. Instead, for areas without deformation twins, small cells form within the pre-existing cellular/columnar structure to accommodate the increasing dislocation density, e.g. Figure 4-12. After 30% cr, the average size of these cells is about 125 nm (see Figure 4-14), i.e. on average one quarter of the original CeDB/CoDB spacing. These deformation induced cell boundaries, in addition to the original HABs and CeDBs/CoDBs, also play an important role in strengthening the materials. For conventionally manufactured metals, the contribution of different boundaries on the mechanical properties has been analysed in detail [166]. Similar detailed work has not been done for 3D printed samples. The boundaries in these samples are, as shown here, dramatically different from those in conventionally manufactured samples. The pre-existing dislocation structure possesses various Burgers vectors and may be subjected to elemental segregation as reported in e.g. [20]. The present study has shown that the

pre-existing dislocation structure in P-0 influences dislocation activation, glide and storage. When comparing the hardness of P-0 to C-0, it is obvious that the strengthening effect of this low angle pre-existing structure is significant.

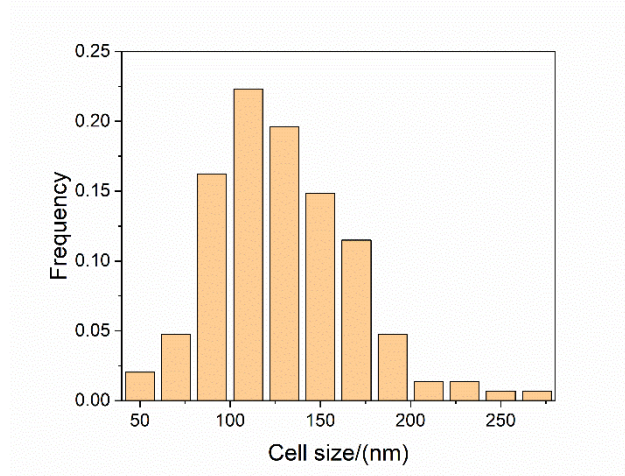


Figure 4-14 The size distribution of dislocation cells in P-30%. The average cell size is about 125 nm, which is a quarter of the original CeDB spacing.

### ***B Deformation twinning behaviour***

Compared to the conventionally manufactured samples, twinning occurs earlier and more extensively in 3D printed samples during deformation. In P-10%, deformation twinning can be detected by EBSD using a step size of 500 nm whereas it is not detectable in C-10% using the same step size. This trend continues and after 30% cr, deformation twinning occurs more extensively in P-30% than in C-30% with the fraction of twin boundaries 72% vs 60% (P-30% vs C-30%) of the total high angle boundary length. It has been reported that deformation twinning is affected by deformation temperature, strain rate, stacking fault energy, and grain size [152]. The first three factors cannot explain the present results as they are similar in the two cases (conventionally manufactured and 3D printed). Concerning the grain size effect, it is generally accepted that larger grains favor deformation twinning [152], although this effect is small for face-centred-cubic (FCC) metals [167]. The grain size of the investigated conventionally manufactured 316L is about 26  $\mu\text{m}$  [163] while it is 33  $\mu\text{m}$  (along BD) and 17  $\mu\text{m}$  (perpendicular to BD) in the present printed sample, suggesting that the grain size can also not explain the difference in deformation twinning in the present case.

It follows that the pre-existing dislocation structure have a major effect on deformation twinning. The dislocations in the pre-existing dislocation boundaries are

mostly dissociated partial dislocations with the Burgers vector  $1/6\langle 112 \rangle$  [24]. Experimental evidence is shown in Figure 4-3, where the partial dislocations glide from one side of a cell to the other side, forming a stacking fault in between during the 3D printing. Since partial dislocations and stacking faults can serve as nucleation sites for twinning, it is thus reasonable to expect earlier and more extensive deformation twinning upon external loading. However, the pre-existing dislocation structure could also act as a weak obstacle to the growth of the deformation twins [20,24]. As mentioned above, some deformation twins are observed to penetrate the dislocation structures while others are stopped (see Figure 4-5). This is attributed to the interaction between twinning partial dislocations and the pre-existing dislocation structure. When a twinning partial encounters a CeDB/CoDB, it may be repelled by the dislocation boundary and only breaks through upon further loading (larger stress). This has been observed by in-situ TEM [24]. Another possibility is that the twinning partial may be trapped by the dislocation boundary through the formation of Lomer-Cottrell locks:

$$\frac{a}{6} [11\bar{2}] + \frac{a}{6} [112] = \frac{a}{3} [110]$$

In the printed samples, there are a large amount of partial dislocations with various Burgers vectors of the type  $a/6\langle 112 \rangle$ , which would react with twinning partials to form such Lomer-Cottrell locks with the Burgers vector  $a/3\langle 110 \rangle$  to reduce the dislocation energy. These dislocations do not easily glide in FCC metals at room temperature due to a large Peierls-Nabarro stress [168]. Therefore, twinning cannot continue in this case. Upon increasing strain, the Lomer-Cottrell locks can cause stress concentration, thereby initiating another partial dislocation. If this partial dislocation inherits the initial Burgers vector, the twinning may continue. If a new partial is initiated, then a new twinning variant can form provided the shear stress is large enough for the growth of the new twins, contributing to the frequently observed double sets of twinning in 3D printed 316L samples.

The present results suggest that the pre-existing dislocation structure can also affect the morphology of deformation twins. Thinner deformation twins are observed in 3D printed 316L than that in conventional samples after deformation (see Figure 4-15). The suggested reason is that pre-existing dislocations may provide nucleation sites for twinning (by providing twinning partial dislocations). The large variety of both twins

and dislocations lead to a more uniform deformation and thin twins in 3D printed samples than in conventional ones.

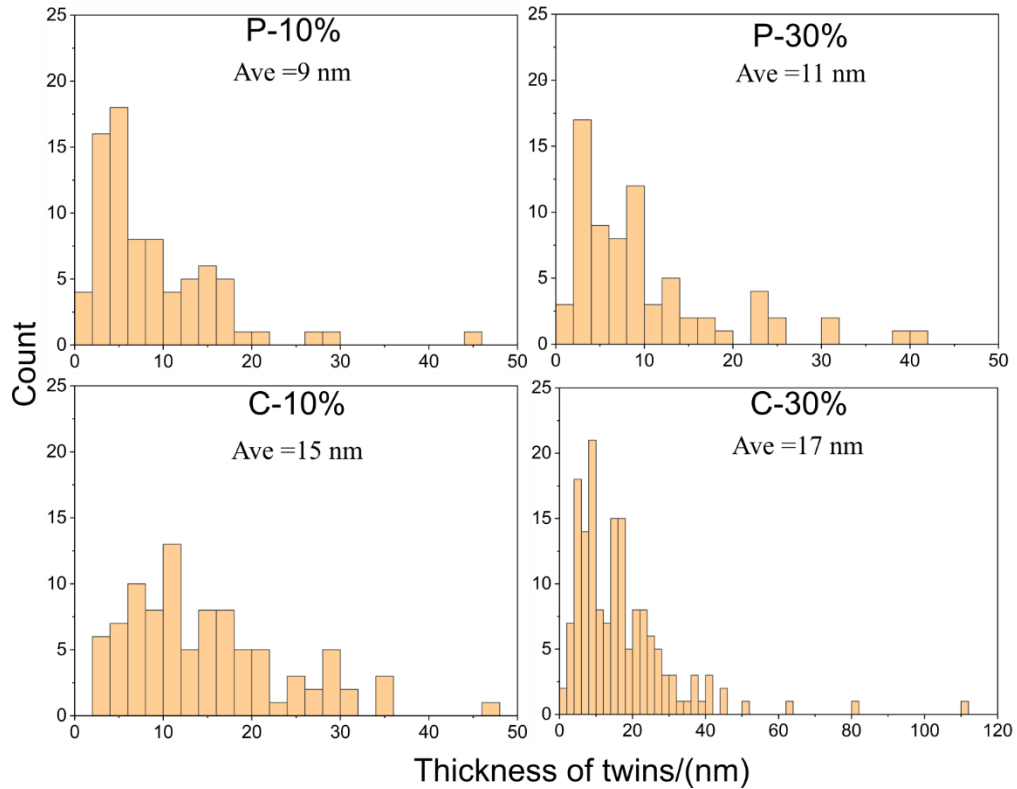


Figure 4-15 The thickness of twins in 3D printed samples (P-10% and P-30%) and in conventionally manufactured samples (C-10% and C-30%). Note that the scale of X-axis for C-30% is different from others. The average twin spacing for the printed samples is smaller than that for the conventionally manufactured samples.

#### 4.4.2 Orientation dependence of deformation twinning

In conventionally manufactured and cold rolled samples, deformation twinning is found to be orientation dependent [163]. In 3D printed samples, we have observed that grains with Brass orientation are not favorable for twinning (see Figure 4-16), similar to the results for conventionally manufactured samples. While many grains with twins in 3D printed samples have an orientation *away from* the Copper orientation (see Figure 4-16(c)), which is the favorable orientation for twinning in conventional samples. To understand this difference, a Schmid factor analysis is done. The Schmid factor for rolling is defined [150] as:

$$m = \frac{(\cos\phi_{RD}\cos\gamma_{RD} - \cos\phi_{ND}\cos\gamma_{ND})}{2} \quad (11)$$

where  $\phi_{RD}$  and  $\phi_{ND}$  are the angles between the slip/twinning plane normal and RD and ND, respectively;  $\gamma_{RD}$  and  $\gamma_{ND}$  are the angles between the slip/twinning direction and RD and ND, respectively. The analysis results in no apparent difference in Schmid factors for twinning ( $m_t$ ) between grains with twins and without twins in the printed sample (see Figure 4-16 (e)). However, higher average ratio of Schmid factors, i.e.  $m_t/m_s$  ( $m_s$  denotes the Schmid factor for slip), is observed for the grains with twins (see Figure 4-16 (c)). Similar results were obtained from conventionally manufactured samples. It is worth to note that there is large overlap between the distribution of  $m_t/m_s$  for grains with twins and that for grains without twins as shown in Figure 4-16 (f). This is due to the high symmetry of FCC metals, resulting in many equivalent slip/twinning systems.

Another difference found is that all the deformation twinning detected by EBSD occurs on the planes having the highest  $m_t$  in C-30% whereas only 13/19 (13 grains out of 19) exhibits the same pattern in P-10% and this probability decreases to 31/100 in P-30%. These phenomena suggest that in 3D printed samples, twinning selection is a more complex process than that in conventionally manufactured samples due to the effects of the pre-existing dislocation structure and irregularly shaped grains.

For the case of double sets of deformation twins, one set of twins develops on the plane with the highest  $m_t$  while the other set develops on a plane with very low  $m_t$  (near zero). As a shear stress is needed for the motion of partial dislocations on the twinning plane for twin propagation, large internal stresses are expected in the 3D printed samples with irregularly shaped grains and pre-existing dislocation structures. Both the irregularly shaped grains and pre-existing dislocation structures can cause a complex local stress state and therefore provide the resolved shear stress required for the development of deformation twins on planes other than the one with the highest  $m_t$  during the subsequent cold rolling. However, further understanding of this phenomenon requires more information on relations between the 3D microstructure and the local residual stress, which may be obtained by advanced experimental studies using the 3DXRD technique [169].

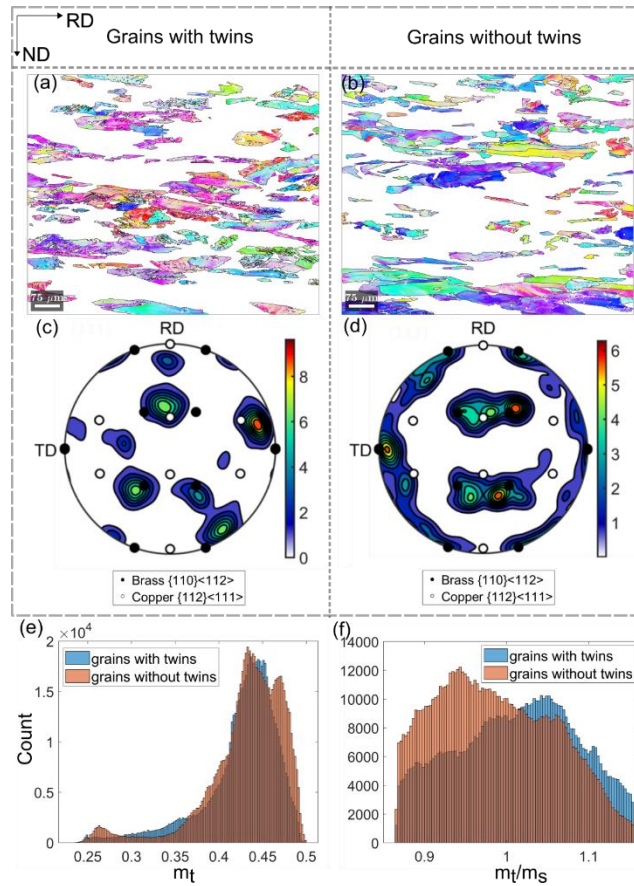


Figure 4-16 Difference between grains with twins and without twins in P-30%. (a, c) Orientation map and  $\{111\}$  pole figure of grains with twins in P-30% (Figure 3-8(a)), respectively. (b, d) For grains without twins. (e) The highest Schmid factor for twinning ( $m_t$ ). (f) Ratio of the highest Schmid factor for twinning ( $m_t$ ) to the highest Schmid factor for slip ( $m_s$ ), i.e. ( $m_t/m_s$ ). The grains with twins show an orientation away from Copper orientation; the grains without deformation twins show an orientation near Brass orientation. There is no obvious difference in the highest Schmidt factor for twinning between grains with twins and grains without twins, whereas the ratio of Schmidt factors ( $m_t/m_s$ ) is higher for grains with twins.

## 4.5 Conclusion

We suggest that it is important to understand how 3D printed samples behave when they are in use, including being exposed to plastic deformation. Here we have shown that the pre-existing dislocation structure introduced by printing plays an important role during subsequent deformation of 3D printed 316L stainless steel samples. It affects the nucleation and motion of dislocations and the deformation twinning behaviour. The conclusions are as follows:

1. The pre-existing dislocation boundaries suppress continuous planar slip of dislocations, and therefore the Taylor lattice structure, which is commonly observed in conventionally manufactured 316L, does not develop in 3D printed samples.
2. The pre-existing dislocation structure promotes initiation of deformation twinning, which occurs earlier and with a higher number density of twins in 3D printed than in conventionally manufactured samples. This is because the pre-existing dislocation structure facilitates deformation twinning by providing twinning partial dislocations. Yet, this structure also acts as an obstacle — either as a repelling force between dislocations or by forming Lomer-Cottrell locks.
3. The high strength of 3D printed samples are attributed to: i) The pre-existing dislocation structure, which is on a sub-micron scale. ii) The preferential formation of deformation twins, which decreases the spacing of HABs in 3D printed samples. iii) Small cells formed inside the pre-existing dislocation structure during deformation.

## **Acknowledgement**

The authors gratefully acknowledge support from the European Research Council (ERC) under the European Union's Horizon 2020 research and innovation programme (grant agreement No.788567) for the M4D Advanced Grant within which this work is performed. CZ further acknowledges the financial support of the China Scholarship Council (CSC) (NO. 201706120026).

# Chapter 5: Annealing behaviour of 3D printed 316L

---

This chapter focuses on the annealing behaviour of the 3D printed samples (P-0 and P-30%), as well as of the C-30%. The overall recrystallization behaviour is analysed and the results are shown in Section 5.1. Section 5.2 shortly summarizes the obtained 2D and 3D information about the voids in P-0. The aim is to report what type of voids are observed in the present printed samples rather than an in-depth analysis. Voids are expected to affect the recrystallization behaviour during post-printing heat treatment. In manuscript III (Section 5.3), a modified phase field recrystallization model is proposed to analyse the effect of voids on boundary kinetics.

## 5.1 Recrystallizing microstructure of 316L

### 5.1.1 C-30%

After annealing at 850 °C (in this chapter the default annealing temperature is 850 °C; in some cases 900 °C was used as then specifically indicated) for less than 1 h, no obvious recrystallizing nuclei are observed (see Figure 5-1). With increasing annealing time (after 2 h), recrystallization nuclei develop and grow. To quantify the fraction of recrystallized material, recrystallizing grain/nuclei are identified by the criterion: a maximum grain orientation spread (GOS) of 0.5° and a minimum size of 2 µm. The recrystallizing grain/nuclei The recrystallized fraction is calculated by  $f = \frac{S_{rex}}{S_{eb sd}}$ , where  $S_{rex}$  is the area of recrystallizing grains and  $S_{eb sd}$  is the total area of relevant EBSD map. By this method it is found that after annealing at 900 °C for 5 h, the sample is 88% recrystallized, as shown in Figure 5-2.

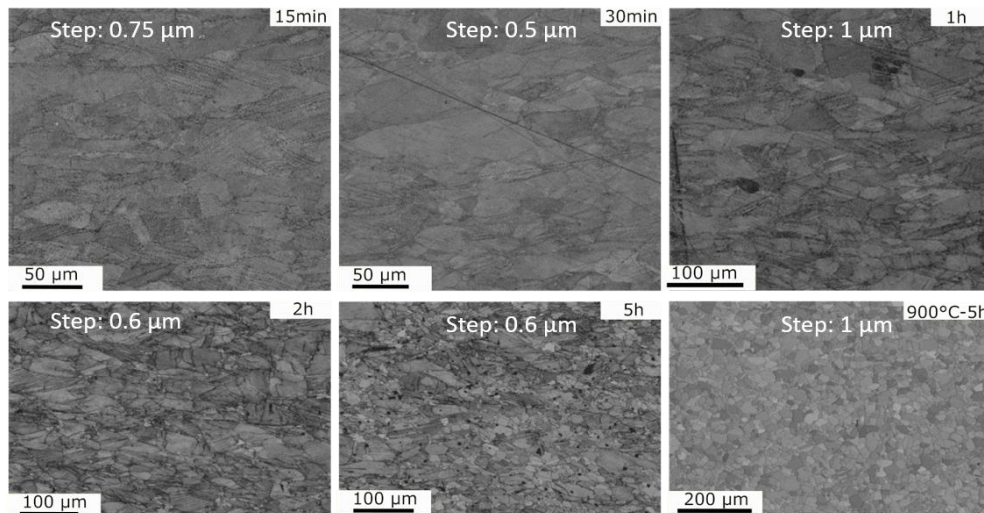


Figure 5-1 Band contrast maps for C-30% samples annealed at 850 °C for 15 min, 30 min, 1 h, 2 h and 5 h. The bottom-right panel presents the case for 900 °C for 5 h.

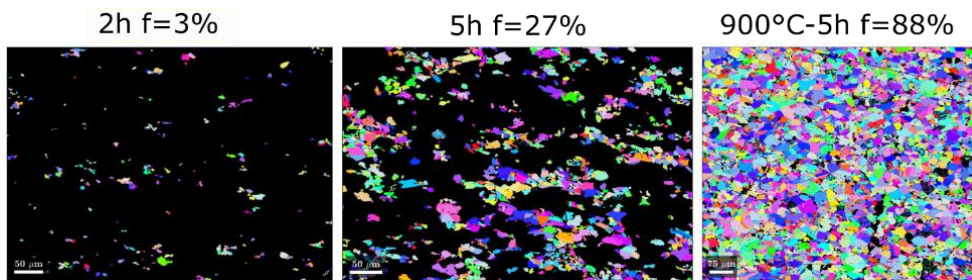


Figure 5-2 Recrystallizing grains determined from EBSD maps of annealed C-30% samples. A maximum grain orientation spread (GOS) of  $0.5^\circ$  and a minimum size of 2 μm are chosen to identify the recrystallizing grains.

### 5.1.2 3D printed 316L; P-0 and P-30%

No obvious recrystallization is observed in the as-printed samples (P-0), even after annealing at 900 °C for 5 h, as shown in Figure 5-3. This may be related to the low annealing temperature used here. Other studies of printed 316L samples have shown that the recrystallization temperature is 1150 °C [170]. However, this was not investigated in the present work.

For P-30%, EBSD maps reveal some nuclei developing inside the deformed grains already after annealing at 850 °C for 15 min. An example is marked by the white dashed rectangle in Figure 5-4. In addition, nuclei are found to develop at boundaries of deformation twins (see the arrows in the 15 and 30 min cases). This may be attributed to the high stored energy there resulting from strong dislocation-twin interaction in P-30%, as described in Chapter 4. It is worth noting that recrystallization in P-30% is rather inhomogeneous. This is clear already after the shortest annealing

time of 15 min. To quantify recrystallization properly in the P-30% samples, large EBSD acquisition areas are necessary (e.g. the case of 1 h with an area of  $1.5 \times 1.2 \text{ mm}^2$ ). An almost fully recrystallized microstructure is observed after annealing at 900 °C for 5 h, and this microstructure is rather inhomogeneous. The recrystallization fractions for P-30% and C-30% are determined based on the EBSD data and summarized in

Figure 5-5. The recrystallization of P-30% starts earlier and progresses faster than that of C-30%. An incubation time of 1 h is observed for C-30% (see

Figure 5-5) As expected, the recrystallizing grain size increases during annealing for both C-30% and P-30% (see Figure 5-6). It is worth noting that the large grain size in C-30% is likely due to the large step size used for this condition.

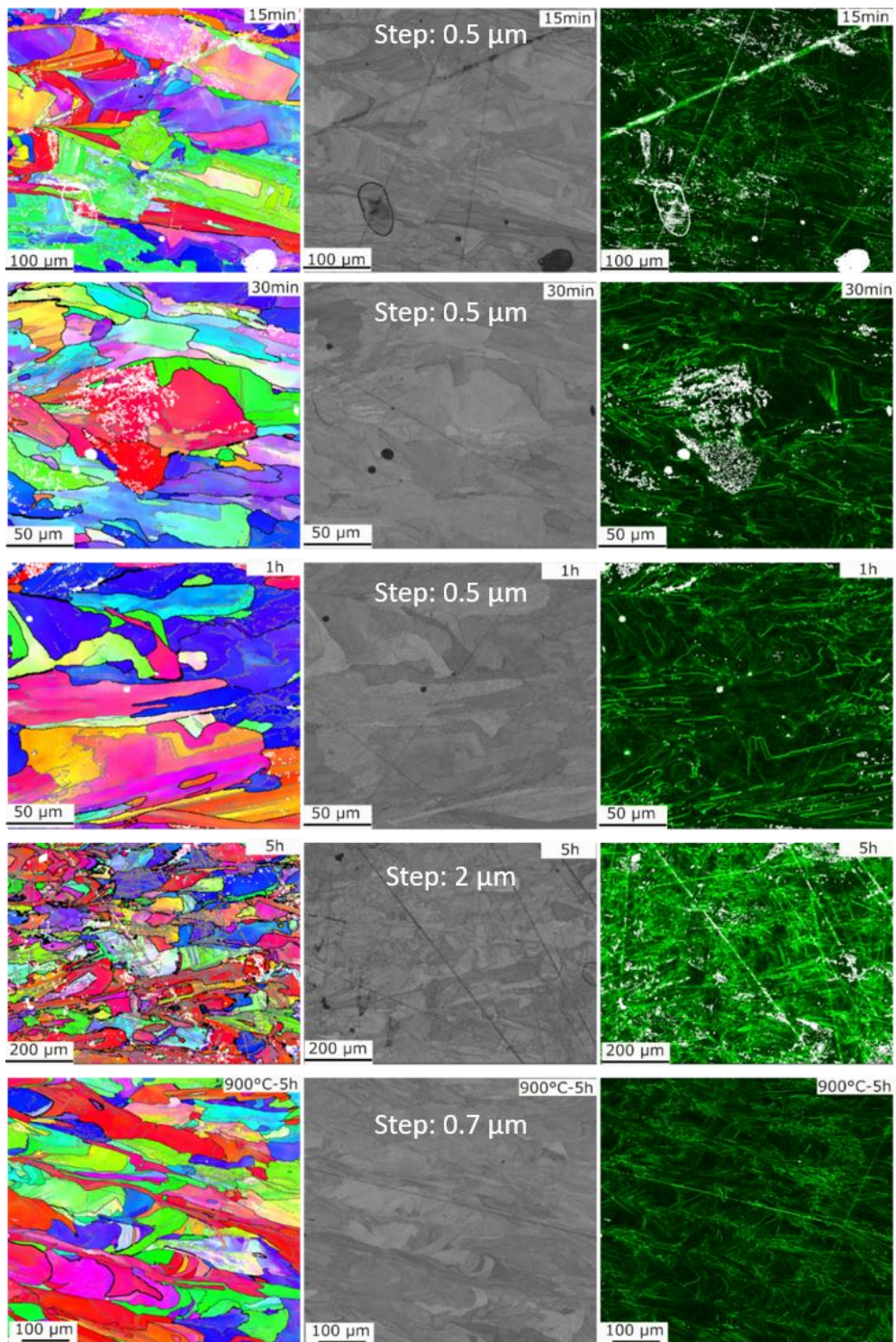


Figure 5-3 Annealing of the as-printed samples (P-0) during annealing. Left column: EBSD orientation maps; middle column: band contrast maps; right column: KAM maps.

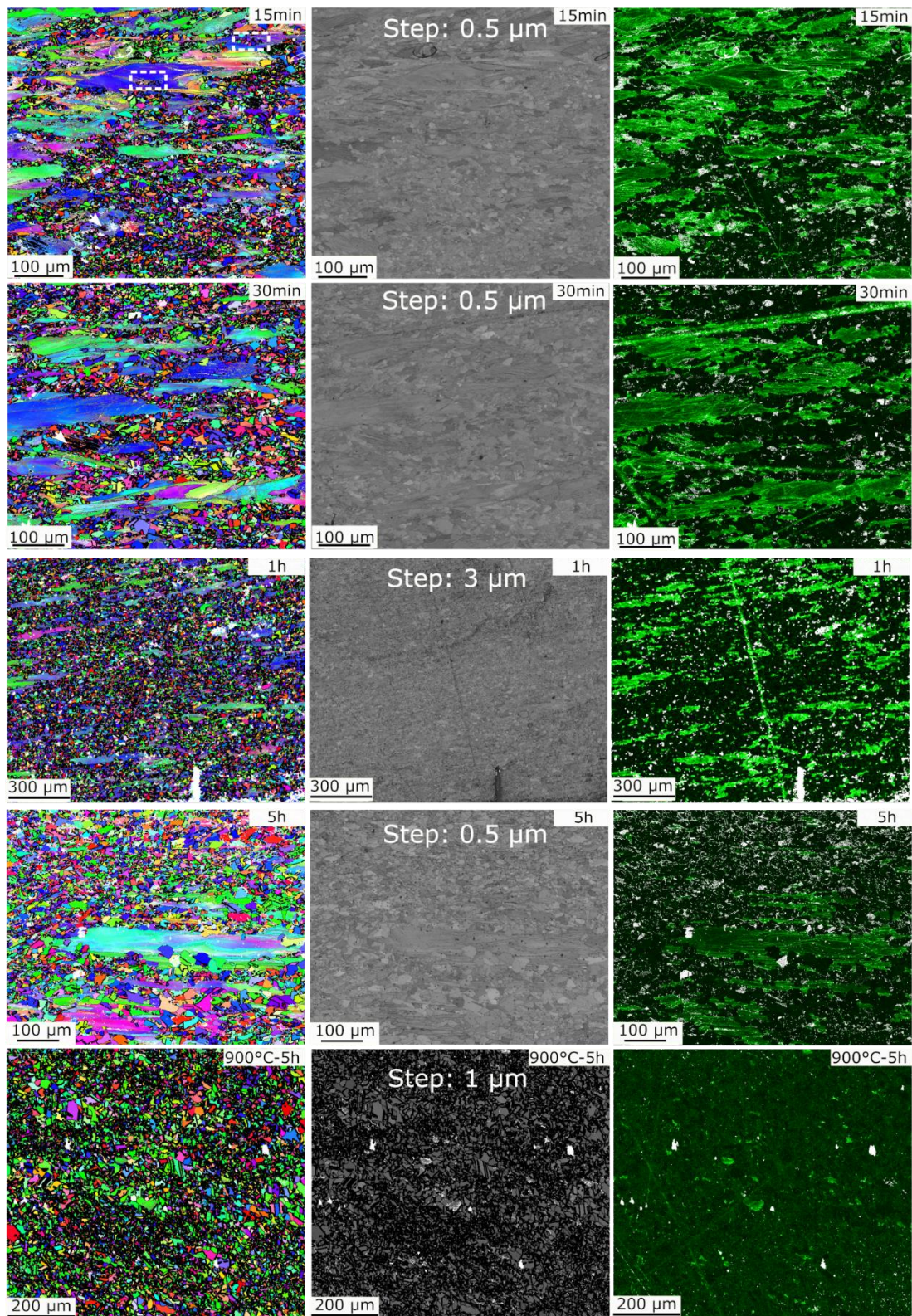


Figure 5-4 Annealing of P-30%. Left column: EBSD orientation maps; middle column: band contrast maps; right column: KAM maps.

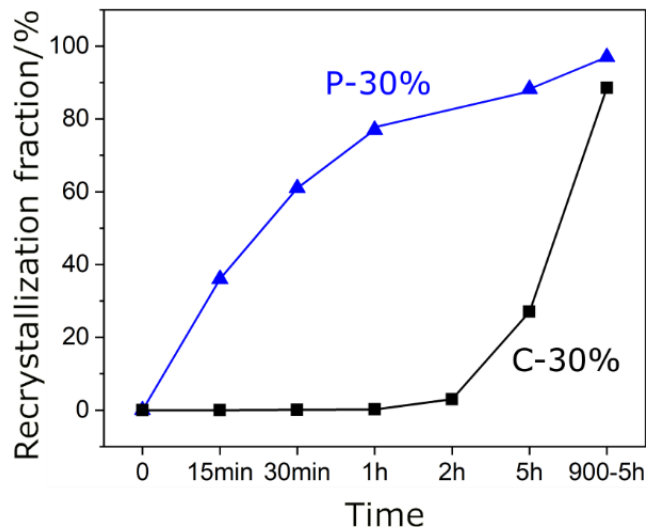


Figure 5-5 Recrystallization fraction of P-30% and C-30% as a function of annealing time.

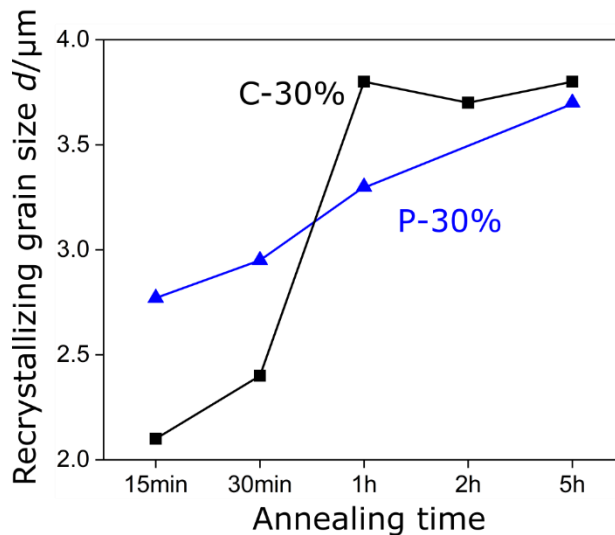


Figure 5-6 Average recrystallizing grain size as a function of annealing time.

### 5.1.3 Mechanical properties

The EBSD characterization has revealed that recrystallization starts earlier in P-30% than C-30%, while no recrystallization is observed at the present annealing temperatures for the as-printed sample (P-0). This matches well with results obtained by hardness measurements. The hardness of P-30% decreases faster than C-30% as a function of annealing time and the hardness hardly drops in P-0, as shown in Figure 5-7 (a). Both P-0 and P-30% reach a plateau in hardness (Hv 190) after annealing at 850 °C for 1 h. After annealing at 900 °C for 5 h, the hardness of C-30% is reduced to Hv 160, close to Hv 151 for the solution treated C-0. There is an increase in hardness of C-30% after annealing for 30 min. If this slight increase is statistically significant, it could be related to the formation of the  $\sigma$  phase [171].

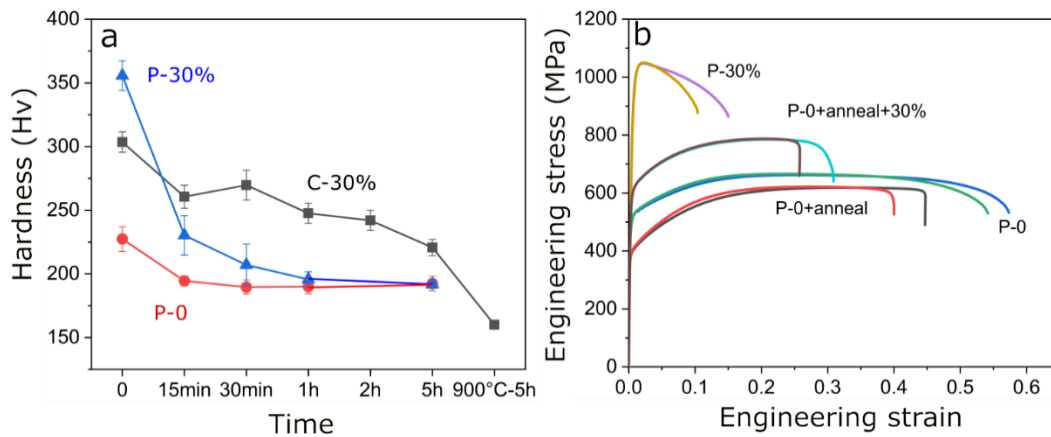


Figure 5-7 Mechanical properties. (a) V-hardness variation of C-30%, P-0 and P-30% with annealing time. Note the last data point of C-30% is obtained at 900 °C for 5 h. (b) Tensile properties of 3D printed samples. P-0: as-printed samples; P-0+anneal: the as-printed sample annealed at 850 °C for 1 h; P-0+anneal+30%: the as-printed sample annealed at 850 °C for 1 h plus 30% rolling reduction in thickness. Two specimens were prepared for each condition.

Although there is no obvious recrystallization observed in the as-printed samples during annealing at the present annealing temperatures, the yield strength decreases after annealing. Whereas the cellular/columnar boundaries have been reported to be stable after annealing at 800 °C for 1 h [172], the dislocation density decreases during this recovery period which matches well with the observed decrease in strength. Based on the analysis presented in Chapter 4, the cellular/columnar boundaries with dislocations of complex Burgers vectors affect dislocation multiplication and motion as well as deformation twinning. Comparing the tensile curves of P-0 and P-0+anneal, it is suggested that the effect of cellular/columnar boundary has been changed after annealing, which may contribute to the decrease in both strength and ductility of the annealed samples. This work suggests the necessity of further investigation on the thermomechanical behaviour to optimize the properties and thus promote the application of 3D printed 316L.

Overall, the results show significant variations in mechanical properties after plastic deformation and annealing. When a printed part is in use, it is likely to be exposed to mechanical and/or thermal loads, and the present results underpins the importance of understanding how such loads affect the microstructure and thus properties of the part. Assuming properties as those in the printed condition is not appropriate.

## 5.2 Voids in 3d printed 316L

Voids are present both within the surface regions and in the bulk centre in 3D printed samples. An example is shown in Figure 5-8 a and b. Here voids are marked by the white arrows in the optical micrographs. In addition, melt pool traces are apparent,

revealing a  $67^\circ$  rotation between adjacent layers during the present printing process. In the X/BD plane (image b) it can be seen that the depth of the melt pool varies with building direction.

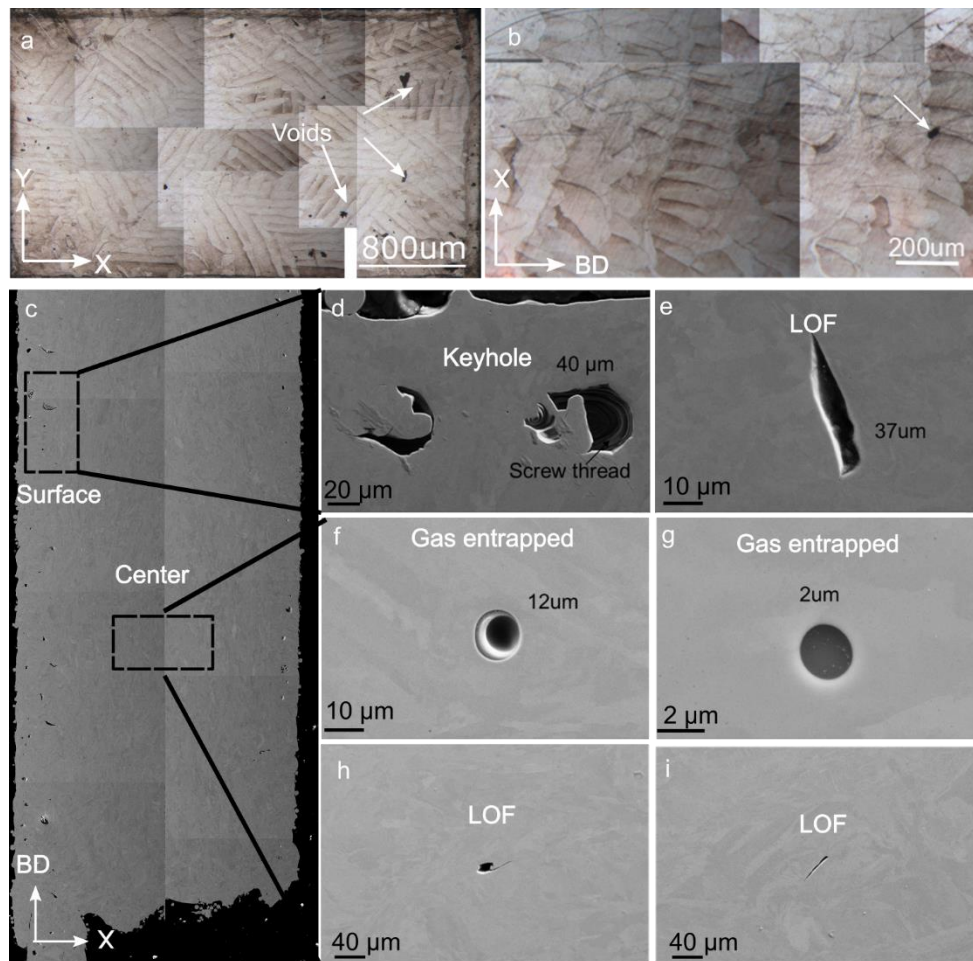


Figure 5-8 Voids in the as-printed samples P-0. (a,b) Optical micrographs; (c) SEM montage; (d,e) SEM micrographs taken from the surface region; (f-g) SEM micrographs taken from the centre region.

The sizes of voids vary in the range of 1-100  $\mu\text{m}$ . Keyhole voids, with sizes of around 40  $\mu\text{m}$ , mainly form near the sample surface because the power input there is high due to overlap of laser traces. It is interesting to observe the thread-like morphology inside some keyhole voids (e.g. see image d).

LOF voids are also frequently observed in volumes near the sample surface while they rarely form inside the bulk components. LOF voids are typically needle-shaped with sharp tips when observed on a 2D section. The long axis of LOF voids can be as large as 100  $\mu\text{m}$  (see image i), indicating that the LOF voids formed during printing

can cross several layers. There can be partially melted powder particles left inside the LOF voids, as shown in image e.

Gas entrapped voids mainly form at the centre volumes of the samples. Gas entrapped voids are much smaller than keyhole and LOF voids. The gas entrapped void shown in image f may come from powder particles, which contains gas from the gas atomization process [30].

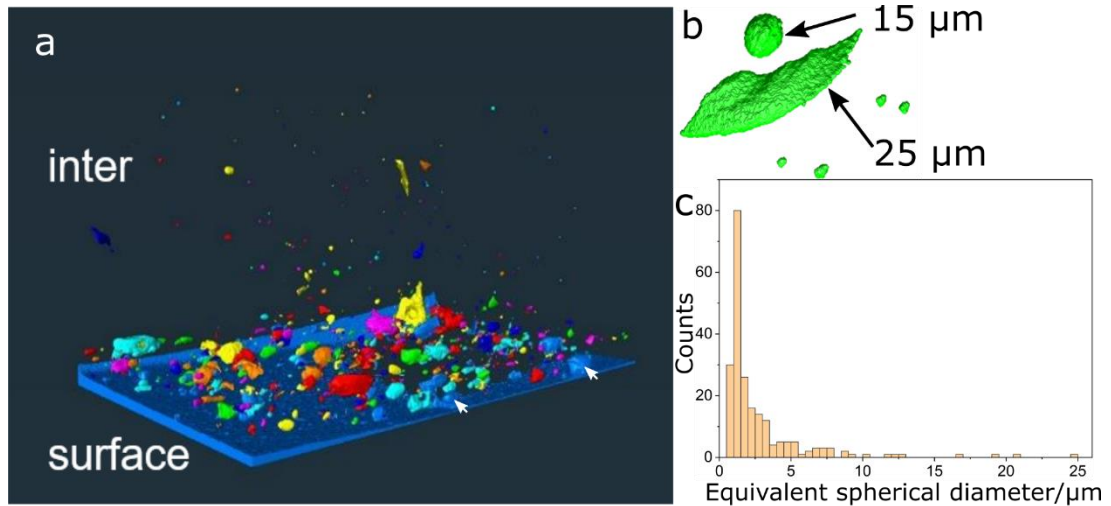


Figure 5-9 3D information about voids obtained from X-ray tomography using absorption contrast. (a) 3D reconstruction showing a sample volume of  $318 \times 300 \times 512 \mu\text{m}^3$ ; (b) Selected examples of the voids; (c) Distribution of equivalent spherical diameters of the voids.

To characterize voids in 3D, X-ray tomography is used. The 3D information is obtained by reconstructing the absorption contrast data and the voids in P-0 are shown in Figure 5-9. It is worth noting that those with sizes smaller than  $1 \mu\text{m}$  in equivalent spherical diameter are considered as noise rather than voids in the data reconstruction. Voids near the surface are larger than those in the bulk interior, consistent with the results obtained from OM / SEM observations. Within the surface regions, there are mushroom-shaped voids, which are open to the air rather than closed and therefore cannot be removed by heat treatment or HIP. These may be keyhole voids that affect the surface roughness and thus the corrosion resistance and fatigue properties of the printed components [17,173]. Inside the bulk, there are mainly only small spherical voids with diameters in the range of  $2\text{-}5 \mu\text{m}$ , yet also a low density of LOF voids exist here. A particular example is shown in Figure 5-9 b. The void with an equivalent diameter of  $15 \mu\text{m}$  may be a keyhole void while other four small spherical voids may be gas entrapped voids. The plate-shaped void represents a LOF void with diameter

25  $\mu\text{m}$ . Most of the voids in the printed samples are less than 10  $\mu\text{m}$  in equivalent spherical diameter whereas a few may be as large as 25  $\mu\text{m}$  (see Figure 5-9 c).

### **5.3 Effect of voids on recrystallization behaviour of 3D printed samples**

As shown above in Section 5.2, voids appear to be unavoidable even when the best industrial printing process is used. Post processing like heat treatment is usually carried out to reduce the size of voids and optimize the microstructure in printed components before they are used. Also printed components may be exposed to heat while they are in use. Voids are expected to affect the recrystallization behaviour during heat treatment but the effect has not been thoroughly investigated yet. Therefore, in this thesis, phase field simulations are performed, to understand the effect of voids on the recrystallization behaviour of 3D printed components. In manuscript III (Section 5.3.1), the effect of voids on boundary migration is analysed by for a few idealized deformation microstructures created to mimic the printed microstructure.

#### **The effect of voids on boundary migration in additive manufactured samples—a phase field study (Manuscript III)**

##### **Abstract:**

Experimental results show that voids inside additive manufactured (i.e. 3D printed) materials are unavoidable. As such samples are often post-printing annealed, it is thus of interest to understand how voids affect boundary migration. In this work, phase field simulations of recrystallization are carried out for systems containing voids and typical inhomogeneous microstructures. The simulation results show that the voids significantly affect the shape of the boundary and its migration kinetics during recrystallization. The location of the voids in relation to the inhomogeneous deformation microstructure is furthermore found to affect local boundary migration. The results are not only of importance for optimizing annealing of printed samples, but also for understanding local boundary migration in particle containing alloys.

Additive manufacturing (also known as 3D printing) has drawn enormous attention during the last few decades in particular due to its advantage in net-shape manufacturing of components with complex shapes [1–3]. However, an important feature in 3D printed metallic samples is voids, which appear to be unavoidable, even though samples of high density (>99.7%) can be obtained by careful control of printing

parameters [20]. These voids may be detrimental to the mechanical properties for example strength, Young's modulus, and fatigue properties [3,35]. To reduce the effect of voids, post-printing treatments like hot isostatic pressing (HIP) are often used [37]. However, voids, in particular gas containing voids, remain even after HIP and may play a role during the post-printing heat treatment. To the best of the authors' knowledge, it has not yet been quantified how interior voids affect the recrystallization behaviour of 3D printed metallic samples. The topic is of importance *both* for establishing efficient post-printing annealing and for understanding how interior surfaces affect recrystallization. In a series of ex-situ annealing experiments followed by electron backscatter diffraction (EBSD) characterization, we have observed that the voids significantly affect the boundary migration during recrystallization. This is exemplified in Here, the horizontal boundary is dragged by a void (marked by the upper white arrow in each panel shown in Figure 5-10), similar to a particle Zener pinning effect, until the last annealing step.

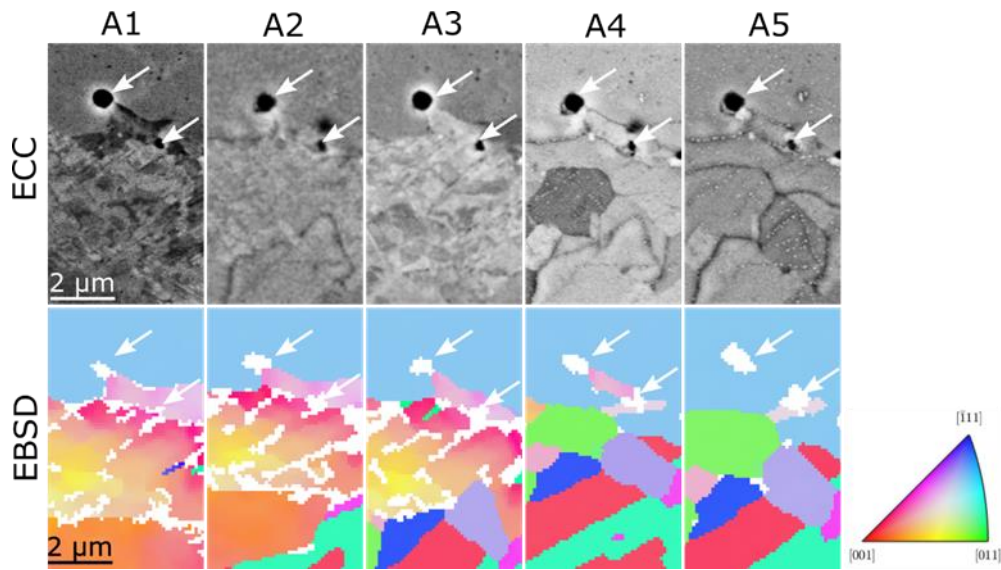


Figure 5-10 Observation of boundary migration during recrystallization of a 3D printed 316L sample which was 30% cold rolled after printing. The white arrows mark the voids. The micrographs show the pinning effect of the void on the grain boundary migration. First row: electron channeling contrast (ECC) images; Second row: EBSD orientation maps. The EBSD maps are coloured based on the crystallographic orientation of the observing surface normal; white indicates non-indexed pixels. A1–A5 denote five subsequent isothermal annealing steps (see supplementary materials **S1** (Appendix C) for more details).

It is worth noting that experimental errors (due to sample mounting and drift) appear to distort the EBSD maps. However, this is not important for the present work, as the

data are not used for a direct comparison with the simulations. In cases where precise information about the boundary positions are needed, the ECC data should be used. For more details about this experimental work, readers are referred to the supplementary materials **S1** (Appendix C).

Since Smith and Zener proposed the effect of particles on boundary migration [174], there has been extensive theoretical analysis, dealing with the complexity of particles (e.g. particle size, shape and distribution) and of boundary geometries [175–178]. Moreover, computer simulations of microstructural evolution during recrystallization and grain growth in systems containing particles were carried out using Monte Carlo Potts model, level-set finite element model, vertex, front tracking and cellular automata [88,92,109,179–181] and *phase field modeling* [108]. During the last two decades, the phase field (PF) method has been developed and successfully utilized for simulation of recrystallization [81,115,182,183]. Important factors for recrystallization, namely, stored energy, grain boundary characteristics [81,111] and local geometrical arrangement of dislocation boundaries in the deformed microstructure [85,112,113], have been analysed by using the PF simulation. In order to understand the effect of voids during recrystallization, we introduce a modified PF model, which can perform simulations in both homogeneous and inhomogeneous microstructures; with and without voids.

In the present study, we introduce a void into the PF model [81] for a few idealized cases of deformation microstructures (see Figure 5-11). The free energy function for the system is:

$$F = \int_{\Omega} [F_{gb} + F_s] d\Omega \quad (12)$$

where  $\Omega$  is the simulation domain. The contribution from grain boundary  $F_{gb}$  (based on Chen and Yang's grain growth model [115] and the expression in [114]) is shown in Eq. (2), where  $\eta_{rex,i\dots p}$  and  $\eta_{def}$  denote the order parameters for recrystallizing grains and deformed microstructure, respectively. The stored energy  $F_s$  is given in Eq. (3), where  $f_{def}(x,y)$  is the free energy density and  $\phi_{def}$  is the local fraction of deformed field within the simulation domain. The parameter  $p$  denotes the number of recrystallizing grains simulated.

$$\begin{aligned}
F_{gb} = & m \left[ 0.25 \left( \sum_{i=1}^p \eta_{rex,i}^4 + \eta_{def}^4 \right) - 0.5 \left( \sum_{i=1}^p \eta_{rex,i}^2 + \eta_{def}^2 \right) + \right. \\
& 1.5 \sum_{i=1}^p \sum_{i \neq j} \eta_{rex,i}^2 \eta_{rex,j}^2 + 1.5 \eta_{def}^2 \sum_{i=1}^p \eta_{rex,i}^2 + 0.25 \left. \right] + \\
& \epsilon \Phi^2 \left( \sum_{i=1}^p \eta_{rex,i}^2 + \eta_{def}^2 \right) + \frac{\kappa}{2} \left( \sum_{i=1}^p |\nabla \eta_{rex,i}|^2 + |\nabla \eta_{def}|^2 \right) \quad (13)
\end{aligned}$$

$$F_s = f_{def}(x, y) \cdot \phi_{def} = f_{def}(x, y) \cdot \frac{\eta_{def}^2}{\sum_{i=1}^p \eta_{rex,i}^2 + \eta_{def}^2 + \Phi^2} \quad (14)$$

The modification made here is that a new parameter  $\Phi$  is introduced to represent the void and therefore expressions of  $F_{gb}$  and  $F_s$  are correspondingly modified (see Eq. (2) and (3)). The model parameters  $\kappa$  and  $m$  are related to the grain boundary energy  $\sigma_{gb}$  and diffuse interface width  $\iota_{gb}$ ,  $\kappa = 3/4 \cdot \sigma_{gb} \cdot \iota_{gb}$  and  $m = 6 \cdot \sigma_{gb} / \iota_{gb}$ . A region with  $\eta_{rex,i} = 1, \eta_{def} = 0$  and  $\Phi = 0$  represents a recrystallized grain, a region with  $\eta_{rex,i} = 0, \eta_{def} = 1$  and  $\Phi = 0$  represents the deformed microstructure, and a region with  $\eta_{rex,i} = 0, \eta_{def} = 0$  and  $\Phi = 1$  represents the void. More information about the present PF model is given in the supplementary materials **S2** (Appendix C) and in Ref. [81,114].

Both homogeneous and inhomogeneous microstructures are considered (see Figure 5-11). For convenience, the homogeneous microstructure is denoted as HM while the inhomogeneous microstructure, i.e. the sine function defined one is denoted as SM. The SM, containing two sets of planar dislocation boundaries, has been used in PF simulation previously to mimic typical deformed microstructures [81,85,112,163] and it is also reasonable to use the same for printed microstructures, i.e. for cellular structures. Details about the SM can be found in the supplementary materials **S3** (Appendix C). The average stored energy is set to be  $0.51 \text{ MJ/m}^3$ , in both the HM and SM simulations. All simulations have the same system size of  $478 \times 1000$  grid points with a grid spacing  $\Delta x = 14.1 \text{ nm}$ . For the simulations with a single recrystallizing grain (Rex), the initial recrystallizing grain size is  $478 \times 170$  grid points; for the simulations with 3 recrystallizing grains, as an example to show the effect of multiple grains, the sizes of Rex1 and Rex3 are chosen to be  $149 \times 170$  while Rex2 is  $180 \times 170$  grid points. The voids are chosen to be spherical with a radius of 65 grid points. To investigate effects of the void position in the SM case, two positions are chosen: one at the grid position (300, 239) and the other at (352, 239). For comparison, identical simulations without voids are also performed. Parameters typical for pure Al are

chosen here (taken from [184]) to ease comparison with previous PF simulations of recrystallization in similar microstructures but without voids. The mobility of the grain boundary is set to  $\mu_{gb} = 6 \times 10^{-14} \text{ m}^4/(\text{J}\cdot\text{s})$ ; the grain boundary energy  $\sigma_{gb} = 0.32 \text{ J/m}^2$ ; and the time step  $\Delta t = 0.0023 \text{ s}$ . It is worth noting that the present PF model can be also used to simulate recrystallization in systems containing incoherent particles—actually the voids in the present model could as well have been incoherent particles.

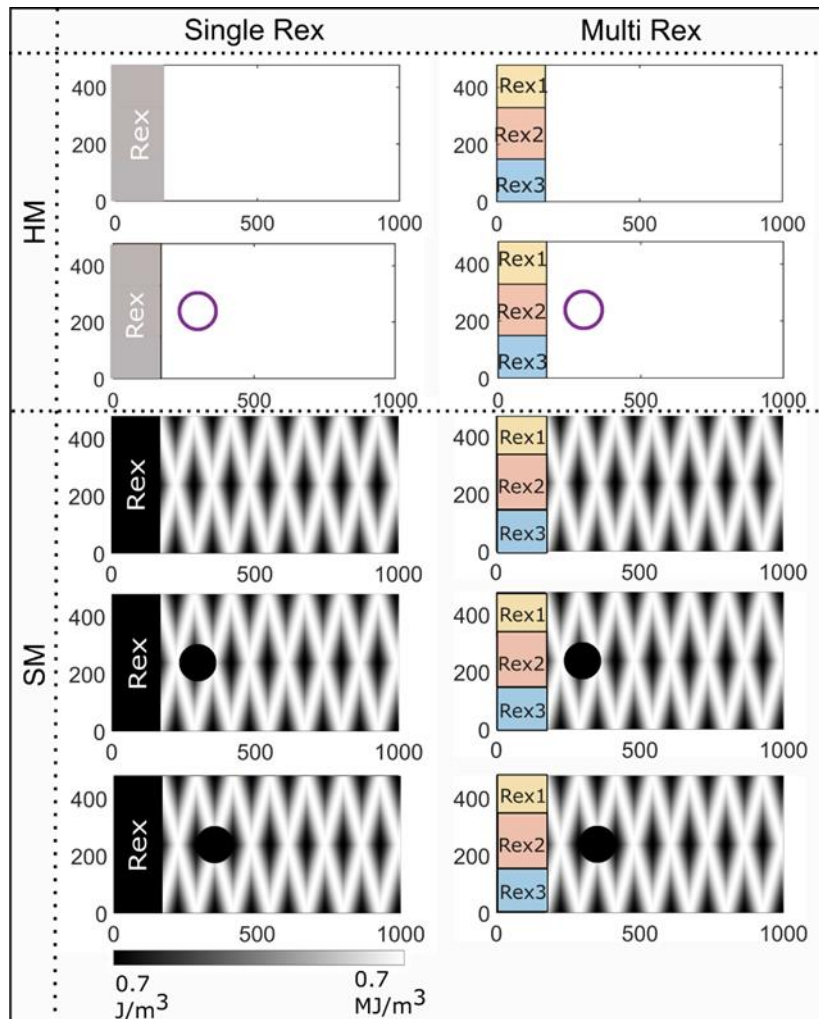


Figure 5-11 Cases simulated in the present study. The deformed microstructures are either homogeneous (HM) or inhomogeneous—sine function defined (SM). The behaviour of one or three recrystallizing grains are simulated. The circle denotes the void.

In the HM case, the boundary migration is very simple (see supplementary materials **S4** in Appendix C) and only included here for comparison reasons. For the SM case without void, the initially straight boundary migrates in a wave-shaped manner due to the local variation in stored energy (Figure 5-12 a1). This is similar to what has been reported in [85]. The velocity variations (see Figure 5-12 a2) show that the boundary

segment encountering high stored energy migrates fast and vice versa. The velocity variations of point 1 and point 3 are similar—with the same frequency and amplitude but of opposite phase. The maximum velocity of point 2 is lower compared to points 1 and 3 due to the lower stored energy encountered by point 2. When the void is included in the simulation, the migration kinetics of point 1 is slightly affected; the frequency of the velocity variation is slightly changed due to the interaction between the void and the boundary (see Figure 5-12 (b2, c2)). In contrast, the boundary kinetics of points 2 and 3 are significantly altered when the boundary interacts with the void. When the boundary just touches the void, the boundary velocity increases to  $0.15 \mu\text{m/s}$  (The calculation of boundary velocity is described in Appendix C). This can be explained by the high boundary curvature formed near the void intersection resulting in an extra driving force for boundary migration. This high curvature is formed because the two segments of the boundary intersecting with the void have to be perpendicular to the void surface, which is consistent with the assumption in the Zener analysis of incoherent particles [185]. It is worth noting that this velocity is averaged over 500 time-steps, i.e. 1.15 s, and thus the instantaneous velocity could be higher. The interaction provides a driving force additional to the stored energy for boundary migration before the boundary pass through half of the void, after which it provides a dragging force. The velocity of point 3 is extremely high when the boundary just gets unpinned from the void, again because of the very large boundary curvature there. The velocity variations of the three points tend to become similar to that observed in the microstructure without the void (see Figure 5-12 a3) after the boundary has passed the void.

The average velocity of the whole recrystallizing grain boundary is also significantly influenced when passing the void (see Figure 5-12 (a3, b3, c3)). The void thus has a considerable effect on the kinetics of the whole boundary. In all cases, the void acts as an obstacle to the overall boundary migration. One interesting observation is that the position of the void relative to the inhomogeneous deformed microstructure also matters. This is clear when comparing the cases shown in Figure 5-12 (b, c): the boundary shape is different when the boundary interacts with the void due to the different deformed microstructure around the void. This result shows that the local microstructure around the void also affects the local as well as the global boundary kinetics during recrystallization.

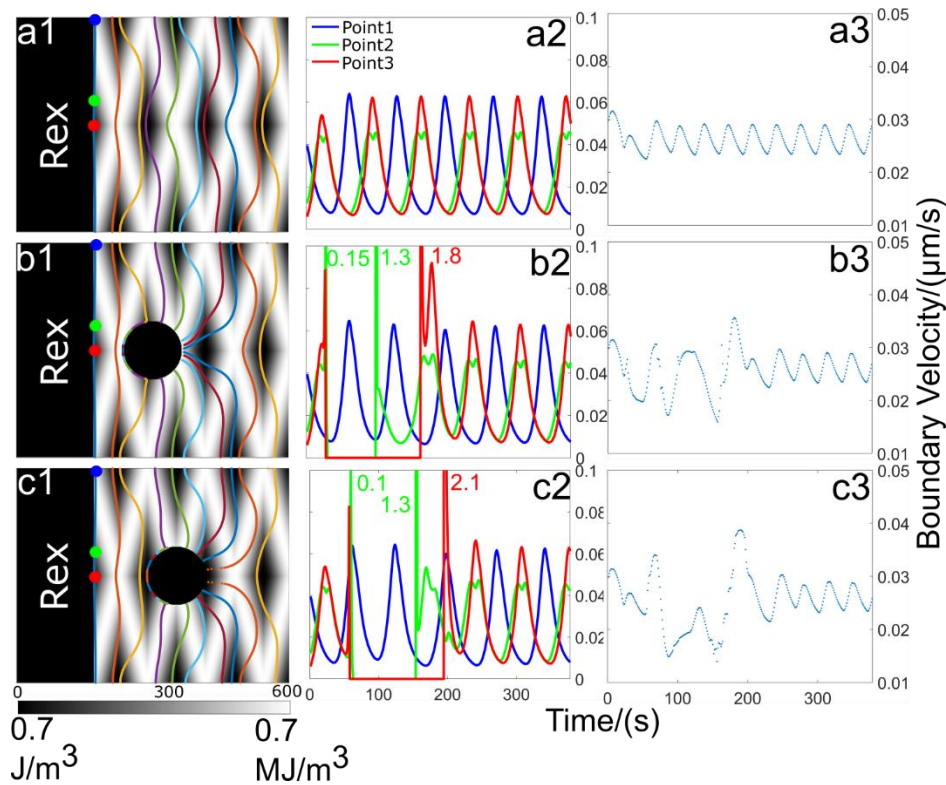


Figure 5-12 The kinetics of the recrystallizing grain boundary in the sine function defined microstructure (SM). (a1, b1, c1) Boundary characteristics for the three cases: without voids, with a void at position (300, 239) and (352, 239), respectively. The boundary traces are shown for every 10000 time steps (23.298s). (a2, b2, c2) Velocity variations of three grid points on the initial boundary (the peak values outside the display range are annotated). As shown in a1, b1 and c1, blue, green and red dots are denoted as point 1, point 2 and point 3, respectively. (a3, b3, c3) Velocity variations averaged over the whole boundary, corresponding to a1, b1 and c1, respectively.

The results for the cases with 3 recrystallized grains are shown in Figure 5-13. Due to the simulation set-up (the effective grain sizes of Rex1 and Rex3 are twice the illustrated size and thus larger than Rex2), Rex2 is observed to shrink with time and disappears at 740 s for the HM case without voids (1<sup>st</sup> row in Figure 5-13). If a void is present in the HM, (see 2<sup>nd</sup> row in Figure 5-13), the growth of Rex2 is limited due to the pinning effect from the void, and it takes longer time (about 1070 s) for Rex2 to disappear again due to the pinning effect from the void. A similar result is observed for the SM case (4<sup>th</sup> row in Figure 5-13), revealing the pinning effect of voids in recrystallization and grain growth. It is worth noting that grain growth is usually limited when recrystallization is still on-going [82]. The early grain growth observed here is due to the fact we are simulating the early stage of recrystallization, where the

nuclei sizes are very small (comparable to the sizes of voids and dislocation cells), and Rex2 cannot pass the void. This observation is important since voids are commonly observed in 3D printed samples with similar sizes as recrystallization nuclei.

In SM without voids (3<sup>rd</sup> row in Figure 5-13), Rex2 is also observed to shrink, but it happens quite early compared to the HM case. The reason is that the average stored energy in front of Rex2 is lowest, leading to the slow boundary migration of Rex2. Consequently, the two triple junctions migrate towards each other and Rex1 and Rex3 meet earlier. In addition, the boundary migrates faster in the HM than in the SM case. These results underline that the void and the inhomogeneous microstructure in combination play a significant role in determining the boundary kinetics during recrystallization.

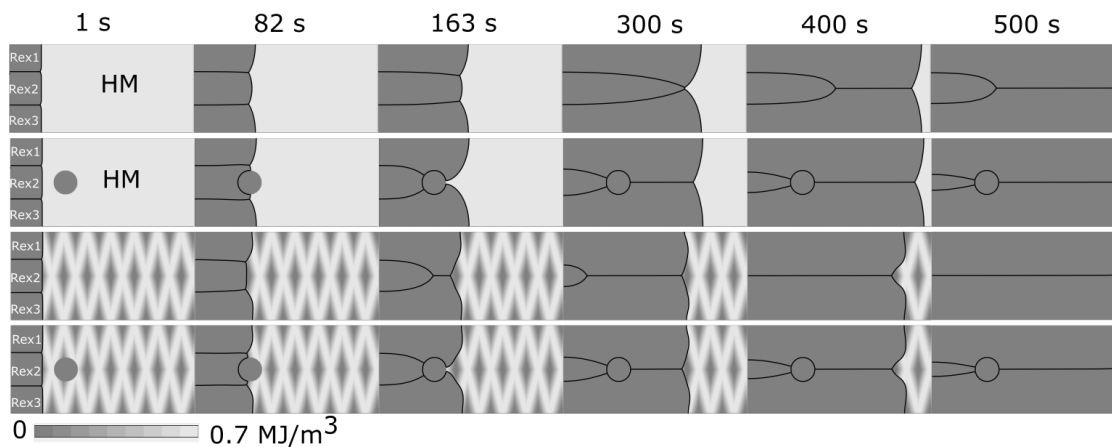


Figure 5-13 Comparison of boundary traces for the systems containing 3 recrystallization grains. For simplicity the deformation microstructures are not shown.

It is worth noting that in reality the deformed microstructure near the void may be different from that far away from the void due to less constraints near the void. To advance the present simulation, more inputs from experimental characterization and/or finite element modelling are needed. In this respect, it may be interesting to do a one-to-one experimental-simulation comparison, and thereby optimize the simulation parameters e.g. the boundary mobility, which remains a long-standing issue in recrystallization modelling.

The present study has considered the effects of both voids and inhomogeneous deformed microstructures on boundary migration during recrystallization. The void and the surrounding local microstructure are found to significantly alter the kinetics and shape of the boundary during recrystallization. The results also show that the

pinning effect of the void is strongest at the early stages of recrystallization when the nuclei and void sizes are comparable. The presented PF model with a void, is compatible with that containing incoherent second phase particles, so the present results are also valid for such systems.

### **Acknowledgements**

The authors gratefully acknowledge support from the European Research Council (ERC) under the European Union's Horizon 2020 research and innovation programme (grant agreement No.788567) for the M4D Advanced Grant within which this work is performed. CZ further acknowledges the financial support of the China Scholarship Council (CSC) (NO. 201706120026).

## Chapter 6: Conclusion and outlook

---

The objective of this thesis was to investigate the deformation and recrystallization behaviour of 3D printed stainless steel 316L samples. To facilitate a sound basis for understanding effects of the printing induced microstructures on the subsequent microstructural evolution, the data were compared to those obtained by a similar investigation of conventionally manufactured samples. The two initial conditions are referred to as P-0 and C-0, respectively. Both P-0 and C-0 samples were deformed by cold rolling, after which detailed microstructure characterization was carried out using electron microscopy (SEM/EBSD and TEM), X-ray diffraction and absorption contrast X-ray tomography. The P-0 and samples rolled to 30% reduction (P-30% and C-30%) were annealed to study recrystallization. Particularly, to understand the effects of voids in P-0 (and in P-30%) on the recrystallization boundary migration, a phase field model was modified to allow for voids to be included, and simulations and ex-situ SEM/EBSD observations were performed. The mechanical properties were characterized by hardness measurement and tensile testing. The main conclusions of the present study and suggestions for future work are as follows:

The microstructural evolution during cold rolling of the conventionally manufactured 316L can be briefly summarized as: a Taylor lattice structure is formed at small strains; deformation twins/twin-matrix lamellae form at medium strains; micro shear banding and martensite transformation (mainly in shear bands) occur at high strains. An orientation dependence of deformation twinning is found: deformation twinning occurs preferentially in grains with near Copper orientation rather than Brass orientation. The deformation twinning transforms the Copper orientation to the twin Copper orientation, and therefore contributes to the elimination of Copper orientation with increasing rolling reduction. A texture transition from the Copper to the Brass type occurs at medium strains and is suggested to be related to the deformation

twinning and micro shear banding, which are observed to develop at a strain coinciding with the onset of the texture transition.

The cellular/columnar structure, which is a result of the printing process, contributes to the higher strength of P-0 than C-0. The detailed observations of the microstructural evolution during cold rolling of the printed samples, and the comparison with that in the conventionally manufactured samples, shows that the cellular/columnar dislocation boundaries act as a weak obstacle to dislocation motion and deformation twinning. Furthermore, they facilitate the formation of multiple sets of deformation twins and the formation of a dislocation cell structure—not observed in conventionally manufactured samples. In addition, the deformation twins in the printed samples are found to be thinner than that in conventionally manufactured samples. The initial cellular/columnar boundaries, induced by the printing, are thus suggested to pivot dislocation multiplication and deformation twinning as well as their interaction. This explains the higher yield strength and less elongation to failure of P-30% and C-30%.

Recrystallization is not obvious in P-0 at the chosen annealing conditions, but when cold rolling is added recrystallization is observed. P-30% recrystallizes earlier and progresses at a faster rate than C-30%, which agrees well with the additional printing induced stored energy. Tensile test shows a decrease in both strength and ductility of P-0 after annealing at 850 °C for 1 h. This suggests that the characteristic of cellular/columnar boundaries and the dislocations inside the cellular structure may change, affecting deformation behaviours such as dislocation multiplication and motion, nucleation and growth of deformation twinning as well as their interaction.

Voids appear to be unavoidable in 3D printed samples, even when the printing parameters are carefully controlled and optimized. In the P-0 sample characterized in this work, large keyhole voids tend to form in volumes near the sample surface while small gas entrapped voids tend to form at the centre of the printed samples. Lack of fusion voids are rarely observed, indicating that the applied printing parameters are suitable.

Effects of voids on the boundary kinetics during recrystallization was analysed by both ex-situ SEM/EBSD characterization and phase field simulations. A modification was made to the existent phase field model: A void is included into the simulation system by including a new order parameter into the equation. A few idealized cases concerning the deformed microstructure, the position of the void in the deformed

microstructure and the number of recrystallizing grains, were simulated. It is found that both voids and the deformed/printed microstructure can significantly affect the local boundary kinetics and the effect is especially strong at the early stage of recrystallization.

The present study indicates that there is significant potential in optimizing the microstructure (cellular/columnar boundaries) of 3D printed samples by post-printing thermomechanical treatments. Furthermore, it is found that mechanical and thermal loads, which a printed part may be exposed to during its use in practical applications, will change the microstructure and thus the properties of the part. In order to predict the performance, it is thus of critical importance to consider such changes.

In outlook, it is suggested to extend the present work with the aim of understanding the physical relationship between cellular/columnar dislocation boundaries including the elemental segregation (which may affect the local SFE) and deformation mechanism. This work will not only provide an understanding of boundary dynamics in 3D printed samples but also make it possible to obtain new microstructures that lead to better mechanical and corrosion properties by controlling the distributions of dislocations, dislocation boundaries, solutes and precipitates. Although there is no recrystallization observed in P-0 at the chosen annealing temperature, it is of interest to investigate the annealing kinetics of P-0 at higher temperatures, its relationship with printing parameters and the resultant microstructure. In addition, from the simulation perspective, there is a necessity for future work to perform a one-on-one comparison between phase field simulations and experiments (in both 2D and 3D) to validate the phase field model and provide novel insights into recrystallization, e.g. to deduce reliable values for grain boundary mobilities.

# Bibliography

---

- [1] W.E. Frazier, Metal additive manufacturing: A review, *J. Mater. Eng. Perform.* 23 (2014) 1917–1928.
- [2] E. MacDonald, R. Wicker, Multiprocess 3D printing for increasing component functionality, *Science*. 353 (2016) aaf2093.
- [3] J.J. Lewandowski, M. Seifi, Metal Additive Manufacturing: A Review of Mechanical Properties, *Annu. Rev. Mater. Res.* 46 (2016) 151–186.
- [4] Z. Chen, Z. Li, J. Li, C. Liu, C. Lao, Y. Fu, C. Liu, Y. Li, P. Wang, Y. He, 3D printing of ceramics: A review, *J. Eur. Ceram. Soc.* 39 (2019) 661–687.
- [5] N.T. Aboulkhair, M. Simonelli, L. Parry, I. Ashcroft, C. Tuck, R. Hague, 3D printing of Aluminium alloys: Additive Manufacturing of Aluminium alloys using selective laser melting, *Prog. Mater. Sci.* 106 (2019) 100578.
- [6] H. Wu, W.P. Fahy, S. Kim, H. Kim, N. Zhao, L. Pilato, A. Kafi, S. Bateman, J.H. Koo, Recent developments in polymers/polymer nanocomposites for additive manufacturing, *Prog. Mater. Sci.* 111 (2020) 100638.
- [7] M. Tarik Hasib, H.E. Ostergaard, X. Li, J.J. Kruzic, Fatigue crack growth behavior of laser powder bed fusion additive manufactured Ti-6Al-4V: Roles of post heat treatment and build orientation, *Int. J. Fatigue*. 142 (2021) 105955.
- [8] D. Banerjee, J.C. Williams, Perspectives on Titanium Science and Technology, *Acta Mater.* 61 (2013) 844–879.
- [9] Y. Zhong, L. Liu, S. Wikman, D. Cui, Z. Shen, Intragranular cellular segregation network structure strengthening 316L stainless steel prepared by selective laser melting, *J. Nucl. Mater.* 470 (2016) 170–178.
- [10] M.M. Dewidar, K.A. Khalil, J.K. Lim, Processing and mechanical properties of porous 316L stainless steel for biomedical applications, *Trans. Nonferrous Met.*

Soc. China. 17 (2007) 468–473.

- [11] U.I. Thomann, P.J. Uggowitzer, Wear-corrosion behavior of biocompatible austenitic stainless steels, *Wear*. 239 (2000) 48–58.
- [12] B. AlMangour, D. Grzesiak, J.M. Yang, In-situ formation of novel TiC-particle-reinforced 316L stainless steel bulk-form composites by selective laser melting, *J. Alloys Compd.* 706 (2017) 409–418.
- [13] L. Thijs, F. Verhaeghe, T. Craeghs, J. Van Humbeeck, J.P. Kruth, A study of the microstructural evolution during selective laser melting of Ti–6Al–4V, *Acta Mater.* 58 (2010) 3303–3312.
- [14] T. Ishimoto, K. Hagihara, K. Hisamoto, S.H. Sun, T. Nakano, Crystallographic texture control of beta-type Ti–15Mo–5Zr–3Al alloy by selective laser melting for the development of novel implants with a biocompatible low Young’s modulus, *Scr. Mater.* 132 (2017) 34–38.
- [15] S. Bahl, S. Mishra, K.U.U. Yazar, I.R. Kola, K. Chatterjee, S. Suwas, Non-equilibrium microstructure, crystallographic texture and morphological texture synergistically result in unusual mechanical properties of 3D printed 316L stainless steel, *Addit. Manuf.* 28 (2019) 65–77.
- [16] H. Choo, K.L. Sham, J. Bohling, A. Ngo, X. Xiao, Y. Ren, P.J. Depond, M.J. Matthews, E. Garlea, Effect of laser power on defect, texture, and microstructure of a laser powder bed fusion processed 316L stainless steel, *Mater. Des.* 164 (2019) 107534.
- [17] D. Kong, X. Ni, C. Dong, X. Lei, L. Zhang, C. Man, J. Yao, X. Cheng, X. Li, Bio-functional and anti-corrosive 3D printing 316L stainless steel fabricated by selective laser melting, *Mater. Des.* 152 (2018) 88–101.
- [18] J.H.K. Tan, S.L. Sing, W.Y. Yeong, Microstructure modelling for metallic additive manufacturing: a review, *Virtual Phys. Prototyp.* 15 (2020) 87–105.
- [19] T. Niendorf, S. Leuders, A. Riemer, H.A. Richard, T. Tröster, D. Schwarze, Highly anisotropic steel processed by selective laser melting, *Metall. Mater. Trans. B Process Metall. Mater. Process. Sci.* 44 (2013) 794–796.
- [20] Y.M. Wang, T. Voisin, J.T. McKeown, J. Ye, N.P. Calta, Z. Li, Z. Zeng, Y. Zhang, W. Chen, T.T. Roehling, R.T. Ott, M.K. Santala, P.J. Depond, M.J.

- Matthews, A. V. Hamza, T. Zhu, Additively manufactured hierarchical stainless steels with high strength and ductility, *Nat. Mater.* 17 (2018) 63–70.
- [21] K. Saeidi, X. Gao, Y. Zhong, Z.J. Shen, Hardened austenite steel with columnar sub-grain structure formed by laser melting, *Mater. Sci. Eng. A.* 625 (2015) 221–229.
- [22] A.J. Birnbaum, J.C. Steuben, E.J. Barrick, A.P. Iliopoulos, J.G. Michopoulos, Intrinsic strain aging,  $\Sigma 3$  boundaries, and origins of cellular substructure in additively manufactured 316L, *Addit. Manuf.* 29 (2019) 100784.
- [23] S. Gorsse, C. Hutchinson, M. Gouné, R. Banerjee, Additive manufacturing of metals: a brief review of the characteristic microstructures and properties of steels, Ti-6Al-4V and high-entropy alloys, *Sci. Technol. Adv. Mater.* 18 (2017) 584–610.
- [24] L. Liu, Q. Ding, Y. Zhong, J. Zou, J. Wu, Y.-L. Chiu, J. Li, Z. Zhang, Q. Yu, Z. Shen, Dislocation network in additive manufactured steel breaks strength–ductility trade-off, *Mater. Today.* 21 (2018) 354–361.
- [25] K.M. Bertsch, G. Meric de Bellefon, B. Kuehl, D.J. Thoma, Origin of dislocation structures in an additively manufactured austenitic stainless steel 316L, *Acta Mater.* 199 (2020) 19–33.
- [26] A. Basak, S. Das, Epitaxy and Microstructure Evolution in Metal Additive Manufacturing, *Annu. Rev. Mater. Res.* 46 (2016) 125–149.
- [27] L. Cui, D. Deng, F. Jiang, R.L. Peng, T. Xin, R.T. Mousavian, Z. Yang, J. Moverare, Superior low cycle fatigue property from cell structures in additively manufactured 316L stainless steel, *J. Mater. Sci. Technol.* 111 (2022) 268–278.
- [28] Robert W. Messler Jr., Weld Fusion Zone Solidification, in: *Princ. Weld.*, John Wiley & Sons, Ltd, 1999: pp. 373–453.
- [29] S.A. Khairallah, A.T. Anderson, A. Rubenchik, W.E. King, Laser powder-bed fusion additive manufacturing: Physics of complex melt flow and formation mechanisms of pores, spatter, and denudation zones, *Acta Mater.* 108 (2016) 36–45.
- [30] J. V. Gordon, S.P. Narra, R.W. Cunningham, H. Liu, H. Chen, R.M. Suter, J.L. Beuth, A.D. Rollett, Defect structure process maps for laser powder bed fusion

- additive manufacturing, *Addit. Manuf.* 36 (2020) 101552.
- [31] M. Tang, P.C. Pistorius, Oxides, porosity and fatigue performance of AlSi10Mg parts produced by selective laser melting, *Int. J. Fatigue.* 94 (2017) 192–201.
- [32] L.E. Scriven, C. V. Sternling, The Marangoni Effects, *Nature.* 187 (1960) 186–188.
- [33] R. Cunningham, C. Zhao, N. Parab, C. Kantzos, J. Pauza, K. Fezzaa, T. Sun, A.D. Rollett, Keyhole threshold and morphology in laser melting revealed by ultrahigh-speed x-ray imaging, *Science.* 363 (2019) 849–852.
- [34] J.P. Kruth, L. Froyen, J. Van Vaerenbergh, P. Mercelis, M. Rombouts, B. Lauwers, Selective laser melting of iron-based powder, *J. Mater. Process. Technol.* 149 (2004) 616–622.
- [35] J.A. Choren, S.M. Heinrich, M.B. Silver-Thorn, Young's modulus and volume porosity relationships for additive manufacturing applications, *J. Mater. Sci.* 48 (2013) 5103–5112.
- [36] G. Sander, J. Tan, P. Balan, O. Gharbi, D.R. Feenstra, L. Singer, S. Thomas, R.G. Kelly, J.R. Scully, N. Birbilis, Corrosion of Additively Manufactured Alloys: A Review, *Corrosion.* 74 (2018) 1318–1350.
- [37] R.W. Fonda, D.J. Rowenhorst, C.R. Feng, A.J. Levinson, K.E. Knippling, S. Olig, A. Ntiros, B. Stiles, R. Rayne, The Effects of Post-processing in Additively Manufactured 316L Stainless Steels, *Metall. Mater. Trans. A Phys. Metall. Mater. Sci.* 51 (2020) 6560–6573.
- [38] P. Bian, J. Shi, Y. Liu, Y. Xie, Influence of laser power and scanning strategy on residual stress distribution in additively manufactured 316L steel, *Opt. Laser Technol.* 132 (2020) 106477.
- [39] Q. Chao, S. Thomas, N. Birbilis, P. Cizek, P.D. Hodgson, D. Fabijanic, The effect of post-processing heat treatment on the microstructure, residual stress and mechanical properties of selective laser melted 316L stainless steel, *Mater. Sci. Eng. A.* 821 (2021) 141611.
- [40] O. Takakuwa, H. Soyama, Effect of Residual Stress on the Corrosion Behavior of Austenitic Stainless Steel, *Adv. Chem. Eng. Sci.* 05 (2015) 62–71.

- [41] G. Van Boven, W. Chen, R. Rogge, The role of residual stress in neutral pH stress corrosion cracking of pipeline steels. Part I: Pitting and cracking occurrence, *Acta Mater.* 55 (2007) 29–42.
- [42] X. Luo, Z. Feng, T. Yu, J. Luo, T. Huang, G. Wu, N. Hansen, X. Huang, Transitions in mechanical behavior and in deformation mechanisms enhance the strength and ductility of Mg-3Gd, *Acta Mater.* 183 (2020) 398–407.
- [43] N. Hansen, Polycrystalline strengthening, *Metall. Trans. A.* 16 (1985) 2167–2190.
- [44] N. Hansen, D.J. Jensen, Development of microstructure in FCC metals during cold work, *Philos. Trans. R. Soc. London. Ser. A Math. Phys. Eng. Sci.* 357 (1999) 1447–1469.
- [45] G. Winther, X. Huang, Dislocation structures. Part II. Slip system dependence, *Philos. Mag.* 87 (2007) 5215–5235.
- [46] X. Huang, G. Winther, Dislocation structures. Part I. Grain orientation dependence, *Philos. Mag.* 87 (2007) 5189–5214.
- [47] X.Z. Liao, F. Zhou, E.J. Lavernia, S.G. Srinivasan, M.I. Baskes, D.W. He, Y.T. Zhu, Deformation mechanism in nanocrystalline Al: Partial dislocation slip, *Appl. Phys. Lett.* 83 (2003) 632.
- [48] Q. Liu, D. Juul Jensen, N. Hansen, Effect of grain orientation on deformation structure in cold-rolled polycrystalline aluminium, *Acta Mater.* 46 (1998) 5819–5838.
- [49] Q. Liu, X. Huang, D.J. Lloyd, N. Hansen, Microstructure and strength of commercial purity aluminium (AA 1200) cold-rolled to large strains, *Acta Mater.* 50 (2002) 3789–3802.
- [50] D.A. Hughes, N. Hansen, Microstructural evolution in nickel during rolling from intermediate to large strains, *Metall. Trans. A.* 24 (1993) 2022–2037.
- [51] S. Curtze, V.T. Kuokkala, A. Oikari, J. Talonen, H. Hänninen, Thermodynamic modeling of the stacking fault energy of austenitic steels, *Acta Mater.* 59 (2011) 1068–1076.
- [52] G. Wassermann, Der Einfluß mechanischer Zwillingsbildung auf die

Entstehung der Walztexturen kubisch Flächenzentrierter Metalle, *Int. J. Mater. Res.* 54 (1963) 61–65.

- [53] J. Hirsch, K. Lücke, Overview no. 76. Mechanism of deformation and development of rolling textures in polycrystalline f.c.c. metals-II. Simulation and interpretation of experiments on the basis of Taylor-type theories, *Acta Metall.* 36 (1988) 2883–2904.
- [54] T. Leffers, R.K. Ray, The brass-type texture and its deviation from the copper-type texture, *Prog. Mater. Sci.* 54 (2009) 351–396.
- [55] E. El-Danaf, S.R. Kalidindi, R.D. Doherty, C. Necker, Deformation texture transition in brass: critical role of micro-scale shear bands, *Acta Mater.* 48 (2000) 2665–2673.
- [56] C. Donadille, R. Valle, P. Dervin, R. Penelle, Development of texture and microstructure during cold-rolling and annealing of F.C.C. alloys: Example of an austenitic stainless steel, *Acta Metall.* 37 (1989) 1547–1571.
- [57] S. Hashmi, *Comprehensive Materials Processing*, 2014.
- [58] F.K. Yan, N.R. Tao, K. Lu, Tensile ductility of nanotwinned austenitic grains in an austenitic steel, *Scr. Mater.* 84–85 (2014) 31–34.
- [59] J. Li, Y. Cao, B. Gao, Y. Li, Y. Zhu, Superior strength and ductility of 316L stainless steel with heterogeneous lamella structure, *J. Mater. Sci.* 53 (2018) 10442–10456.
- [60] M. Odnobokova, A. Belyakov, R. Kaibyshev, Effect of Severe Cold or Warm Deformation on Microstructure Evolution and Tensile Behavior of a 316L Stainless Steel, *Adv. Eng. Mater.* 17 (2015) 1812–1820.
- [61] I. Shakhova, V. Dudko, A. Belyakov, K. Tsuzaki, R. Kaibyshev, Effect of large strain cold rolling and subsequent annealing on microstructure and mechanical properties of an austenitic stainless steel, *Mater. Sci. Eng. A.* 545 (2012) 176–186.
- [62] T.S. Byun, E.H. Lee, J.D. Hunn, Plastic deformation in 316LN stainless steel - Characterization of deformation microstructures, *J. Nucl. Mater.* 321 (2003) 29–39.

- [63] M. Naghizadeh, H. Mirzadeh, Microstructural Evolutions During Reversion Annealing of Cold-Rolled AISI 316 Austenitic Stainless Steel, *Metall. Mater. Trans. A Phys. Metall. Mater. Sci.* 49 (2018) 2248–2256.
- [64] L. Remy, Kinetics of f.c.c. deformation twinning and its relationship to stress-strain behaviour, *Acta Metall.* 26 (1978) 443–451.
- [65] Y.F. Shen, X.X. Li, X. Sun, Y.D. Wang, L. Zuo, Twinning and martensite in a 304 austenitic stainless steel, *Mater. Sci. Eng. A.* 552 (2012) 514–522.
- [66] M.J. Sohrabi, M. Naghizadeh, H. Mirzadeh, Deformation-induced martensite in austenitic stainless steels: A review, *Arch. Civ. Mech. Eng.* 2020 204. 20 (2020) 1–24.
- [67] F.D. Fischer, G. Reisner, E. Werner, K. Tanaka, G. Cailletaud, T. Antretter, New view on transformation induced plasticity (TRIP), *Int. J. Plast.* 16 (2000) 723–748.
- [68] D. Kuhlmann-Wilsdorf, N. Hansen, Geometrically necessary, incidental and subgrain boundaries, *Scr. Metall. Mater.* 25 (1991) 1557–1562.
- [69] M. Moneghan, C. Williams, R. Mirzaeifar, Deformation mechanisms and defect tolerance in the microstructure of 3D-printed alloys, *J. Mater. Res.* 35 (2020) 1984–1997.
- [70] D. Raabe, D. Ponge, O. Dmitrieva, B. Sander, Designing ultrahigh strength steels with good ductility by combining transformation induced plasticity and martensite aging, *Adv. Eng. Mater.* 11 (2009) 547–555.
- [71] Z. Sun, X. Tan, C. Wang, M. Descoins, D. Mangelinck, S.B. Tor, E.A. Jäggle, S. Zaefferer, D. Raabe, Reducing hot tearing by grain boundary segregation engineering in additive manufacturing: example of an Al<sub>x</sub>CoCrFeNi high-entropy alloy, *Acta Mater.* 204 (2021) 116505.
- [72] F.J. Humphreys, M. Hatherly, *Recrystallization and related annealing phenomena*, Elsevier, 2012.
- [73] P.A. Beck, P.R. Sperry, Strain Induced Grain Boundary Migration in High Purity Aluminum, *J. Appl. Phys.* 21 (2004) 150.
- [74] P.B.H. J.E. Bailey, *The recrystallization process in some polycrystalline metals*,

- Proc. R. Soc. London. Ser. A. Math. Phys. Sci. 267 (1962) 11–30.
- [75] R.W. Cahn, A New Theory of Recrystallization Nuclei, Proc. Phys. Soc. Sect. A. 63 (1950) 323.
- [76] A.H. Cottrell, Theory of dislocations, Prog. Met. Phys. 4 (1953) 205–264.
- [77] H. Hu, Direct observations on annealing of a si-fe crystal in electron microscope, Trans. Metall. Soc. AIME. 224 (1962) 75.
- [78] J.C. M Li, J.C. M Lr Edgar C, Possibility of Subgrain Rotation during Recrystallization, J. Appl. Phys. 33 (2004) 2958.
- [79] J.W. Cahn, Y. Mishin, A. Suzuki, Coupling grain boundary motion to shear deformation, Acta Mater. 54 (2006) 4953–4975.
- [80] Y. Zhang, A. Godfrey, D.J. Jensen, Local boundary migration during recrystallization in pure aluminium, Scr. Mater. 64 (2011) 331–334.
- [81] N. Moelans, A. Godfrey, Y. Zhang, D. Juul Jensen, Phase-field simulation study of the migration of recrystallization boundaries, Phys. Rev. B. 88 (2013) 54103.
- [82] M.F. Ashby, Recrystallization and grain growth of multi-phase and particle containing materials, in: 1st Risø Int. Symp., N. Hansen, A.R. Jones, T. Leffers, eds., Risø National Laboratory, Roskilde, Denmark, 1980, pp. 325..
- [83] S. Sreekala, M. Haataja, Recrystallization kinetics: A coupled coarse-grained dislocation density and phase-field approach, Phys. Rev. B - Condens. Matter Mater. Phys. 76 (2007) 094109.
- [84] R.B. Godiksen, Z.T. Trautt, M. Upmanyu, J. Schiøtz, D.J. Jensen, S. Schmidt, Simulations of boundary migration during recrystallization using molecular dynamics, Acta Mater. 55 (2007) 6383–6391.
- [85] V. Yadav, N. Moelans, Y. Zhang, D. Juul Jensen, Influence of geometrical alignment of the deformation microstructure on local migration of grain boundaries during recrystallization: A phase-field study, Scr. Mater. 191 (2021) 116–119.
- [86] P.A. Manohar, M. Ferry, T. Chandra, Five Decades of the Zener Equation, ISIJ Int. 38 (1998) 913–924.
- [87] E.A. Holm, C.C. Battaile, The computer simulation of microstructural

- evolution, *JOM* 2000 539. 53 (2001) 20–23.
- [88] V. Mohles, 3-D front tracking model for interfaces with anisotropic energy, *Comput. Mater. Sci.* 176 (2020) 109534.
- [89] M.P. Anderson, D.J. Srolovitz, G.S. Grest, P.S. Sahni, Computer simulation of grain growth—I. Kinetics, *Acta Metall.* 32 (1984) 783–791.
- [90] B. Scholtes, M. Shakoor, A. Settefrati, P.O. Bouchard, N. Bozzolo, M. Bernacki, New finite element developments for the full field modeling of microstructural evolutions using the level-set method, *Comput. Mater. Sci.* 109 (2015) 388–398.
- [91] A.D. Rollett, D.J. Srolovitz, M.P. Anderson, R.D. Doherty, Computer simulation of recrystallization—III. Influence of a dispersion of fine particles, *Acta Metall. Mater.* 40 (1992) 3475–3495.
- [92] D. Weygand, Y. Bréchet, J. Lépinoux, Zener pinning and grain growth: a two-dimensional vertex computer simulation, *Acta Mater.* 47 (1999) 961–970.
- [93] D. Raabe, Cellular automata in materials science with particular reference to recrystallization simulation, *Annu. Rev. Mater. Sci.* 32 (2002) 53–76.
- [94] F.J. Humphreys, The nucleation of recrystallization at second phase particles in deformed aluminium, *Acta Metall.* 25 (1977) 1323–1344.
- [95] D.A. Molodov, U. Czubayko, G. Gottstein, L.S. Shvindlerman, On the effect of purity and orientation on grain boundary motion, *Acta Mater.* 46 (1998) 553–564.
- [96] M.L. Taheri, D. Molodov, G. Gottstein, A.D. Rollett, Grain boundary mobility under a stored-energy driving force: A comparison to curvature-driven boundary migration, *Zeitschrift Fuer Met. Res. Adv. Tech.* 96 (2005) 1166–1170.
- [97] K. Chen, J. Han, D.J. Srolovitz, On the temperature dependence of grain boundary mobility, *Acta Mater.* 194 (2020) 412–421.
- [98] M.I. Mendeleev, D.J. Srolovitz, Grain-boundary migration in the presence of diffusing impurities: Simulations and analytical models, *Philos. Mag. A Phys. Condens. Matter, Struct. Defects Mech. Prop.* 81 (2001) 2243–2269.

- [99] E.R. Homer, E.A. Holm, S.M. Foiles, D.L. Olmsted, Trends in grain boundary mobility: Survey of motion mechanisms, *JOM*. 66 (2014) 114–120.
- [100] B. Schönfelder, G. Gottstein, L.S. Shvindlerman, Comparative study of grain-boundary migration and grain-boundary self-diffusion of [0 0 1] twist-grain boundaries in copper by atomistic simulations, *Acta Mater.* 53 (2005) 1597–1609.
- [101] K.G.F. Janssens, D. Olmsted, E.A. Holm, S.M. Foiles, S.J. Plimpton, P.M. Derlet, Computing the mobility of grain boundaries, *Nat. Mater.* 2006 52. 5 (2006) 124–127.
- [102] K. Chen, J. Han, X. Pan, D.J. Srolovitz, The grain boundary mobility tensor, *Proc. Natl. Acad. Sci. U. S. A.* 117 (2020) 4533–4538.
- [103] S. Schmidt, S.F. Nielsen, C. Gundlach, L. Margulies, X. Huang, D.J. Jensen, Watching the growth of bulk grains during recrystallization of deformed metals." *Science*, 305.5681 (2004): 229-232.
- [104] W.J. Boettinger, J.A. Warren, C. Beckermann, A. Karma, Phase-field simulation of solidification, *Annu. Rev. Mater. Sci.* 32 (2002) 163–194.
- [105] L.Q. Chen, Phase-field models for microstructure evolution, *Annu. Rev. Mater. Sci.* 32 (2002) 113–140.
- [106] L.Q. Chen, Y. Wang, The continuum field approach to modeling microstructural evolution, *JOM*. 48 (1996) 13–18.
- [107] D. Tournet, H. Liu, J. LLorca, Phase-field modeling of microstructure evolution: Recent applications, perspectives and challenges, *Prog. Mater. Sci.* 123 (2022) 100810.
- [108] N. Moelans, B. Blanpain, P. Wollants, A phase field model for the simulation of grain growth in materials containing finely dispersed incoherent second-phase particles, *Acta Mater.* 53 (2005) 1771–1781.
- [109] G.N. Hassold, E.A. Holm, D.J. Srolovitz, Effects of particle size on inhibited grain growth, *Scr. Metall. Mater.* 24 (1990) 101–106.
- [110] L. Zhang, Y. Shibuta, C. Lu, X. Huang, Interaction between nano-voids and migrating grain boundary by molecular dynamics simulation, *Acta Mater.* 173

- (2019) 206–224.
- [111] J. Zhang, W. Ludwig, Y. Zhang, H.H.B. Sørensen, D.J. Rowenhorst, A. Yamanaka, P.W. Voorhees, H.F. Poulsen, Grain boundary mobilities in polycrystals, *Acta Mater.* 191 (2020) 211–220.
- [112] R. Li, V. Yadav, N. Moelans, Y. Zhang, D. Juul Jensen, A phase-field investigation of recrystallization boundary migration into heterogeneous deformation energy fields: Effects of dislocation boundary sharpness, *IOP Conf. Ser. Mater. Sci. Eng.* 1121 (2021) 012013.
- [113] Y.B. Zhang, J.D. Budai, J.Z. Tischler, W. Liu, R. Xu, E.R. Homer, A. Godfrey, D. Juul Jensen, Boundary migration in a 3D deformed microstructure inside an opaque sample, *Sci. Reports* 2017 71. 7 (2017) 1–8.
- [114] N. Moelans, B. Blanpain, P. Wollants, Quantitative analysis of grain boundary properties in a generalized phase field model for grain growth in anisotropic systems, *Phys. Rev. B - Condens. Matter Mater. Phys.* 78 (2008).
- [115] L.Q. Chen, W. Yang, Computer simulation of the domain dynamics of a quenched system with a large number of nonconserved order parameters: The grain-growth kinetics, *Phys. Rev. B.* 50 (1994) 15752–15756.
- [116] S. Kikuchi, Diffraction of Cathode Rays by Mica, *Proc. Imp. Acad.* 4 (1928) 271–274.
- [117] F.J. Humphreys, Characterisation of fine-scale microstructures by electron backscatter diffraction (EBSD), *Scr. Mater.* 51 (2004) 771–776.
- [118] A. Winkelmann, Principles of depth-resolved Kikuchi pattern simulation for electron backscatter diffraction, *J. Microsc.* 239 (2010) 32–45.
- [119] F. Bachmann, R. Hielscher, H. Schaeben, Texture Analysis with MTEX – Free and Open Source Software Toolbox, *Solid State Phenom.* 160 (2010) 63–68.
- [120] G. Christiansen, J.R. Bowen, J. Lindbo, Electrolytic preparation of metallic thin foils with large electron-transparent regions, *Mater. Charact.* 49 (2002) 331–335.
- [121] F.J. Humphreys, Grain and subgrain characterisation by electron backscatter diffraction, *J. Mater. Sci.* 36 (2001) 3833–3854.

- [122] H.-J. Bunge, *Texture analysis in materials science: mathematical methods*, Elsevier, 2013.
- [123] B. Weiss, Stickler R, Phase instabilities during high temperature exposure of 316 austenitic stainless steel, *Met Trans.* 3 (1972) 851–866.
- [124] Y. Xiong, Y. Yue, Y. Lu, T. He, M. Fan, F. Ren, W. Cao, Cryorolling impacts on microstructure and mechanical properties of AISI 316 LN austenitic stainless steel, *Mater. Sci. Eng. A.* 709 (2018) 270–276.
- [125] S. Kheiri, H. Mirzadeh, M. Naghizadeh, Tailoring the microstructure and mechanical properties of AISI 316L austenitic stainless steel via cold rolling and reversion annealing, *Mater. Sci. Eng. A.* 759 (2019) 90–96.
- [126] T. Leffers, Microstructures and mechanisms of polycrystal deformation at low temperature, in: 2nd Risø Int. Symp., N.Hansen, A. Horsewell, T. Leffers, H. Lilholt (Eds.), on *Deformation of Polycrystals: Mechanisms and Microstructure*, Risø National Laboratory, Roskilde, Denmark, 1981: pp. 55–71.
- [127] D. Juul Jensen, A.W. Thompson, N. Hansen, The role of grain size and strain in work hardening and texture development, *Metall. Trans. A.* 20 (1989) 2803–2810.
- [128] J. Hirsch, K. Lücke, M. Hatherly, Overview No. 76: Mechanism of deformation and development of rolling textures in polycrystalline f.c.c. Metals—III. The influence of slip inhomogeneities and twinning, *Acta Metall.* 36 (1988) 2905–2927.
- [129] Q. Liu, C. Maurice, J. Driver, N. Hansen, Heterogeneous Microstructures and Microtextures in CubeOriented Al crystals after channel die compression, *Metall. Mater. Trans. A Phys. Metall. Mater. Sci.* 29 (1998) 2333–2344.
- [130] W.Q. Cao, A. Godfrey, Q. Liu, EBSD investigation of microstructure and texture evolution during equal channel angular pressing of aluminium, *Mater. Sci. Eng. A.* 361 (2003) 9–14.
- [131] J. Gil Sevillano, P. van Houtte, E. Aernoudt, Large strain work hardening and textures, *Prog. Mater. Sci.* 25 (1980) 69–134.
- [132] S. Roy, D. Satyaveer Singh, S. Suwas, S. Kumar, K. Chattopadhyay,

- Microstructure and texture evolution during accumulative roll bonding of aluminium alloy AA5086, *Mater. Sci. Eng. A.* 528 (2011) 8469–8478.
- [133] D. Barbier, N. Gey, S. Allain, N. Bozzolo, M. Humbert, Analysis of the tensile behavior of a TWIP steel based on the texture and microstructure evolutions, *Mater. Sci. Eng. A.* 500 (2009) 196–206.
- [134] L. Bracke, K. Verbeken, L. Kestens, J. Penning, Microstructure and texture evolution during cold rolling and annealing of a high Mn TWIP steel, *Acta Mater.* 57 (2009) 1512–1524.
- [135] E. Jimenez-Melero, N.H. van Dijk, L. Zhao, J. Sietsma, J.P. Wright, S. van der Zwaag, In situ synchrotron study on the interplay between martensite formation, texture evolution and load partitioning in low-alloyed TRIP steels, *Mater. Sci. Eng. A.* 528 (2011) 6407–6416.
- [136] S. Vercammen, B. Blanpain, B.C. De Cooman, P. Wollants, Cold rolling behaviour of an austenitic Fe-30Mn-3Al-3Si TWIP-steel: The importance of deformation twinning, *Acta Mater.* 52 (2004) 2005–2012.
- [137] S.G. Chowdhury, S. Das, P.K. De, Cold rolling behaviour and textural evolution in AISI 316L austenitic stainless steel, *Acta Mater.* 53 (2005) 3951–3959.
- [138] M. Odnobokova, A. Belyakov, N. Enikeev, D.A. Molodov, R. Kaibyshev, Annealing behavior of a 304L stainless steel processed by large strain cold and warm rolling, *Mater. Sci. Eng. A.* 689 (2017) 370–383.
- [139] D.A. Hughes, N. Hansen, Microstructural evolution in nickel during rolling from intermediate to large strains, *Metall. Trans. A.* 24 (1993) 2022–2037.
- [140] G. Kurdjumow, G. Sachs, Der Mechanismus der Stahlhärtung, *Z. Phys.* 18 (1930) p 534.
- [141] D. Molnár, X. Sun, S. Lu, W. Li, G. Engberg, L. Vitos, Effect of temperature on the stacking fault energy and deformation behaviour in 316L austenitic stainless steel, *Mater. Sci. Eng. A.* 759 (2019) 490–497.
- [142] G. Monnet, M.A. Pouchon, Determination of the critical resolved shear stress and the friction stress in austenitic stainless steels by compression of pillars extracted from single grains, *Mater. Lett.* 98 (2013) 128–130.

- [143] J.T. Busby, M.C. Hash, G.S. Was, The relationship between hardness and yield stress in irradiated austenitic and ferritic steels, *J. Nucl. Mater.* 336 (2005) 267–278.
- [144] D.A. Hughes, Microstructural evolution in a non-cell forming metal: AlMg, *Acta Metall. Mater.* 41 (1993) 1421–1430.
- [145] G.I. Taylor, Plastic strain in metals, *J. Inst. Met.* 62 (1938) 307–325.
- [146] B.J. Duggan, M. Hatherly, W.B. Hutchinson, P.T. Wakefield, Deformation structures and textures in cold-rolled 70:30 brass, *Met. Sci.* 12 (1978) 343–351.
- [147] Y. Lü, B. Hutchinson, D.A. Molodov, G. Gottstein, Effect of deformation and annealing on the formation and reversion of  $\epsilon$ -martensite in an Fe-Mn-C alloy, *Acta Mater.* 58 (2010) 3079–3090.
- [148] B. Ravi Kumar, B. Mahato, N.R. Bandyopadhyay, D.K. Bhattacharya, Comparison of rolling texture in low and medium stacking fault energy austenitic stainless steels, *Mater. Sci. Eng. A.* 394 (2005) 296–301.
- [149] H. Paul, J. Driver, C. Maurice, Z. Jasiński, Shear band microtexture formation in twinned face centred cubic single crystals, *Mater. Sci. Eng. A.* 359 (2003) 178–191.
- [150] J.R. Luo, A. Godfrey, W. Liu, Q. Liu, Twinning behavior of a strongly basal textured AZ31 Mg alloy during warm rolling, *Acta Mater.* 60 (2012) 1986–1998.
- [151] S. Sinha, J.A. Szpunar, N.A.P. Kiran Kumar, N.P. Gurao, Tensile deformation of 316L austenitic stainless steel using in-situ electron backscatter diffraction and crystal plasticity simulations, *Mater. Sci. Eng. A.* 637 (2015) 48–55.
- [152] J.W. Christian, S. Mahajan, deformation twinning, *Prog. Mater. Sci.* 39 (1995) 1–157.
- [153] S.S. Cai, X.W. Li, N.R. Tao, Orientation dependence of deformation twinning in Cu single crystals, *J. Mater. Sci. Technol.* 34 (2018) 1364–1370.
- [154] T.S. Byun, On the stress dependence of partial dislocation separation and deformation microstructure in austenitic stainless steels, *Acta Mater.* 51 (2003) 3063–3071.

- [155] J.A. Venables, Deformation twinning in face-centred cubic metals, *Philos. Mag.* 6 (1961) 379–396.
- [156] B.E. Carroll, T.A. Palmer, A.M. Beese, Anisotropic tensile behavior of Ti-6Al-4V components fabricated with directed energy deposition additive manufacturing, *Acta Mater.* 87 (2015) 309–320.
- [157] T.C. Dzogbewu, Additive manufacturing of TiAl-based alloys, *Manuf. Rev.* 7 (2020) 35.
- [158] K.N. Amato, S.M. Gaytan, L.E. Murr, E. Martinez, P.W. Shindo, J. Hernandez, S. Collins, F. Medina, Microstructures and mechanical behavior of Inconel 718 fabricated by selective laser melting, *Acta Mater.* 60 (2012) 2229–2239.
- [159] B. Cheng, S. Shrestha, K. Chou, Stress and deformation evaluations of scanning strategy effect in selective laser melting, *Addit. Manuf.* 12 (2016) 240–251.
- [160] Z. Sun, X. Tan, S.B. Tor, W.Y. Yeong, Selective laser melting of stainless steel 316L with low porosity and high build rates, *Mater. Des.* 104 (2016) 197–204.
- [161] G. Miranda, S. Faria, F. Bartolomeu, E. Pinto, S. Madeira, A. Mateus, P. Carreira, N. Alves, F.S. Silva, O. Carvalho, Predictive models for physical and mechanical properties of 316L stainless steel produced by selective laser melting, *Mater. Sci. Eng. A.* 657 (2016) 43–56.
- [162] Z. Sun, X. Tan, S.B. Tor, C.K. Chua, Simultaneously enhanced strength and ductility for 3D-printed stainless steel 316L by selective laser melting, *NPG Asia Mater.* 10 (2018) 127–136.
- [163] C. Zhang, D. Juul Jensen, T. Yu, Microstructure and Texture Evolution During Cold Rolling of 316L Stainless Steel, *Metall. Mater. Trans. A.* (2021) 1–12.
- [164] R. Hielscher, C.B. Silbermann, E. Schmidla, J. Ihlemann, Denoising of crystal orientation maps, *J. Appl. Crystallogr.* 52 (2019) 984–996.
- [165] D. Kuhlmann-Wilsdorf, Theory of plastic deformation: properties of low energy dislocation structures, *Mater. Sci. Eng. A.* 113 (1989) 1–41.
- [166] N. Hansen, Hall–Petch relation and boundary strengthening, *Scr. Mater.* 51 (2004) 801–806.
- [167] Y.T. Zhu, X.Z. Liao, X.L. Wu, J. Narayan, Grain size effect on deformation

- twinning and detwinning, *J. Mater. Sci.* 48 (2013) 4467–4475.
- [168] F.R.N. Nabarro, Dislocations in a simple cubic lattice, *Proc. Phys. Soc.* 59 (1947) 256–272.
- [169] H.F. Poulsen, S.F. Nielsen, E.M. Lauridsen, S. Schmidt, R.M. Suter, U. Lienert, L. Margulies, T. Lorentzen, D. Juul Jensen, Three-dimensional maps of grain boundaries and the stress state of individual grains in polycrystals and powders, *J. Appl. Crystallogr.* 34 (2001) 751–756.
- [170] L.S. Aota, P. Bajaj, K.D. Zilnyk, E.A. Jägle, D. Ponge, H.R.Z. Sandim, D. Raabe, Recrystallization kinetics, mechanisms, and topology in alloys processed by laser powder-bed fusion: AISI 316L stainless steel as example, *Materialia*. 20 (2021) 101236.
- [171] T. Kurzynowski, K. Gruber, W. Stopyra, B. Kuźnicka, E. Chlebus, Correlation between process parameters, microstructure and properties of 316 L stainless steel processed by selective laser melting, *Mater. Sci. Eng. A.* 718 (2018) 64–73.
- [172] N. Chen, G. Ma, W. Zhu, A. Godfrey, Z. Shen, G. Wu, Materials Science & Engineering A Enhancement of an additive-manufactured austenitic stainless steel by post-, *Mater. Sci. Eng. A.* 759 (2019) 65–69.
- [173] C.N. Kelly, N.T. Evans, C.W. Irvin, S.C. Chapman, K. Gall, D.L. Safranski, The effect of surface topography and porosity on the tensile fatigue of 3D printed Ti-6Al-4V fabricated by selective laser melting, *Mater. Sci. Eng. C.* 98 (2019) 726–736.
- [174] C.S. Smith, Zener pinning, *Trans. Met. Soc. AIME.* 175 (1948) 15–51.
- [175] Y. Liu, B.R. Patterson, Grain growth inhibition by porosity, *Acta Metall. Mater.* 41 (1993) 2651–2656.
- [176] M. Hillert, Inhibition of grain growth by second-phase particles, *Acta Metall.* 36 (1988) 3177–3181.
- [177] A. Harun, E.A. Holm, M.P. Clode, M.A. Miodownik, On computer simulation methods to model Zener pinning, *Acta Mater.* 54 (2006) 3261–3273.
- [178] G.T. Higgins, Grain-Boundary Migration and Grain Growth, *Met. Sci.* 8 (1974)

143–150.

- [179] M. Miodownik, E.A. Holm, G.N. Hassold, Highly parallel computer simulations of particle pinning: zener vindicated, *Scr. Mater.* 42 (2000) 1173–1177.
- [180] A. Agnoli, N. Bozzolo, R. Logé, J.M. Franchet, J. Laigo, M. Bernacki, Development of a level set methodology to simulate grain growth in the presence of real secondary phase particles and stored energy – Application to a nickel-base superalloy, *Comput. Mater. Sci.* 89 (2014) 233–241.
- [181] D. Raabe, L. Hantcherli, 2D cellular automaton simulation of the recrystallization texture of an IF sheet steel under consideration of Zener pinning, *Comput. Mater. Sci.* 34 (2005) 299–313.
- [182] S.P. Gentry, K. Thornton, Sensitivity analysis of a phase field model for static recrystallization of deformed microstructures, *Model. Simul. Mater. Sci. Eng.* 28 (2020) 065002.
- [183] G. Abrivard, E.P. Busso, S. Forest, B. Appolaire, Phase field modelling of grain boundary motion driven by curvature and stored energy gradients. Part I: Theory and numerical implementation, *Philos. Mag.* 92 (2012) 3618–3642.
- [184] V. Yadav, N. Moelans, Y. Zhang, D. Juul Jensen, Effects of dislocation boundary spacings and stored energy on boundary migration during recrystallization: A phase-field analysis, *Acta Mater.* 221 (2021) 117377.
- [185] R.E. Reed-Hill, R. Abbaschian, R. Abbaschian, *Physical metallurgy principles*, Van Nostrand New York, 1973.

# Appendix A

---

Table S1 Rolling steps for conventionally manufactured 316L (C-0).

N	Entrance thickness $h_0$ (mm)	Exit thickness $h_1$ (mm)	Total thickness Reduction after pass N	Thickness reduction for single pass N	Contact length L (mm)	Mean thickness h (mm)	L/h
1	5.17	4.653	10.0%	10.0%	9.37	4.911	1.91
2	4.653	4.394	15.0%	5.6%	6.63	4.523	1.47
3	4.394	4.136	20.0%	5.9%	6.63	4.265	1.55
4	4.136	3.619	30.0%	12.5%	9.37	3.877	2.42
5	3.619	3.102	40.0%	14.3%	9.37	3.360	2.79
6	3.102	2.585	50.0%	16.7%	9.37	2.843	3.30
7	2.585	2.326	55.0%	10.0%	6.63	2.455	2.70
8	2.326	2.068	60.0%	11.1%	6.63	2.197	3.02
9	2.068	1.809	65.0%	12.5%	6.63	1.938	3.42
10	1.809	1.654	68.0%	8.6%	5.13	1.731	2.96
11	1.654	1.551	70.0%	6.3%	4.19	1.602	2.62
12	1.551	1.447	72.0%	6.7%	4.19	1.499	2.80
13	1.447	1.344	74.0%	7.1%	4.19	1.395	3.00
14	1.344	1.240	76.0%	7.7%	4.19	1.292	3.24
15	1.240	1.163	77.5%	6.3%	3.63	1.202	3.02
16	1.163	1.085	79.0%	6.7%	3.63	1.124	3.23
17	1.085	1.034	80.0%	4.8%	2.96	1.059	2.80



## Appendix B

---

Supplementary materials for: Microstructure and texture evolution during cold rolling of 316L stainless steel (manuscript I)

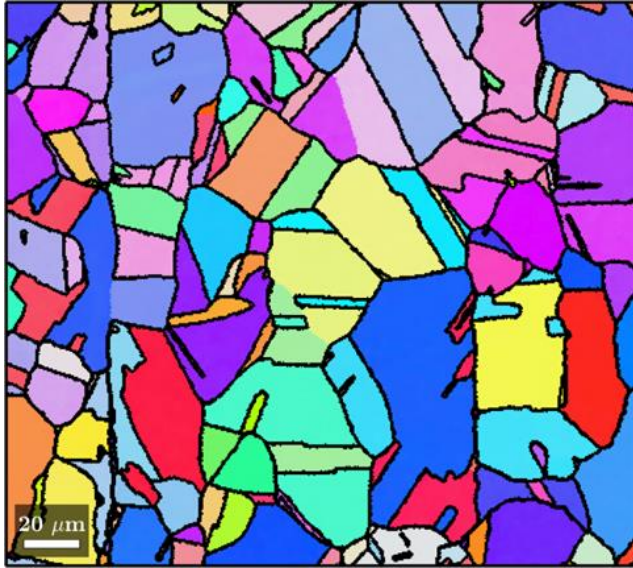


Figure S-1. The EBSD orientation map of as annealed sample.

# Appendix C

---

## Supplementary materials for “The effect of voids on boundary migration in additive manufactured samples—a phase field study” (manuscript III)

### S.1 Isothermal annealing

The 3D printed 316L stainless steel sample was cold rolled to 30% in thickness reduction followed by annealing at 850°C for 7 min (denoted A1). Three further annealing steps (denoted A2, A3, A4) were done at the same temperature with the holding time of 1 min for each step. To overcome effects of thermal grooving, one further annealing step (A5) was done at 870°C for 1 min. All the annealing was done in a vacuum furnace. The sample (A1) was prepared by grinding using SiC papers followed by mechanical polishing using a colloidal silica suspension (0.04 μm) for the final polishing step. There is no additional polishing between the subsequent annealing steps (A2-A5).

### S2 Phase field model

In the present study, the void, presented by an order parameter  $\Phi$ , is included to the phase field model [81]. Based on the Ginsburg-Landau equation:

$$\frac{\partial \eta}{\partial t} = -L \frac{\partial F}{\partial \eta} \quad \text{S(9)}$$

The numerical equations are thus modified as:

$$\frac{\partial \eta_{rex,i}}{\partial t} = -L \left[ m \left( \eta_{rex,i}^3 - \eta_{rex,i} + 3\eta_{rex,i} \left( \sum_{i \neq j}^p \eta_{rex,j}^2 + \eta_{def}^2 \right) - \kappa \nabla^2 \eta_{rex,i} + 2\epsilon \eta_{rex,i} \Phi^2 - \frac{2\eta_{rex,i} \eta_{def}^2}{\left( \sum_{i=1}^p \eta_{rex,i}^2 + \eta_{def}^2 + \Phi^2 \right)^2} f_{def}(x, y) \right) \right], \quad \text{S(10)}$$

$$\frac{\partial \eta_{def}}{\partial t} = -L \left[ m \left( \eta_{def}^3 - \eta_{def} + 3\eta_{def} \sum_{i=1}^p \eta_{rex,i}^2 \right) - \kappa \nabla^2 \eta_{def} + 2\epsilon \eta_{def} \Phi^2 + \frac{2\eta_{def} \left( \sum_{i=1}^p \eta_{rex,i}^2 + \Phi^2 \right)}{\left( \sum_{i=1}^p \eta_{rex,i}^2 + \eta_{def}^2 + \Phi^2 \right)^2} f_{def}(x, y) \right] \quad \text{S(11)}$$

where  $\eta$  is the order parameter for recrystallized grains or deformed microstructure, i.e.  $\eta_{rex}$  and  $\eta_{def}$ . The model parameter  $L$  is a kinetic coefficient related to the grain boundary mobility  $\mu_{gb}$  and diffuse interface width  $\iota_{gb}$  [114]:  $L = 4/3 \cdot \mu_{gb} \cdot \iota_{gb}$ . The parameter  $p$  refers to the number of recrystallizing grains.

A standard finite-difference discretization with a central five-point scheme for the spatial Laplacian and explicit time stepping was applied in Eqs. S(6) and S(7). von Neumann boundary condition was applied in the X and Y directions. In the present study, the mobility of the grain boundary  $\mu_{gb} = 6 \times 10^{-14} \text{ m}^4/(\text{J}\cdot\text{s})$ ; the grain boundary energy  $\sigma_{gb} = 0.32 \text{ J/m}^2$ ; the time step  $\Delta t = 0.0023\text{s}$ ; grid spacing  $\Delta x = 14.1 \text{ nm}$ ; order parameters:  $m=22.7 \text{ MJ/m}^3$ ,  $L = 9.46 \times 10^{-7} \text{ m}^3/(\text{J}\cdot\text{s})$ , and  $\kappa=2.03 \times 10^{-8} \text{ J/m}$ ;  $\epsilon=22.7 \text{ MJ/m}^3$ . The energy and mobility of the grain boundary and the stored energy are the typical values for Al [184].

### S3 Sine function defined microstructure (SM)

The sine function defined microstructure (SM) was defined by the following equation:

$$f_{def} = \max \left\{ A \left[ 1 + \sin \left( \frac{\pi}{64} \left( y - \frac{x}{\tan\left(\frac{\pi}{12} + \frac{\pi}{2}\right)} \right) \right) \right], A \left[ 1 + \sin \left( \frac{\pi}{64} \left( y - \frac{x}{\tan\left(-\frac{\pi}{12} + \frac{\pi}{2}\right)} \right) \right) \right] \right\} \quad \text{S(12)}$$

where  $A = 0.367 \text{ MJ/m}^3$ . The maximum and minimum stored energy were  $0.7 \text{ MJ/m}^2$  and  $0.7 \text{ J/m}^2$  [184], respectively.

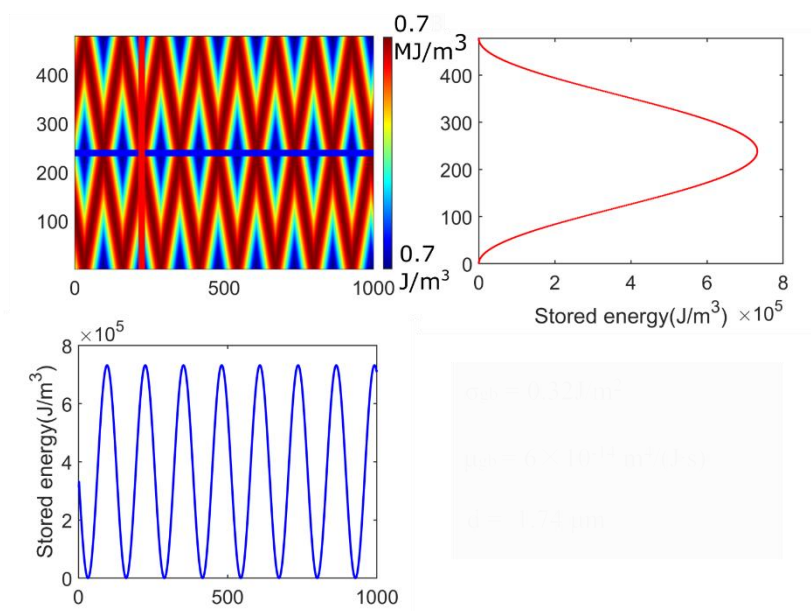


Fig. S1. The sine function defined microstructure (SM). The right plot: energy variation along the vertical red line in the top-left plot; the bottom plot: along the horizontal blue line.

#### S4 Boundary motion in uniform deformed microstructure (HM) with and without a void

Before encountering the void, the boundary moves at a constant velocity of  $0.0304 \mu\text{m/s}$ , while the analytical solution of  $v = MP$  is  $0.0308 \mu\text{m/s}$ , i.e. a deviation of 1.3%. This is reasonable because there is often a deviation of 1%-5% due to the discretization in the numerical simulation. Similar to the pinning effect of particles, when the boundary encounters a void, the shape and velocity of the boundary are strongly affected.

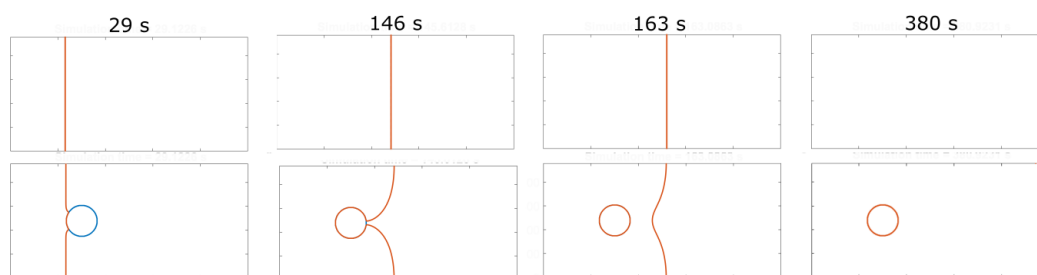
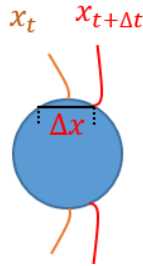


Fig.S2 Interaction between recrystallizing boundary with the void in a system containing uniform stored energy.

## S5 Calculation of boundary velocity

The boundary velocity is calculated over every 500 time steps, i.e. 1.15 s.  $V = \frac{\Delta x}{\Delta t}$ ,  $\Delta x$  is the boundary migration distance during the time interval  $\Delta t$ . It is assumed that the boundary migrates in the x direction and the positions of boundary segments are interpolated over grid points. Therefore, the migration distance of segment  $i$ :  $\Delta x^i = x_{t+\Delta t}^i - x_t^i$ . It is worth noting that there will be errors in the determination of  $\Delta x$  after the boundary pass through the half of the void: As shown in the figure below, the boundary migration distance  $\Delta x^i$  is obviously not fully correct. This artifact will cause a discontinuity in the boundary velocity calculation, which is tackled by removing these huge outliers in the boundary velocity and smoothing the velocity curve using linear interpolation.





Danmarks Tekniske Universitet

Produktionstorvet  
Bygning 425  
2800 Kgs. Lyngby  
Tel. 45 25 19 60  
Fax 45 25 19 61

[www.mek.dtu.dk](http://www.mek.dtu.dk)